UNIVERSITY OF CALIFORNIA, MERCED

# APPLICATIONS OF LONG RANGE DEPENDENCE CHARACTERIZATION IN THERMAL IMAGING & HEART RATE VARIABILITY

by

Marwin Ko

A thesis submitted in partial satisfaction of the
requirements for the degree of
Master of Science

in

Mechanical Engineering

Committee in charge:
Professor YangQuan Chen, Chair
Professor Kara McCloskey
Professor Jian-Qiao Sun

The thesis of Marwin Ko is approved:

YangQuan Chen, Chair Date

Kara McCloskey Date

Jian-Qiao Sun Date

University of California, Merced

To my family: Ronald Ko, Susie Chang, and Gordon Ko.

# ACKNOWLEDGEMENTS

First, I would like to thank Professor YangQuan Chen for providing me with an unparalleled graduate experience. My two years in graduate school were completely funded with the help of Professor Chen and the University. Professor Chen has also endowed me with the knowledge and fundamental ideology of fractional calculus (FC) of which my thesis is centered upon. Lastly, Professor Chen provided me with the extraordinary opportunity of meeting Richard L. Magin, Igor Podlubny, and Bruce J. West; juggernauts of the FC world.

Second, I want to thank Professor Kara McCloskey and Professor JianQian Sun for participating in my graduate committee and helping me edit my thesis.

Third, I would like to thank my colleagues Zhou Li, Tiebiao Zhao, Brendan Smith, and Brandon Stark for their support in technical and research related matters. In particular, I would like to thank Brandon Stark for his advice and guidance in writing my first conference paper. I want also acknowledge and thank Jeremy Ho, Trevor Murdock, and Andrena Rodriquez for helping me edit my first conference paper.

Fourth, I wish to acknowledge my undergraduate interns Cody Crossley, Kevin Cunha, Dannilo Ibarra and Monica Barbadillo for their assistance in research and coding. Specifically I want to give a special thanks to Monica for her unparalleled work ethic and special aptitude for coding biometric algorithms in this thesis.

Fifth, I want to express my gratefullness to my immediate family for providing my housing, financial support, and unprecedented home cooked chinese food. Sixth, I would to thank Ivan Leung for his assistance in building my computer which was responsible a monstrous amount of calculations, simulations, and data processing.

In this portion, I thank God for providing me with following people that have made monumental changes in my life. I want to thank Mark Stone for imparting me with the attitude that I can do anything I put my mind to. I also thank Sushant Soni for his help and life advice during our academic expedition (undergraduate); without him, I would not be in the field of engineering. Unfortunately in the midst of my undergraduate journey there were several times when I believed that I was not smart enough to continue. I want to wholeheartedly thank Elton Leung for encouraging me to continue along the engineering path; see Fig 1 for a motivational quote he provided to me back in 2010. I also wish to thank Paul Bargouth for his friendship and bestowing me with the mentality of working diligently or not at all; “go hard or go home” as he would say. However, solely working diligently in graduate school proved to be insufficient. I want to thank my closest friend during my Master’s program, Alan Richards, for constantly challenging me to rethink of new ways to work more efficiently; as his saying goes “work smarter, not harder”. Finally, I want to thank my girlfriend, Tina Kuang, for keeping me grounded for a majority of my college career.

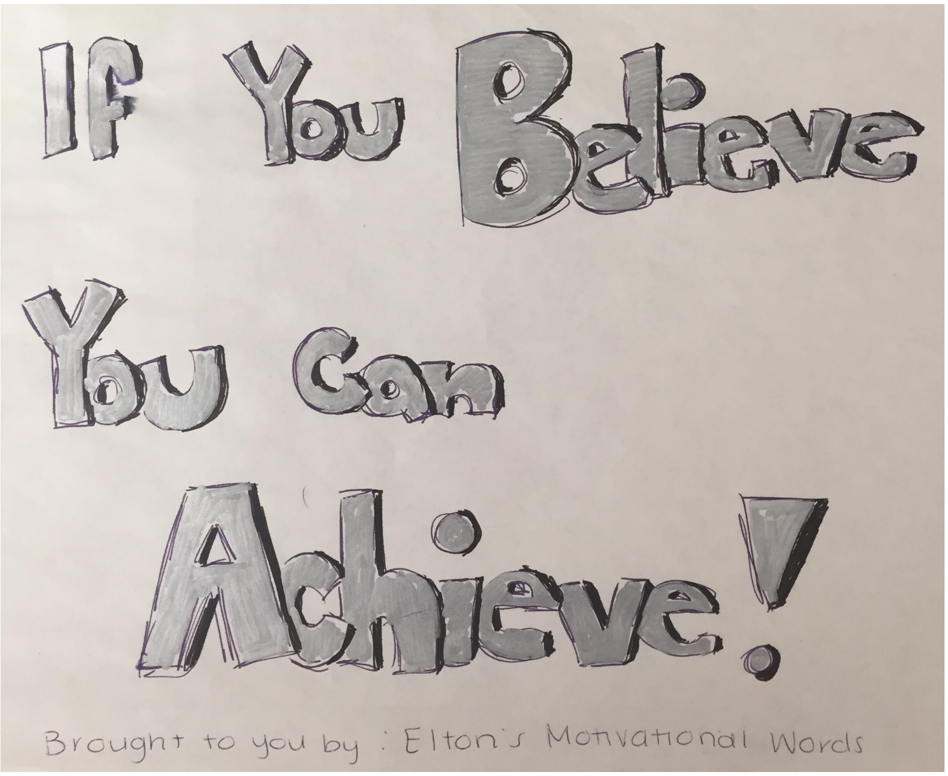

**Figure 1:** Motivational words.

I must also express my sincere appreciation to my friends during my tenure as a graduate student. Thank you for all the good times! See list of friends below.

- Paul Bargouth
- Michael Garcia
- Megan Hamlin
- Jeremy Ho
- Brandon Needens
- Alan Richards
- Andrena Rodriguez
- Sajjan Sodhi
- Steven Stone
- Blake Stockman
- Jeffrey Wong
- Andrew Young

# CURRICULUM VITAE

## Education

B.S. in Bioengineering, University of California, Merced, 2013.
M.S. in Mechanical Engineering, University of California, Merced, 2015.

## Scholarships

Community Engaged Scholarship Award, University of California, Merced, 2014.
Dean's Travel Scholarship, University of California, Merced, 2015.

## Publications

M. Ko, M. Barbadillo, Y.Q. Chen, 2015, "Heart Rate Variability Stress Detection using Diffusion Entropy Analysis ". *In Proceedings of 2015 International Symposium on Fractional Signals and Systems. October 2015, Cluj-Napoca, Romania.*

M. Ko, M. Barbadillo, B. Stark, Y.Q. Chen, 2015, "An Evaluation of three approaches using Hurst Estimation to Differentiate between Normal & Abnormal HRV ". *In Proceedings of 2015 ASME International Design Engineering Technical Conferences & Computers and Information in Engineering Conference. August 2015. Boston, MA, USA. DETC2015-46966* .

T. Lv, Y.Q. Chen, M. Ko, B. Stark, 2014, "An Online Heart Rate Variability Analysis Method Based on Sliding Window Hurst Series ".*In Proceedings of 2014 International Conference on Fractional Differentiation and its Application. June 2014, Catania, Italy.*

# TABLE OF CONTENTS

**Chapter**

**Appendix**

# LIST OF FIGURES

# LIST OF TABLES

# ACRONYMS

| | |
|---|---|
| ACF | Autocorrelation function |
| ANS | Autonomic nervous system |
| ATP | Adenosine triphosphate |
| AV | Aortic valve |
| AVN | Atrioventricular node |
| AVV | Atrioventricular valves |
| CPU | Central processing unit |
| CWE | Cumulative window estimation |
| ECG | Electrocardiogram |
| fBm | Fractional Brownian motion |
| FC | Fractional calculus |
| FPA | Focal plane array |
| HRV | Heart rate variability |
| HSE | Hurst sectional estimation |
| LRD | Long range dependence |
| MV | Mitral valve |
| NUC | Nonuniformity correction |
| OP | Optimizing parameter |
| PDF | Probability density function |
| PV | Pulmonary valve |
| RMSE | Root mean squared error |
| SAN | Sinoatrial node |
| SLV | Semilunar valves |
| SWE | Sliding window estimation |
| SWV | Sliding window variable |
| TIR | Thermal infrared |
| TSE | Total time series estimation |
| TV | Tricuspid valve |

# ABSTRACT

The world we live in is nonlinear. Fortunately, there are several mathematical methods to linearize a system. However, a multitude of nonlinear systems exists that cannot be fully linearized; such as economical, ecological, and biological systems. Linear or linearized systems are desired due to their predictable characteristics. On the other hand, nonlinear systems are unpredictable and considered stochastic. Is it possible to predict the unpredictable? Yes it is possible, to a degree. However, traditional or integer based mathematics do not suffice. Utilizing fractional calculus (FC) as a mathematical tool, one is able to describe nonlinearity in a system; with the assumption that there is memory or fractal properties embedded in the system. The Hurst exponent ($H$), also known as the Hurst parameter, is used to determine the intensity of memory in a system. The range of the Hurst is $H \in (0, 1)$. Memory, also referred to as long range dependence (LRD), is the inverse power law decay of statistical correlation over lag time; memory is present when $0.5 < H < 1$. Herein, the Hurst exponent is used to identify LRD in thermal pixels; classify between normal heart rate variability (HRV) and arrhythmic HRV; and detect mental stress using HRV from human subjects.

# Chapter 1

# INTRODUCTION

## 1.1 Motivation

The notion of integers, meaning whole, is ingrained in our everyday lives. Examples of integer order can be as simple as currency or as complex as a computer. One could view currency as being fractional since a $1 bill can be broken into change, however, a penny cannot be divide into smaller increments. As I type my thesis on my computer, each key pressed sends a voltage to the central processing unit (CPU) that is read in binary, which is integer order, to determine the output of each key. One could argue that calculators can compute fractional numbers by computing the square root of an irrational or prime number. While that may be true to a degree, calculators use a series of linear approximations, which is based on integer, to determine those fractional numbers. This bring us to the fundamental topic of mathematics, specifically integer order calculus; invented independently by Isaac Newton and Gottfried Wilhelm Leibniz. Since the 17th century, integer order calculus has provided a framework to analyze the real world using approximations. However, approximations may lead to information loss within a signal, system, etc.

### 1.1.1 Fractional Calculus

A french mathematician by the name of Guillaume de l'Hôpital questioned what if the order of the derivative was non-integer. In September 30th, 1695 l'Hôpital wrote a letter to Leibniz asking him about the $n^{th}$-derivative of a linear function $f(x) = x$, where the derivative can be written as $\frac{D^n x}{Dx^n}$ [1]. Specifically, l'Hôpital asked what would the result be if $n = \frac{1}{2}$? Leibniz replied [1], "An apparent paradox, from which one day useful consequences will be drawn." As a result of that conversation, fractional calculus (FC) was born.

The world is stochastic, nonlinear, and complex which is hard to model [2]. Conventional methods to model randomness, such as Brownian motion, do not always suffice due to hidden fractal properties [3]. Typically masqueraded by nonlinearity, fractals are often coupled with useful statistical information. In the mid 1900s, Paul Lev́y utilized the Riemann-Liouville fractional integral [4],

$$ {}_aD_t^{-\alpha}[f(t)] = \frac{1}{\Gamma(\alpha)} \int_0^t \frac{f(\tau)}{(t-\tau)^{1-\alpha}} d\tau, \tag{1.1} $$

to informally define fractional Brownian motion (fBm). After some revisions, a formalized fBm is defined as [2],

$$B_H(t) = B_H(0) + \frac{1}{\Gamma(\alpha)}\left\{ \int_{-\infty}^{0} \frac{d(s)}{(t-s)^{1-\alpha} - (-s)^{1-\alpha}} + \int_{0}^{t} \frac{d(s)}{(t-s)^{1-\alpha}} \right\}, \tag{1.2}$$

where

$$\alpha = H + \frac{1}{2}. \tag{1.3}$$

In Eq. 1.2, increments may or may not be independent of each other. The scaling exponent ($H$), captures the statistical complexity of the fractal process or system. In Chapter 3 the scaling exponent, also referred to as the Hurst exponent or Hurst parameter, is revisited and explained in a detail.

## 1.2 Contributions

This section highlights three major contributions made: Hurst map, sliding window optimization, and classification index. In all three contributions, the Hurst estimator plays a central role. In the Hurst map, the Hurst exponent ($H$) is estimated using an array of thermal infrared (TIR) data from each individual pixel for a whole TIR image to detect long range dependence (LRD) and display its morphology. Although the sliding window technique itself is not necessarily novel, the optimization of the sliding window using a surface plot to quantitatively determine an optimal window and slide combination is presented here. Lastly, utilizing the Hurst exponent as a classification index to determine whether a person has a cardiac arrhythmia or not.

### 1.2.1 Hurst Map

There are 307,200 pixels in an image from a 640 × 480 pixel resolution. Due to computational limits, only every 20 pixels were analyzed. A total of 825 pixels were selected to be analyzed. The TIR data with respect to time for each selected pixel is then analyzed using a Hurst estimator [5], in this case, the diffusion entropy. The estimated Hurst exponent for each pixel is then placed into the same location as the pixel element used to estimate that respective Hurst exponent. A generalized illustration of the Hurst map with respect to pixels location is shown in Fig. 1.1.

Finally, a surface plot, or Hurst map, is created from these Hurst exponents. The Hurst map is a novel technique in displaying LRD or statistical persistency for individual pixels as well as the location of those persistencies. If there are statistical persistency bias present, then there is potential in exploiting those statistical characteristics for cleaning up noise in TIR images. This technique, Hurst mapping, is utilized in Chapter 4 to determine if LRD is present and their location relative to the pixel matrix.

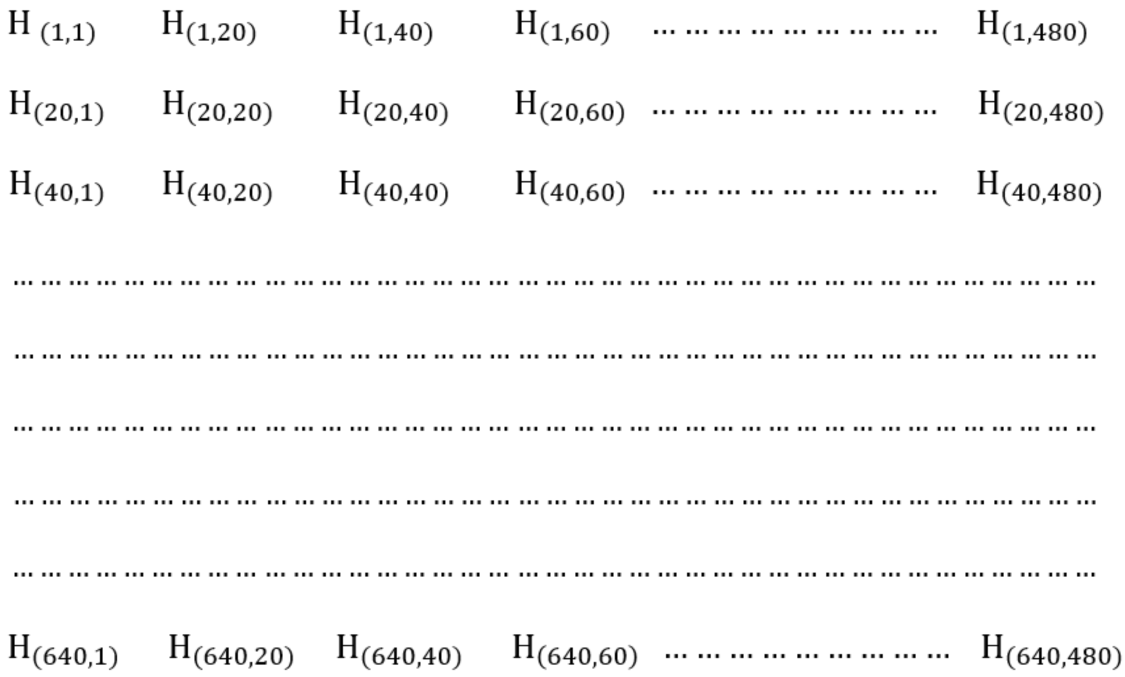

$$\begin{array}{llllll}
H_{(1,1)} & H_{(1,20)} & H_{(1,40)} & H_{(1,60)} & \dots\dots\dots\dots\dots\dots\dots\dots\dots & H_{(1,480)} \\
H_{(20,1)} & H_{(20,20)} & H_{(20,40)} & H_{(20,60)} & \dots\dots\dots\dots\dots\dots\dots\dots\dots & H_{(20,480)} \\
H_{(40,1)} & H_{(40,20)} & H_{(40,40)} & H_{(40,60)} & \dots\dots\dots\dots\dots\dots\dots\dots\dots & H_{(40,480)} \\
\dots & \dots & \dots & \dots & \dots & \dots \\
\dots & \dots & \dots & \dots & \dots & \dots \\
\dots & \dots & \dots & \dots & \dots & \dots \\
\dots & \dots & \dots & \dots & \dots & \dots \\
\dots & \dots & \dots & \dots & \dots & \dots \\
H_{(640,1)} & H_{(640,20)} & H_{(640,40)} & H_{(640,60)} & \dots\dots\dots\dots\dots\dots\dots\dots\dots & H_{(640,480)}
\end{array}$$

**Figure 1.1:** Generalized illustration of the Hurst map.

### 1.2.2 Sliding Window Optimization

A novel technique to optimize a sliding window is presented. The concept of a sliding window was inspired by previous research [4] and will be explained first. Subsequently, the algorithmic framework of the sliding window is given in detail. Lastly, a generalized procedure of optimizing a sliding window is described in detail. This sliding window optimization procedure was utilized in Chapters 5 and 6 for heart rate variability (HRV) analysis, but can be applied to any type of data for truncation purposes.

#### 1.2.2.1 Sliding Window Concept

The sliding window consists of one tangible component called the window and moves dynamically by increments of the slide length. The window component is a truncated segment of data from which the Hurst exponent is estimated from. The slide is the movement of the window, with respect to time. Both window length ($w_t$) and slide length ($s_t$) are units of time in minutes.

In the initial step, the window is constructed with the boundary starting at the first data point and extending to the length of $w_t$ of the data. Once the window is constructed, the data inside the window is truncated. The truncated data is used to estimate the first Hurst exponent. See Fig. 1.2, part A, for illustration of this initial step.

In the following step, an iterative truncation, the defined window then shifts by the length indicated by $s_t$ and the new truncated segment of HRV data of length $w_t$ is used to compute the next Hurst exponent; see Fig. 1.2, part B, for illustration of this first slide.

This iterative truncation is then repeated until the constructed window attempts to truncate a portion of the HRV data in which $w_t$ is greater in length. The remaining HRV data less than the window length will be neglected. A generalized illustration of the sliding window is shown in Fig. 1.2.

In this thesis the sliding window is only utilized relative to time. However, that does not mean the sliding window is limited to only time. It is paramount to understand that this sliding window is extremely modular. The sliding window can be modified to work relative to data points instead of time. Herein, time is the unit of choice for potential applicational purposes in the medical field. Note that there is an extreme difference between 60 data points as opposed to an arbituary amount of data points in a 60 second time span.

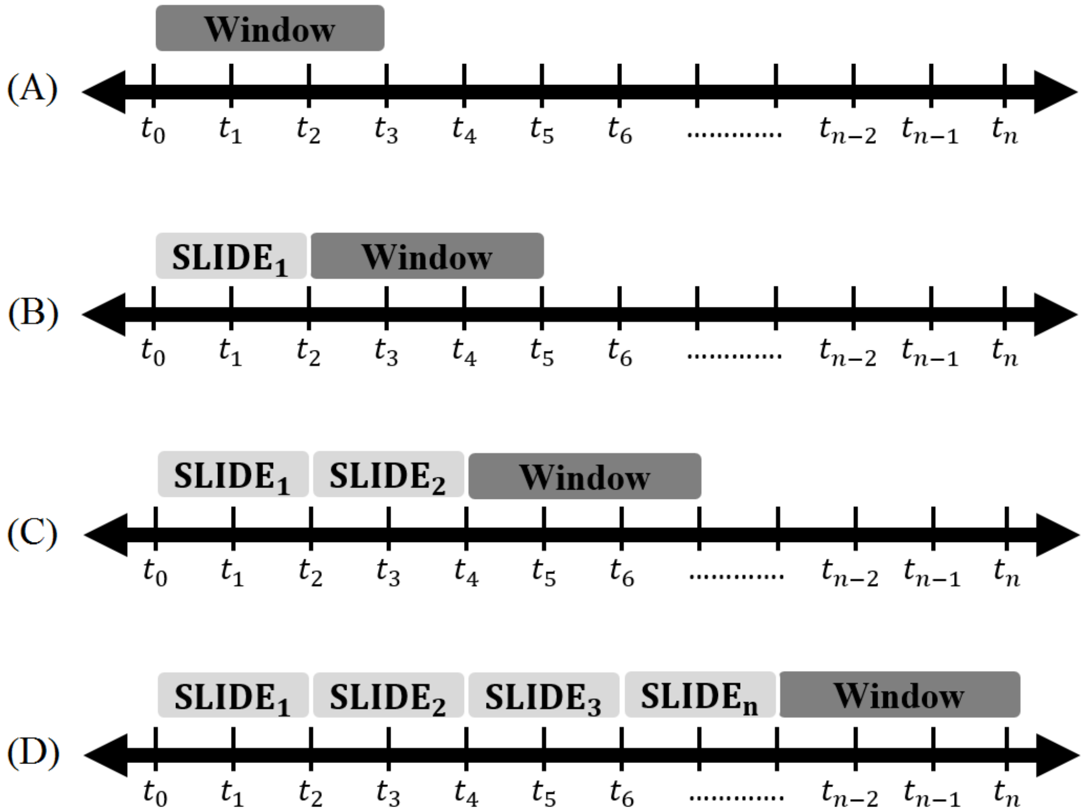

**Figure 1.2:** Generalized illustration of the sliding window.

#### 1.2.2.2 Sliding Window Algorithmic Framework

Let $i$ represent the number of iterations such that $\{i_I : I \in \mathbb{N}\}$. The number of iterations $I$ is defined as,

$$I = \left\lceil \frac{N - w_t}{s_t} \right\rceil, \tag{1.4}$$

where $N$ is total length of sample in minutes. Now consider the following initial conditions, when $i = 1$ for the window:

$$w_{start}(1) = 0, \tag{1.5}$$

$$w_{end}(1) = w_t. \tag{1.6}$$

After the initial condition, when $i > 1$, consider the following equations:

$$w_{start}(i) = w_{start}(i-1) + s_t, \tag{1.7}$$

$$w_{end}(i) = w_{end}(i-1) + s_t. \tag{1.8}$$

As previously mentioned, window length must always be greater than the slide length; $s_t \leq w_t$. If this condition is not met, it will result in neglected data per iteration when calculating the Hurst exponent. Explicitly, the difference between $s_t$ and $w_t$ is the amount of HRV data neglected per iteration. The resulting Hurst sliding window data series is defined as,

$$H(i) = H[x(t)]_{w_{start}}^{w_{end}}, \tag{1.9}$$

where $H[\,]$ is a function of the Hurst estimator. A variety of Hurst estimators are described in depth in Chapter 3.

#### 1.2.2.3 Sliding Window Optimization Protocol

The sliding window is a practical algorithmic framework in which it can detect changes in a signal or system via data truncation or partition. At every slide, the window outputs a sliding window variable ($SWV$) which can be implemented in real time for real world applications such a periodic health monitoring.

However, the parameters of the sliding window, $w_t$ and $s_t$, would vary from application to application. Herein, a novel technique to optimize a sliding window is presented. The sliding window optimization procedure is described in a generalize manner such that it remains modular and can be modified based on a variety of research requirements or parameters. This optimization technique is utilized in Chapter 5 and 6.

A generalized protocol to help optimize the sliding window algorithmic framework is explained as follows:

1. For all $w_t$ of interest and $s_t$ such that $s_t \leq w_t$, calculate the $SWV$ of interest, e.g. Hurst exponent.
    - Each sample in the dataset should contain a cell array.
    - Cell array should be window by slide length dimension.
    - Each cell in the cell array should contain a vector containing $SWVs$ that were calculated based on $w_t$ and $s_t$.
2. Calculate optimizing parameter ($OP$) using $SWV$ vector in each cell. A potential $OP$ can be a statistical variable such as mean, variance, or etc.
    - Each sample in the dataset should now contain a matrix with the same dimensions as the cell array in the first step.
    - Each matrix element should now be an $OP$; e.g. the mean, variance, or RMSE of the $SWV$ vector.
3. Using all samples, average the $OP$ with respect to $w_t$ and $s_t$.
    - There should only be one matrix containing.
    - Each matrix element is an averaged $OP$ with respect to $w_t$ and $s_t$.
4. Graph 3D plot with respect to $w_t$, $s_t$, and averaged $OP$.
    - The $z$-axis should always be the averaged $OP$ in order to clearly view surface morphology.
    - Review surface to determine if an optimal combination of $w_t$ and $s_t$ clearly exists. For example, if the $z$-axis is variance, the optimal combination of $w_t$ and $s_t$ should be the lowest region on the 3D surface plot.
    - One can choose to stop at this step and decide on an optimal combination of $w_t$ and $s_t$.
5. Trace over 3D plot with maximum or minimum value of averaged $OP$ with respect to each $w_t$.
    - Depending on what the averaged $OP$ is, such as mean, variance, or RMSE, determines whether a maximum or minimum value trace is warranted. For example, if the $OP$ is variance, then one would wish to perform a minimum trace to obtain lowest variability combinatory pairs of $w_t$ and $s_t$.

6. Heuristically pick optimal combination of $w_t$ and $s_t$ on dataset.
    - Use the following heuristic guideline:
        (a) Review from starting with smallest $w_t$ available in trace line.
        (b) If $OP$ trace line converges to optimal $OP$ value, then select smallest $w_t$ closest to that optimal $OP$ value.
        (c) Always select smallest $s_t$, not smallest $w_t$; to maximize sliding window output.

### 1.2.3 Classification Index

Previous research [4, 6, 7] have utilized the Hurst exponent as a classification index as well. In Chapter 5, six Hurst estimators were evaluated for accuracy in differentiating between normal sinus rhythm and arrhythmia. All Hurst estimators computed a higher Hurst exponent for normal sinus rhythm samples and lower Hurst exponent for arrhythmia. This is due to the innate presence of LRD in physiological signals. An arrhythmia, or irregular heartbeat, compromises the presence of LRD since an arrhythmia introduces stochastic characteristics to the HRV. Ultimately, the diffusion entropy method proved to be most accurate, see Chapter 5. Thus making the Hurst exponent a relatively viable classification index for cardiac arrhythmia.

## 1.3 Thesis Outline

This thesis is comprised of seven chapters. Herein, Chapter 1, an introduction to the thesis is given. Comprehensive background information regarding HRV and TIR imaging is given in Chapter 2. In Chapter 3, the mathematical concepts are explained and in particular the notion of LRD is highlighted. In Chapter 4, the presence of LRD in TIR imaging is established using the Hurst exponent to analyze individual temporal pixel data. In Chapter 5, LRD characterization is utilized to differentiate between normal HRV and arrhythmic HRV via Hurst exponent. In Chapter 6, the Hurst exponent is used to determine mental stress from drivers. Note that the Hurst exponent is utilized as a classification index for arrhythmia and stress in Chapter 5 and 6, respectively. Finally, Chapter 7 summarizes key research findings and discusses future research.

In addition, there is a tri-sectional appendix located at the end of the thesis. Detail explanations of experimental protocols utilized are given in Appendix A. Appendix B contains all sample data from Chapter 4, 5, and 6. Finally, all in-house code written by my intern (Monica Barbadillo) and myself (Marwin Ko) was compiled into Appendix C.

# Chapter 2

# BACKGROUND

## 2.1 Thermal Infrared Imaging

In the 1800s, a scientist by the name of Sir William Herschel hypothesized that different colors refracted from sunlight may have varying temperatures [8]. To test his hypothesis, Herschel directed sunlight via glass prism to construct a color spectrum where each color was measured in temperature. The empirical results showed that the temperatures of the colors were higher than that of the control. An increasing temperature gradient existed from violet to red. Curiosity struck Herschel and lead to him questioning beyond the red portion of the color spectrum. After empirical review, Herschel discovered that the region beyond the red portion was the hottest; he had discovered an invisible form of light called infrared or radiation [8,9]. Similar to other colors of the spectrum, infrared is also reflected, refracted, and absorbed.

In the 1950s, a company named AGA began development of infrared camera technology. By the 1960s, AGA sold commericalized infrared cameras. Today, infrared cameras are utilized for, but not limited to, military [10], biomedical [11], and industrial applications [12]. Specific applications include night vision, non-invasive body tissue analysis, and detecting hot spots in wild fires.

Consider the human eye, it utilizes visible light energy that is bounced off from objects to visualize the world. The reflected light energy is then focused through the cornea then arrives at the retina. The retina is responsible for receiving light energy, processing it, and then sending the image to the brain. An infrared camera is similar to the human eye in regards to processing the image.

Infrared cameras can be divided into two, passive and active [13]. A detailed explaination of passive infrared cameras will be given since a passive thermal infrared (TIR) camera was utilized in experiments in Chapter 4. A passive TIR camera detects emitted heat energy radiation from objects and does not require light as opposed to a human eye [9]. The emitted radiation is then focused with the lense to the infrared sensor array, also known as a focal plane array (FPA) [9, 14]; the TIR camera counter part of the eye's retina. The FPA coverts the energy into an image. As for active TIR cameras, near IR-radiation is emitted and utilizes the reflection of the self-emitted IR-radiation to process images; this is a more intense TIR imaging technique [13].

## 2.2 Heart Rate Variability

The ultimate biological source of energy is adenosine triphosphate (ATP). Vital biological functions such as metabolism, skeletal muscle movement, cardiac muscle contraction, and deoxyribonucleic acid (DNA) synthesis all rely on the use or consumption of ATP. Without ATP, we would not be able to metabolize food, physically move, circulate blood throughout the body, and conduct cellular division. The body produces over 90% of its ATP using proton gradients at a cellular level [15]. This proton gradient drives an oxidation and reduction reaction. The oxidation reaction requires carbon fuel and oxygen which are obtained from eating and breathing, respectively. While the reduction reaction only requires a proton, hydrogen phosphate group, and adenosine diphosphate (ADP) to make ATP [15].

It is imperative to note that the oxygen molecule is used up and becomes carbon dioxide. As a consequence, the carbon dioxide must be expelled and the oxygen must be replaced. The circulatory system is responsible for supplying oxygen throughout the body. The driving force of the circulatory system is a double pump organ known as the heart [16].

### 2.2.1 Heart Anatomy

The heart consists of four chambers [16]: left and right atrium, left and right ventricle; and four valves: tricuspid valve (TV), pulmonary valve (PV), mitral valve (MV), and aortic valve (AV). Collectively, the TV and MV are known as the atrioventricular valve (AVV). In addition, the pairing of PV and AV are known as the semilunar valves (SLV).

The right atrium and ventricle, connected by the TV, assist in pumping deoxygenated blood through the PV to the lungs where the blood gets reoxygenated. The left atrium and ventricle, connected via MV, pump the newly oxygenated blood through the AV, the largest artery in the body, to the rest of the body via smaller arteries [16]. See Fig. 2.1 for a generalized illustration of the heart anatomy and blood circulation.

### 2.2.2 Heart Physiology

In this section, the heart is broken down into two subsections. The subsection, Cardiac Pump Cycle, discusses the mechanical steps of pumping of blood using the heart. The following subsection, Cardiac Electrical Cycle, discusses the electrical conduction pathway of the heart. Ultimately, the electrical cycle or conduction dictates the cardiac output. Therefore, comprehension of the mechanical and electrical elements of the heart is paramount to understanding how electrocardiogram (ECG) readings are directly related to general heart health and heart rate variability (HRV).

#### 2.2.2.1 Cardiac Pump Cycle

One heartbeat can be broken down into 4 phases: 2 diastole and 2 systole [16]. In this subsection when ventricle or ventricular are mentioned, both left and right ventricle are being discussed. The first phase consists of filling the ventricle with blood. In the second phase, the AVV close and isovolumetric ventricular contraction occurs. Subsequently the SLV open and then ventricular ejection of the blood takes place. Finally, both AVV and SLV are closed and isovolumetric ventricular relaxation transpires [16].

The phases of a cardiac cycle is as follows:

1. Opening of AVV → Ventricular filling
2. Closing of AVV → Isovolumetric ventricular contraction
3. Opening of SLV → Ventricular ejection
4. Closing of SLV → Isovolumetric ventricular relaxation

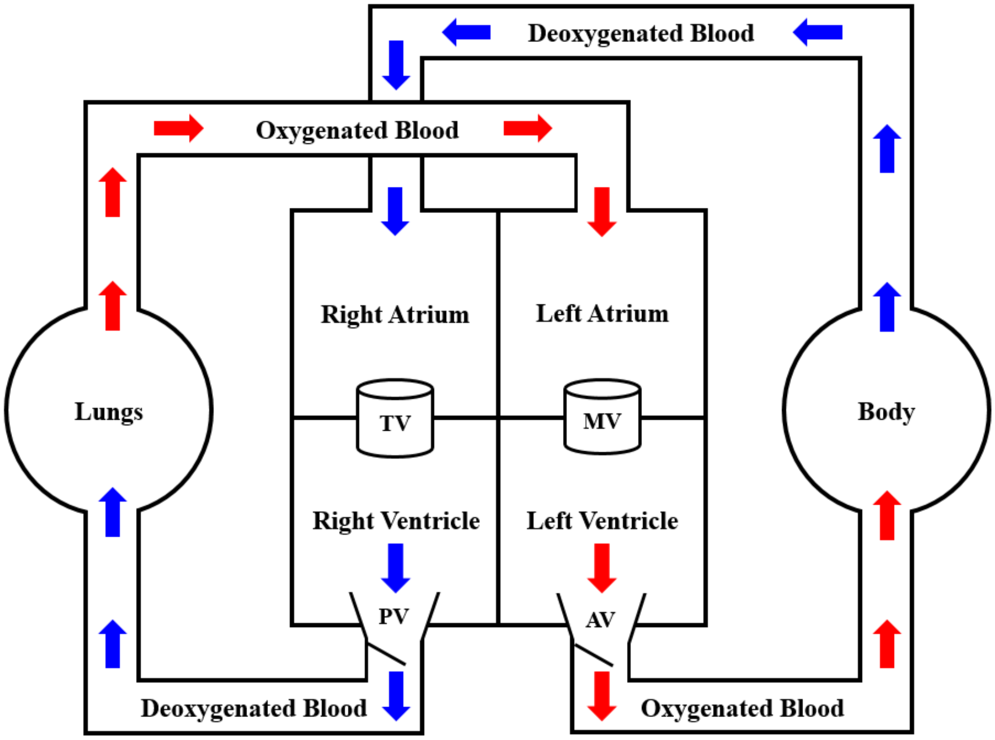

**Figure 2.1:** Engineering illustration of the circulatory system.

#### 2.2.2.2 Cardiac Electrical Cycle

The genesis of any normal heartbeat begins with the electrical signal generated from the sinoatrial node (SAN) also known as the pacemaker. The pacemaker is located in the within the wall of the right atrium. Once an signal is generated from the packemaker, the signal propagates throughout the atrial myocytes in both left and right atriums. At the cross section of all four chambers the signal arrives at the atrioventricular node (AVN). The AVN then relays the electrical signal to the bundle of His which split into the left bundle branch and right bundle branch. This electrical signal continues to propagate through the left bundle branch and right bundle branch down to the apex of the heart. Finally, at the apex, the Purkinje fibers relay the electrical signal to the ventricular myocardium [16].

### 2.2.3 Electrocardiogram

In the early 1900s, a Dutch physiologist by the name of Willem Einthoven recorded the first ECG reading using a string galvanometer. Current medical practices use ECGs as a standard clinical tool to measure electrical activity of a patient's heart [16]. There are several artifacts that are examined when reviewing an ECG recording. These artifacts include the P-wave, Q-wave, R-wave, S-wave, and T-wave [16, 17].

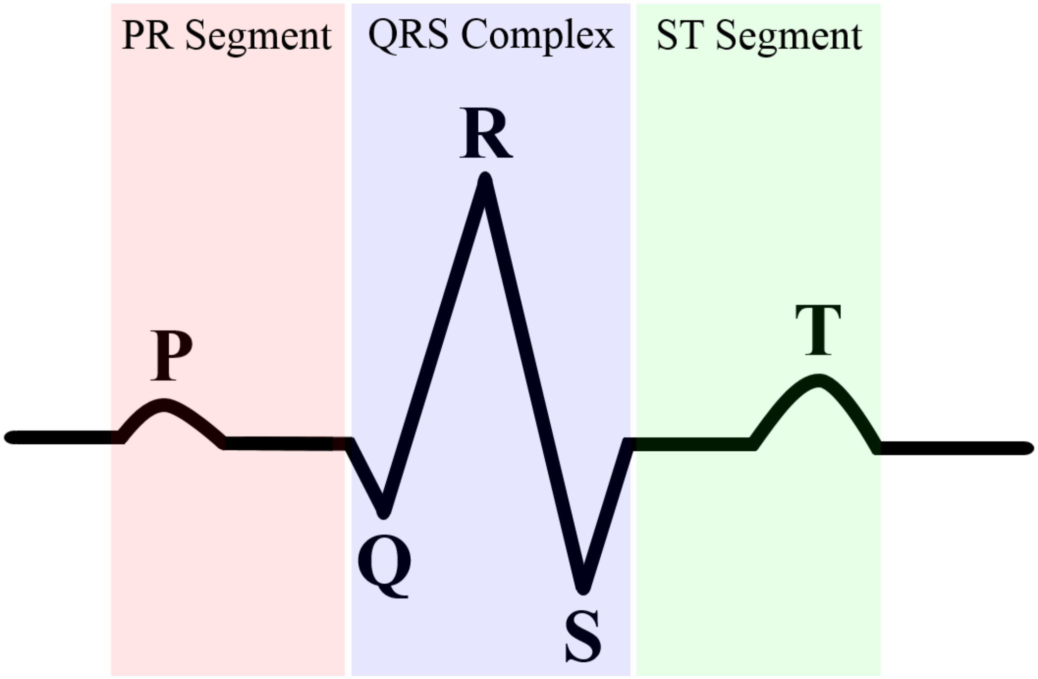

**Figure 2.2:** ECG morphology of one cardiac cycle.

#### 2.2.3.1 Morphology & Artifacts

Precedent to the P-wave, the SAN sends out an electrical signal. The P-wave indicates atrial depolarization or atrial contraction. During the Q-wave, R-wave, and S-wave ventricular depolarization takes place which results in blood being pumped to the lungs and body; the grouping of these three waves are typically called the QRS complex. It is important to note that the R-wave is utilized to calculate the heart rate in various cardio based machines such as treadmills and ellipticals. Finally, ventricular relaxation occurs which is signified by the T-wave [16, 17]. Significant mechanical function and electrical conduction at each ECG artifact are highlighted in Table 2.1.

**Table 2.1:** Electrocardiogram Artifacts I

| **Artifact** | **Mechanical** | **Electrical** |
|---|---|---|
| *P-wave* | atrial contraction | atrial depolarization |
| *Q-wave* | - | depolarization of interventricular septum |
| *R-wave* | ventricular contraction | ventricular depolarization of main mass |
| *S-wave* | ventricular contraction | ventricular depolarization completed |
| *T-wave* | ventricular relaxation | ventricular repolarization |

One can extract more information using the segments between existing artifacts. The PR segment, QRS complex, QT segment, and RR-interval are used for cardiac health evaluation in the medical field [16, 17].

The duration of the PR segment indicates the conduction time through the AVN. The conduction time of the AVN must be faster than the frequency at which the SAN sends a signal in order for the SAN and AVN to continue working in concert [16, 17]. Or else signal aliasing, so to speak, in the heart would result in cardiac arrhythmia or death depending on the severity.

The QRS complex marks the initial to complete depolarization of the ventricles which narrates the electrical conduction speed of the ventricles. The QT segment signifies a time approximation of ventricular depolarization; i.e. the duration of a heartbeat. The shorter the QT segment, the faster the heart rate and vice versa. See Table 2.2 for tabulated information.

**Table 2.2:** Electrocardiogram Artifacts II

| **Artifact** | **Electrical Conduction** |
|---|---|
| *PR segment* | through the AVN |
| *QRS complex* | inital ventricular depolarization |
| *QT segment* | overall ventricular depolarization |
| *RR interval* | heartbeat to heartbeat |

#### 2.2.3.2 RR-interval

The RR-interval indicates the approximate time in between each heartbeat [17]. A single RR-interval quantitatively defined as,

$$RR_n = R_{i+1} - R_i \tag{2.1}$$

where $n$ is the RR-interval index and $i$ is the R-wave index. An illustration of a single RR-interval is shown in Fig. 2.1

The compilation of RR-intervals creates a time series which is indicative of heart health. This RR-interval time series is the quantitative definition of HRV and is defined as,

$$RR_{int} = RR_1, RR_2, RR_3, ...RR_{N-1} \tag{2.2}$$

where N is the total number of R-waves. In Chapter 5 and Chapter 6, these RR-interval time series are referred to as HRV.

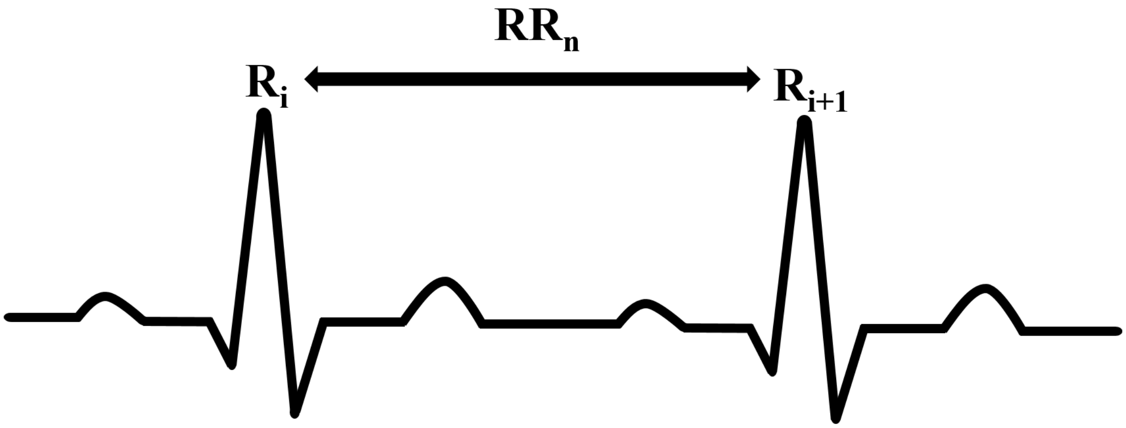

**Figure 2.3:** Generalized illustration of the RR-interval.

# Chapter 3

# MATHEMATICAL PRELIMINARIES

## 3.1 Self-similarity

Objects that contain irregular and fragmented patterns cannot be described by traditional geometry. Such objects are said to have a fractal geometry and often referred to as fractals [18]. Many fractal objects contain some degree of self-similarity [3, 19]. Self-similarity refers to spatial or temporal invariance in distribution under a suitable change of scale [20]. One can also think of self-similarity as a property where the whole or global portion has the same shape as one or more local portions. The broccoli shown in Fig. 3.1 is an example of spatial self-similarity. It shows how the global portion has a similar shape as its smaller components; it is literally similar to itself. Note that each smaller component of the broccoli is derived from the piece to its respective adjacent left side.

**Figure 3.1:** Example of geometric self-similarity: broccoli.

Self-similarity is not only seen spatially, but also temporally. Similar to fractals, the Weierstrass function, defined as $\sum_{k=0}^{\infty}[a^k cos(2\pi b^k x)]$, exhibits self-similarity. In Fig. 3.2, the Weierstrass function is graphed and a portion is magnified to help illustrate self-similarity and scale invariance.

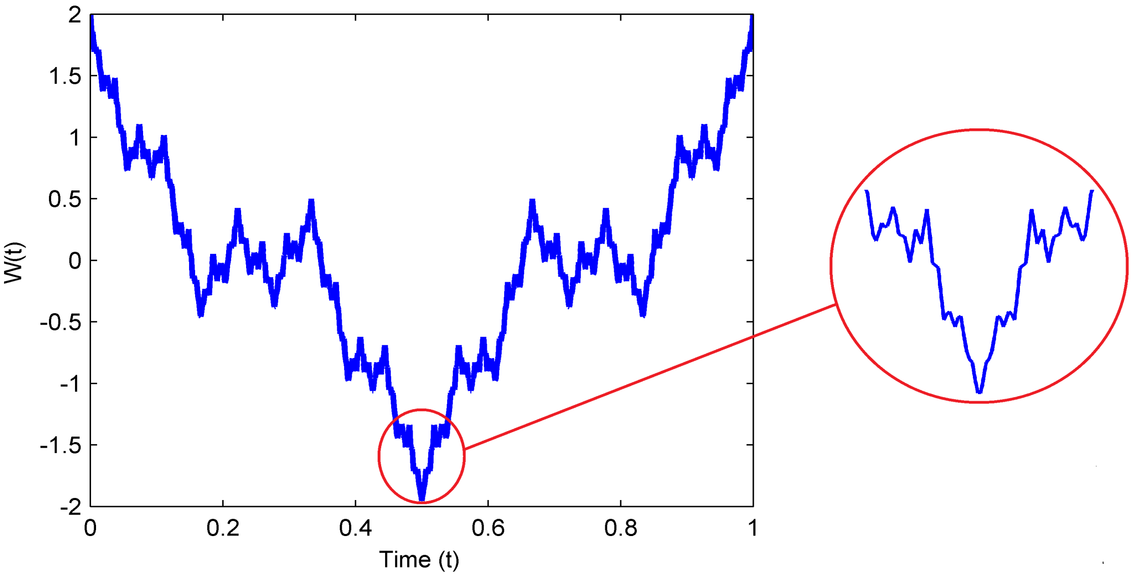

**Figure 3.2:** Example of temporal self-similarity: Weierstrass function.

Furthermore, one can think of a self-similar signal as a fractional Brownian motion (fBm) [3]. Assuming that the fBm is truly self-similar, local properties are reflected in global properties. These local and global properties are denoted as the fractional dimension ($D$) and Hurst exponent ($H$), respectively [21,22]. This results in the celebrated relationship,$D = n + 1 - H$, where n is number of dimensions for a self-similar surface [21,22]. In the case for a time series [22], $n = 1$, which simplifies to $D = 2 - H$. However, in other cases where the time series is not self-similar the fractional dimension and Hurst are independent of each other [21–23]. A formal definition of fBm is given by [2],

$$B_H(t) = B_H(0) + \frac{1}{\Gamma(\alpha)}\left\{ \int_{-\infty}^{0} \frac{d(s)}{(t-s)^{1-\alpha} - (-s)^{1-\alpha}} + \int_{0}^{t} \frac{d(s)}{(t-s)^{1-\alpha}} \right\}, \tag{3.1}$$

where

$$\alpha = H + \frac{1}{2}. \tag{3.2}$$

In Eq. 3.1, increments may or may not be independent of each other. The scaling exponent ($H$), captures the statistical complexity of the fractal process or system. The scaling exponent, also referred to as the Hurst exponent or Hurst parameter.

In this thesis, only temporal self-similarity will be discussed. The notion of self-similarity is key to understanding the underlying mathematical concept of the phenomenon known as long range dependence (LRD) [20].

## 3.2 Long Range Dependence

In the early to mid 1900s, a hydrologist by name Harold Edwin Hurst developed the notion of LRD to help determine optimal dam sizing for the Nile river [24]. Eventually the utilization of LRD was not only found in hydrology, but in other fields of study such as economics [25] and biology [26]. Multiple mathematical definitions of LRD exist. Two commonly used definitions of LRD are explained in the proceeding sections where LRD will be defined in terms of autocorrelation function (ACF) and spectral density in time and frequency domain, respectively [27, 28].

### 3.2.1 Autocorrelation Function

Consider the following self-similar time series, $\{x_t : t \in \mathbb{N}\}$ with length of $T$. Let the ACF, $\rho(k)$, with lag $(k)$ of our time series $(x_t)$ to be defined as [27],

$$\rho(k) = \frac{E[(y_t - \mu)(y_{t+k} - \mu)]}{\sigma^2}, \tag{3.3}$$

where $\mu$, $\sigma^2$, and $E[\ ]$ is the mean, variance, and expected value, respectively. In the case that,

$$\sum_{k=-\infty}^{k=\infty} \rho(k), \tag{3.4}$$

diverges, the time series is considered to be LRD. This divergence is illustrated by an ACF with a power law like decay and heavy tailness. Consequently, the ACF can be characterized by the following relationship,

$$\rho(k) \sim Ck^{-\alpha}, \tag{3.5}$$

where $C > 0$, $k$ is ACF lag, and $\alpha \in (0, 1)$; note that the symbol $\sim$ stands for asymptotically equal. The power law index is given by [27],

$$\alpha = 2 - 2H. \tag{3.6}$$

Therefore, the ACF behaves like an inverse power law which implies a slower loss of memory or correlation compared to exponential decay [26]. Ultimately, resulting in the celebrated relationship between $\alpha$ and Hurst exponent $(H)$,

$$H = 1 - \frac{\alpha}{2}. \tag{3.7}$$

where $\alpha \in (0, 1)$ and $H \in (0, 1)$. With respect to the time domain, one can think of LRD as a high degree of correlation between distantly separated data points, measured using high lags of the ACF [27].

#### 3.2.1.1 Correlation

Simulated fractional Gaussian noise (fGn) with a data length of 4096, $\sigma^2 = 0.2$, and $H \in 0.1, 0.5, 0.9$ is used to illustrate anti-persistent, Wiener, and persistent processes or signals. The statistical importance of LRD lies within the ACF. A signal with LRD in it will have an ACF that decays like an inverse power law and is characterized by heavy tailedness as shown in Fig. 3.5. In a signal, LRD is present when $H \in (0.5, 1)$. The intensity of LRD will vary based on the Hurst exponent. In theory, LRD is most intense when $H = 1$ and decreases in intensity as the Hurst exponent tends towards 0.5 but not being equal to 0.5. See Table 3.1 for statistical properties of the Hurst exponent [27].

**Table 3.1:** Statistical Properties of Hurst Exponent

| **Hurst** | **Statistical Correlation** | **Long Range Dependence?** |
|---|---|---|
| $0 \leq H < 0.5$ | Negatively correlated | no |
| $H = 0.5$ | none/stochastic | no |
| $0.5 < H \geq 1.0$ | positively correlated | yes |

#### 3.2.1.2 Anti-persistent Process ($0 < H < 0.5$)

Hurst exponent under 0.5 is considered be anti-persistent. An anti-persistent process can be thought of as a process that does not follow any particular trend. The autocorrelation graph in Figure 3.3 illustrates equally distributed correlation above and below zero. As the Hurst exponent tends towards zero, the intensity of anti-persistency increases and vice versa [27, 28].

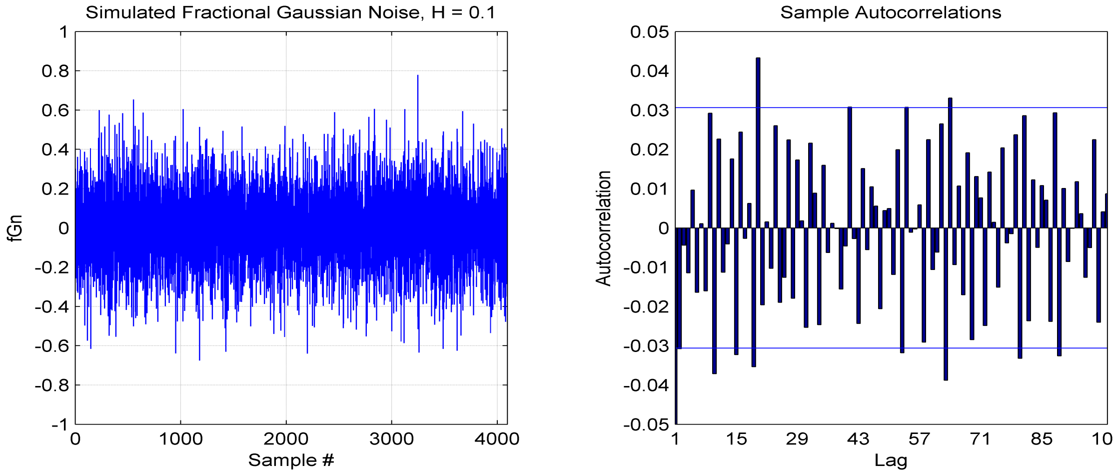

**Figure 3.3:** Raw data and sample autocorrelation of simulated fGn, $H = 0.1$

#### 3.2.1.3 Wiener Process ($H = 0.5$)

At exactly $H = 0.5$, the signal is considered a completely random or Wiener process. The random distribution of correlation as shown in the autocorrelation graph in Figure 3.4 verifies that this signal is indeed a Wiener process [29].

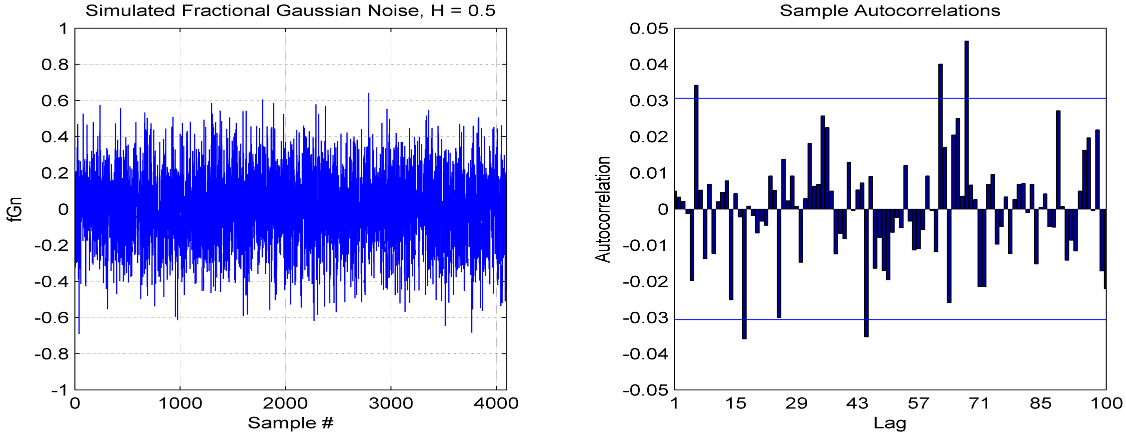

**Figure 3.4:** Raw data and sample autocorrelation of simulated fGn, $H = 0.5$

#### 3.2.1.4 Persistent Process ($0.5 < H < 1$)

When the Hurst exponent is $H \in (0.5, 1)$, it is considered a long range dependent or persistent process. It is crucial to note that the higher the Hurst exponent is, the higher the intensity of LRD is present in the signal. Conversely, if a Hurst exponent value is tending toward 0.5 from the persistent side, then persistent characteristics begin to fade and conform to more of a stochastic nature [27, 28].

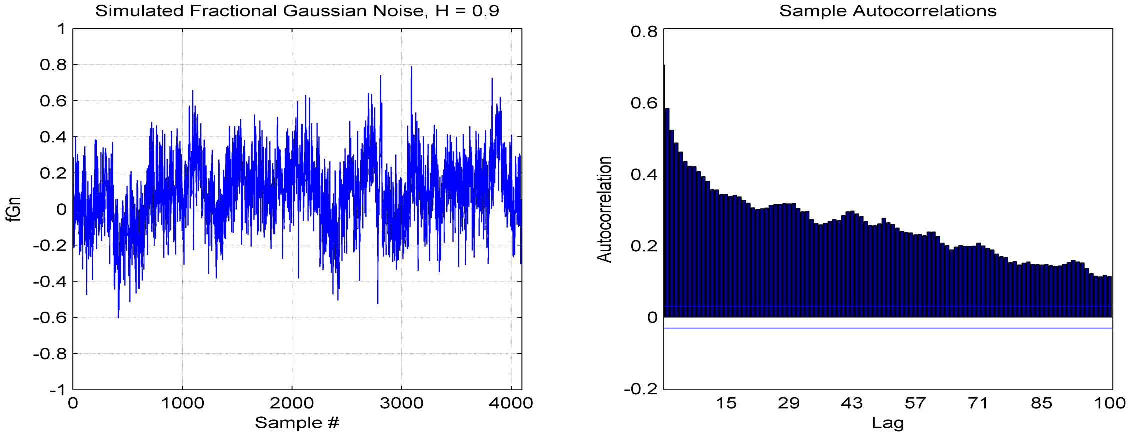

**Figure 3.5:** Raw data and sample autocorrelation of simulated fGn, $H = 0.9$

### 3.2.2 Spectral Density

Assuming that ACF definition holds true, the LRD can be defined in the frequency domain by evaluating the spectral density, $f(\lambda)$, of both variance ($\sigma^2$) and ACF, $\rho(k)$, [27,28]. This is given by the following equation,

$$f(\lambda) = \frac{\sigma^2}{2\pi} \sum_{k=-\infty}^{\infty} \rho(k) e^{ik\lambda}, \tag{3.8}$$

where $\lambda$ and $i$ is frequency and $\sqrt{-1}$, respectively. The following relationship exists if time series is LRD [27],

$$f(\lambda)\ C|\lambda|^{-\beta}, \tag{3.9}$$

as $\lambda \to 0$ where $C > 0$ and some real $\beta \in (0,1)$. The power law index is given by $\beta = 2H - 1$. Consequently, the relationship between the $\beta$ exponent and Hurst exponent ($H$) is described as such,

$$H = \frac{1+\beta}{2}. \tag{3.10}$$

where $\beta \in (0,1)$ and $H \in (0,1)$. Herein, LRD manifests as a significant level of power at frequencies close to zero in the frequency domain [27].

## 3.3 Hurst Estimators

The Hurst exponent ($H$), also known as the Hurst parameter, is a quantitative index that measures the level of LRD present in a self-similar signal; where $H \in [0,1]$. Statistical properties of LRD are not present when $H \in [0,0.5]$. In the case that $H \in (0.5,1]$, some level of intensity of LRD is present [24]. It is important to note that larger values of the Hurst exponent when $H \in (0.5,1]$ results in a higher intensity of LRD present in the signal [28,30].

Numerous methods exist to estimate the Hurst exponent which can be used to characterize LRD [5,24,28,30]. Herein, six Hurst estimators are utilized: aggregated variance method, absolute value method, difference variance method, diffusion entropy method, Peng's method, and rescaled range method. The performance of each method varies with respect to accuracy and robustness [30,31]. This is due to the difference in mathematical approach that each method is centered upon. For example, the aggregated variance method is based on a dispersional analysis [32] while Peng's method uses fractional Brownian motion [24]. In addition, some methods offer specific analytical strengths and weaknesses, for example, the difference variance method is able to detect common non-stationary processes, however, it also introduces additional fluctuation while estimating the Hurst exponent [24].

All Hurst estimators were used in Chapter 5 to help determine the most optimal Hurst estimator for differentiating between normal and abnormal heart rate variability. In Chapter 4 and Chapter 6, only the diffusion entropy method is used due to it's ability to work with smaller data sets [33].

### 3.3.1 Data Aggregation Technique

A multitude of Hurst estimators utilize data partitioning techniques known as the data aggregation [24]. In this thesis, all Hurst estimators with the exception of diffusion entropy method use data aggregation. The diffusion entropy method uses a different method of partitioning the data for analysis; this is explained in the Diffusion Entropy Analysis section of this chapter.

This aggregation procedure is indicative of the self-similarity concept. The global or overall data is proportionally partitioned off into smaller segments. The Hurst estimators analyze these smaller data segments and compares the statistical characteristics between segments to determine quantitative similarity.

Herein, a simple explanation of how to aggregate data into an aggregated data series is given. Consider the time series, $\{X_t : t \in \mathbb{N}\}$ with length of $T$. Divide the time series into [T/m] units of block size $(m)$ with block index $(k)$ amount of units such that $k = 1, 2, 3, ..., [T/m]$. In Fig. 3.6, each row is considered an aggregated series. The aggregated series is formally defined as [24, 30, 32],

$$X_k^{(m)} = \sum_{i=(k-1)m+1}^{km} X(i). \tag{3.11}$$

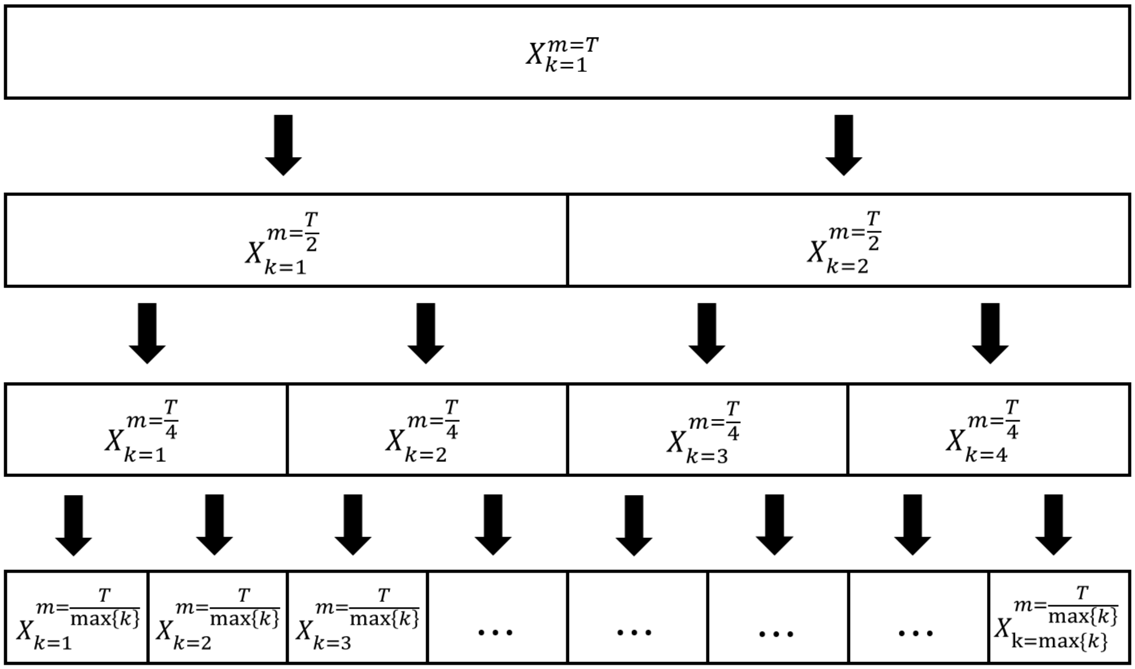

**Figure 3.6:** Generalized illustration of data aggregation.

### 3.3.2 Aggregated Variance Method

The aggregated variance method begins with aggregating the orginal time series $\{X_t : t \in \mathbb{N}\}$ with length of $T$. Each block of the aggregated series, $X_k^{(m)}$, is then averaged by dividing by the block size ($m$). This aggregated series is defined as such [5, 24, 30, 32],

$$X_k^{(m)} = \frac{1}{m} \sum_{i=(k-1)m+1}^{km} X(i), \tag{3.12}$$

where block index ($k$) is $k = 1, 2, 3, ..., [T/m]$. Sample variance of the aggregated series is defined in Eq. (3.13).

$$aggvar(i) = \widehat{Var}(X^{(m)}) = \left[\frac{1}{T/m} \sum_{k=1}^{[T/m]} \left(X_k^{(m)}\right)^2\right] - \left[\frac{1}{T/m} \sum_{k=1}^{[T/m]} X_k^{(m)}\right]^2 \tag{3.13}$$

When the sample number is large enough as $m \to \infty$, we obtain the following equation, $\widehat{var}(X^{(m)}) \sim \sigma^2 m^\beta$; where $\sigma$ is the scale parameter and $\beta = 2H - 2 < 0$ [5,24,30,32]. This results in the following mathematical corollary seen in Eq. (3.14).

$$H = 1 - \frac{\beta}{2} \tag{3.14}$$

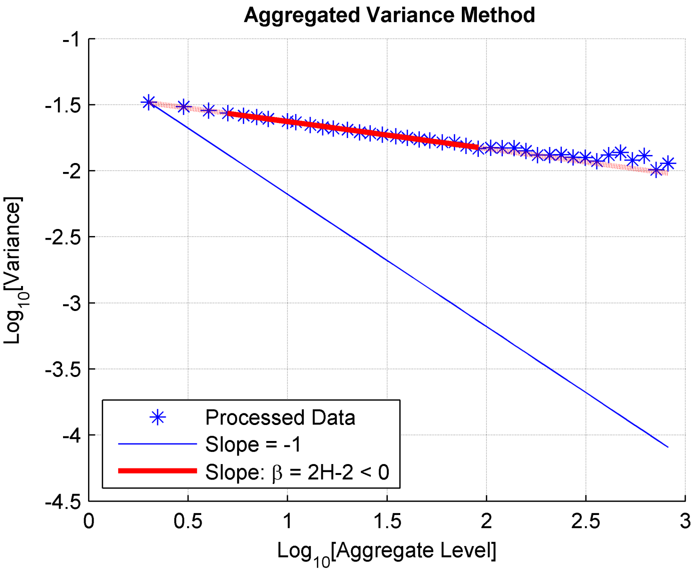

**Figure 3.7:** Log-log plot of aggregated variances.

### 3.3.3 Absolute Value Method

Similar to the aggregated variance method, the absolute value method partitions or aggregates the data exactly shown in Eq. (3.12). However, instead of calculating the sample variance, the sum of the absolute values of the aggregated series, $X_k^{(m)}$, is taken and then averaged by max block index ($k$), or $[T/m]$ of that series. The absolute value method is defined by the following [5, 24, 30],

$$absval(i) = \frac{1}{T/m} \sum_{k=1}^{T/m} |X_k^{(m)}(k)|. \tag{3.15}$$

If the data is found to have LRD characteristics, then the slope of the log-log plot should be $\alpha = H - 1 < 0$. As a result of this corollary, the Hurst exponent can be calculated using,

$$H = 1 + \alpha. \tag{3.16}$$

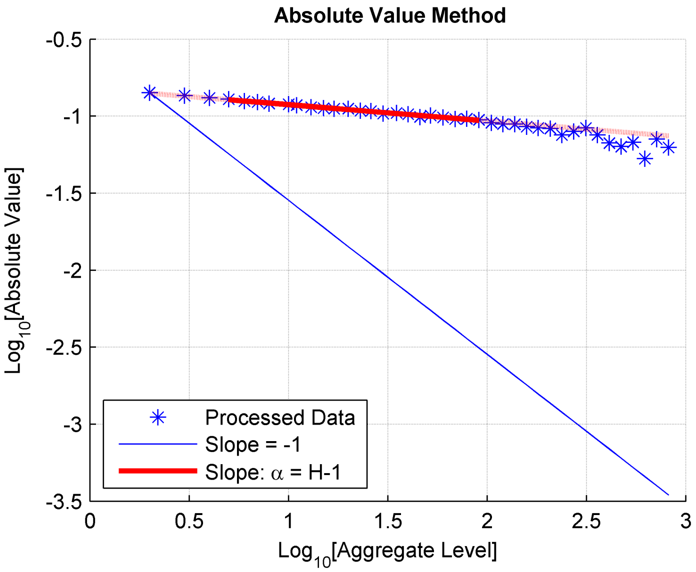

**Figure 3.8:** Log-log plot of absolute values.

### 3.3.4 Difference Variance Method

The difference variance method is known to identify common types of non-stationary processes. This includes non-stationary processes that contain slow decaying trends as well as large shifts in mean [34]. Similar to the aggregated variance method, the data is aggregated as shown in Eq. (3.12) and the sample variance, $\widehat{Var}(X^{(m)})$, of the aggregated series is computed as well. Next, the differences between tandem sample variances are calculated like [5, 24, 30],

$$Z(i) = [X(2) - X(1), X(3) - X(2), ..., X(T) - X(T-1)]. \tag{3.17}$$

This differencing between adjacent variances is the foundation of the difference variance method and can be concisely written as,

$$diffvar(i) = \widehat{Var}X^{(m_{i+1})} - \widehat{Var}X^{(m_i)}, \tag{3.18}$$

where values of $m$, $\{m_i, i \geq 1\}$ that are equidistant on a log scale such that $m_{i+1}/m_i = C$. The constant $(C)$ is contingent on the length of the time series [24]. The log log plot will have a slope $\beta = 2H - 2 < 0$, same as the aggregated variance method. Thus resulting in the Hurst equation which is defined as [24],

$$H = 1 - \frac{\beta}{2}. \tag{3.19}$$

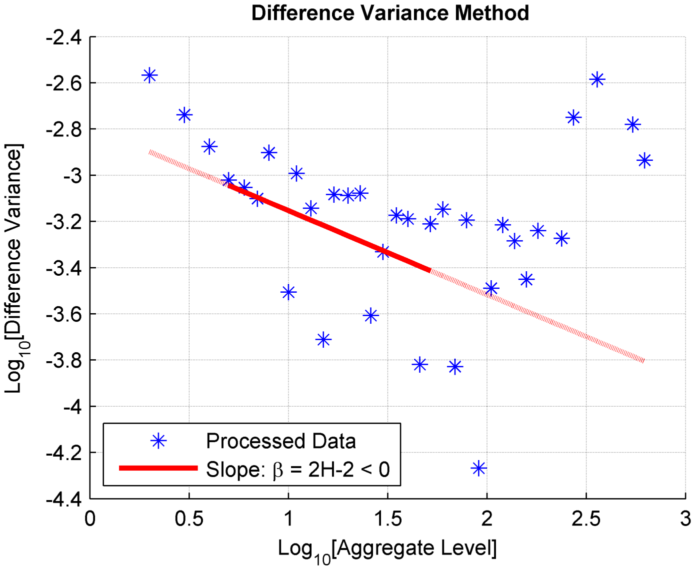

**Figure 3.9:** Log-log plot of difference variances.

### 3.3.5 Diffusion Entropy Analysis

The diffusion entropy analysis method is able to effectively estimate the Hurst exponent, also known as the scaling exponent, for data that may contain detrending characteristics [30]. The existence of the Hurst exponent implies the existence of a probability density function (PDF), $p(x,t)$, which is defined as [5, 30, 33]:

$$p(x,t) = \left(\frac{1}{t^H}\right) F\left(\frac{x}{t^H}\right) \tag{3.20}$$

where the $H$ is the PDF scaling exponent. The imperative equation to determine PDF scaling exponent reads:

$$S(\tau) = A + H\tau, \tag{3.21}$$

where

$$S(t) = -\int_{-\infty}^{\infty} p(x,t) ln[p(x,t)] dx, \tag{3.22}$$

$$A \equiv -\int_{-\infty}^{\infty} F(y) ln[F(y)] dy, \tag{3.23}$$

and

$$\tau = ln(t). \tag{3.24}$$

In this method the slope of the semi-log plot, log of diffusion entropy trajectories over the aggregated levels, is the equal to the Hurst exponent.

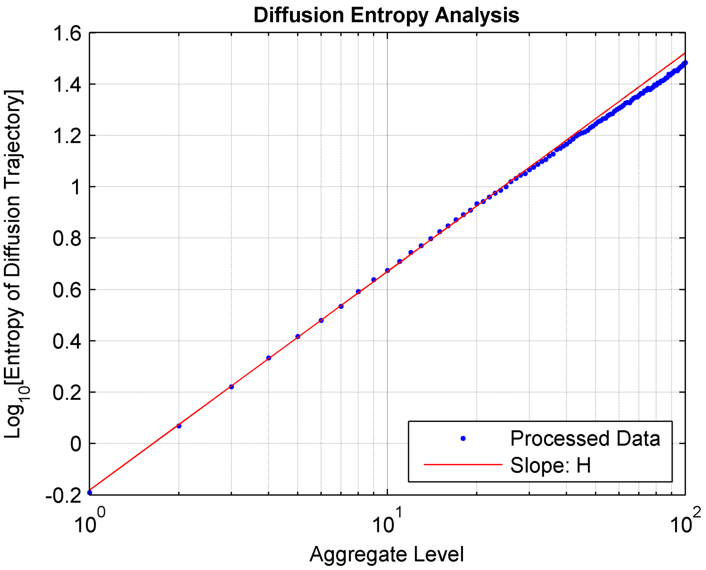

**Figure 3.10:** Semi-log plot of diffusion entropy trajectories.

### 3.3.6 Peng's Method

Peng's method is also known as the variance of residual method. In this method the data is aggregated as shown in Eq. (3.11). For each block the partial sums are calculated and then a least-squares line, $a + bt$, is fitted to the partial sums [5, 24, 30].

$$\frac{1}{m}\sum_{t=1}^{m}(Y(t) - a - bt)^2 \tag{3.25}$$

The calculated sample variance of the residuals is proportional to $m^{2H}$. The slope of the least squares line is defined as [5, 24, 30],

$$\beta = 2H, \tag{3.26}$$

which gives us the following relationship,

$$H = \frac{\beta}{2}. \tag{3.27}$$

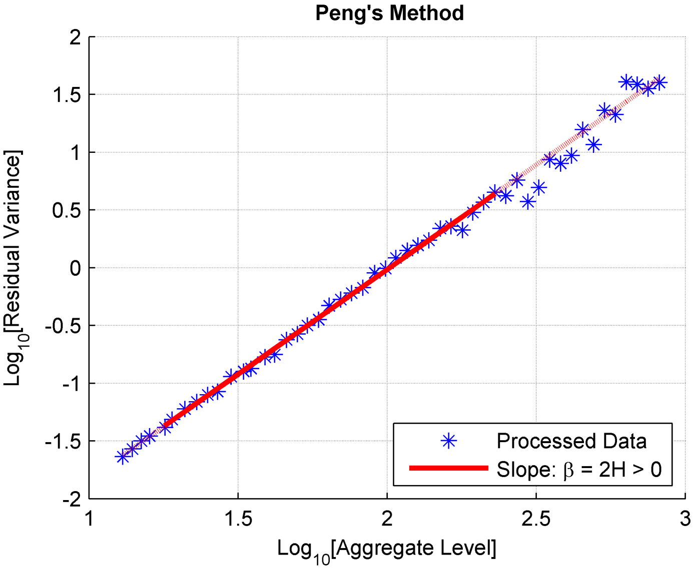

**Figure 3.11:** Log-log plot of residual variances.

### 3.3.7 Rescaled Range Method

In mid 1900s, Harold Edwin Hurst introduced a technique called the rescaled range method, popularly known as the R/S method. The data is aggregated as shown in Eq. (3.11). The maximum residual and minimum residual are subtracted from each other, for each block, to create the residual range, $R(n)$, [5, 24, 30, 35],

$$R(n) = \mathrm{Max}_k \sum_{i=1}^{k} (x_i - \bar{x}_n) - \mathrm{Min}_k \sum_{i=1}^{k} (x_i - \bar{x}_n). \tag{3.28}$$

The standard deviation, $S(n)$, of each block is computed and is defined as,

$$S(n) = \sqrt{\frac{1}{n} \sum_{i=1}^{n} (x_i - \bar{x})^2}. \tag{3.29}$$

The expected value, $E[\ ]$, of the rescaled range, $[R(n)/S(n)]$, yields,

$$E\left[\frac{R(n)}{S(n)}\right] = Cn^H\ , \tag{3.30}$$

as $n \to \infty$; where $C$ is a constant and n is the number of data points in the time series. The Hurst exponent is defined in terms of an asymptotic characteristic of the rescaled range as a function of the time span for a given time series [5, 24, 30].

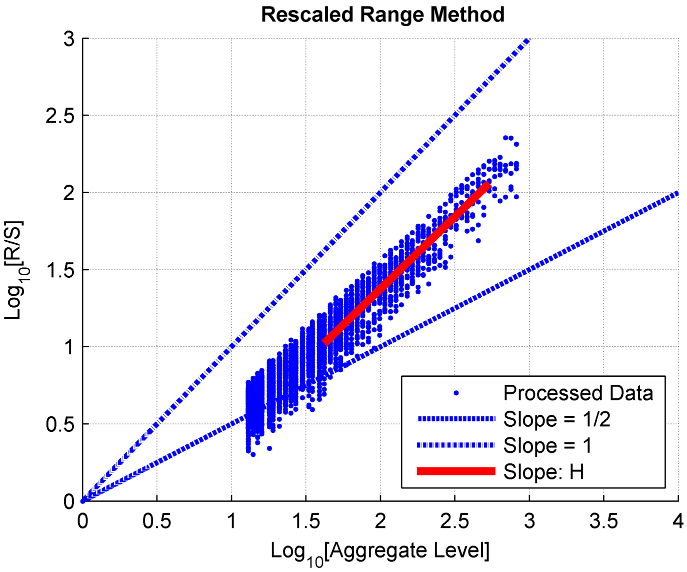

**Figure 3.12:** Log-log plot of rescaled range.

# Chapter 4

# LONG RANGE DEPENDENCE DETECTION USING HURST MAPPING TECHNIQUE IN THERMAL INFRARED IMAGING FOR POTENTIAL NONUNIFORM CORRECTION ALGORITHM

## 4.1 Introduction

Both the human eye and thermal infrared (TIR) cameras utilize electromagnetic radiation to visualize images, however, the human eye can only view within the visible light spectrum while TIR cameras can detect heat energy radiation which is not visible by the human eye [36]. Heat energy radiation is electromagnetic radiation with a lower frequency and longer wavelength [8, 9]. Similar to the retina in an eye, the TIR cameras uses focal plane array (FPA) to generate an image. The FPA is composed of an array of infrared sensors [14].

Unfortunately, the image processing quality of the sensor array or FPA is affected by spatial nonuniformity which manifests as image noise [14,37]. This results some pixels may become darker or brighter. There exists two types of nonuniformity correction (NUC) techniques known as calibration-based [38] and scene-based [39]. The calibration-based technique uses a calibration target, usually a blackbody radiation source. A con to this technique is that the camera cannot be in use in the duration of the calibration. On the other hand, the second type of NUC known as scene-based can be used without stopping the camera's operation using algorithms to filter noise [37]. A variety of these algorithms use temperature changes to compute a reference point for all pixel.

Herein, a novel technqiue called Hurst mapping is utilized to detect long range dependence (LRD) in a selection of 825 pixel equally distributed, by every 20 pixels, over a $640 \times 480$ pixel array. The Hurst exponent ($H$) can quantify the present of LRD in a signal or time series. If a strong presence of LRD is found in these pixels, then the statistical features may be exploited for NUC purposes as a scene-based type technique [39–41]. Statistical features of LRD include power law decay of correlation, stable variance and mean over time. Essentially LRD can characterize the image noise for filtering purposes. The purpose of this chapter to detect if any LRD is present in the TIR images and illustrate the topology of the Hurst map over the pixel array. No filtering algorithms are present in this thesis.

## 4.2 Data Acquistion

The thermal pixel data was collected and processed in the Mechatronics, Embedded Systems, & Automation (MESA) Laboratory at the University of California, Merced (UCM). See Appendix A for further details.

## 4.3 Experimental Methods

Details on equipment, protocol, and the mapping technique are discussed or referenced in this section.

### 4.3.1 Equipment

Three main components were utilized in this project: TIR camera, reflectance reference target, and thermal couples with amplifier. The TIR camera used was a 9640 P-Series made by Infrared Cameras Incorporated (ICI). Specifications of this TIR camera include $-40^oC$ to $200^oC$ temperature range, $\pm 1^oC$ accuracy, and $640 \times 480$ pixel array. The reflectance reference target used was a white colored calibrated diffuse reflectance target made by Labsphere. The reflectance reference target is made out of fluoropolymer and has a nominal reflectance value of 99%. K-type thermal couples with a MAX31850K amplifier breakout board were used to measure ambient temperature also referred to as ground truthing temperature. This setup has a thermocouple accuracy of eight least significant bits (LSBs) for temperatures ranging from $-200^oC$ to $70^oC$ with a $0.25^oC$ resolution.

### 4.3.2 Protocol

An extremely detailed protocol of how to set up this experiment is explained in Appendix A. See Fig. 4.1 for an illustration of the TIR experimental layout.

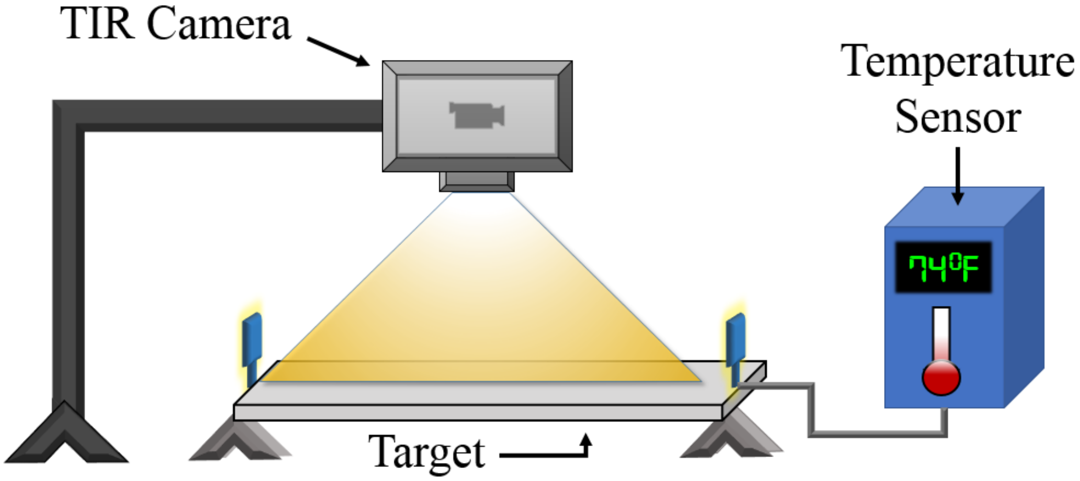

**Figure 4.1:** Thermal infrared imaging experimental layout.

### 4.3.3 Hurst Mapping Technique

This novel analytical framework called the Hurst map is explained in depth in Chapter 1, Section 2. Essentially, a Hurst exponent is calculated using Hurst estimator with respect to each pixel to construct a Hurst matrix for each TIR image. This Hurst matrix is then 3D plotted. The same technique is utilized to create variances maps, where the variance of each pixel is calculated instead of the Hurst exponent.

## 4.4 Results & Discussion

A total of eight TIR image samples were collected via experiments. Each image contains 825 pixels where individual pixels contained 1800 temperature data points. However, a rigid dichotomy between the transient and steady state is found in all image samples; see Fig. 4.2 for raw pixel data of Image #1. Therefore the data was processed using two different data sizes, 1800 and 1600. All 1800 data points were analyzed in the Transient and Steady State Section. In the Steady State Section, 1600 data points were analyzed which accounts for truncation of the initial 400 seconds or 6.5 minutes. Please note that the sample, TIR Image #1, is utilized as the sample model through this section. See Appendix B for graphical results of the rest of the image samples.

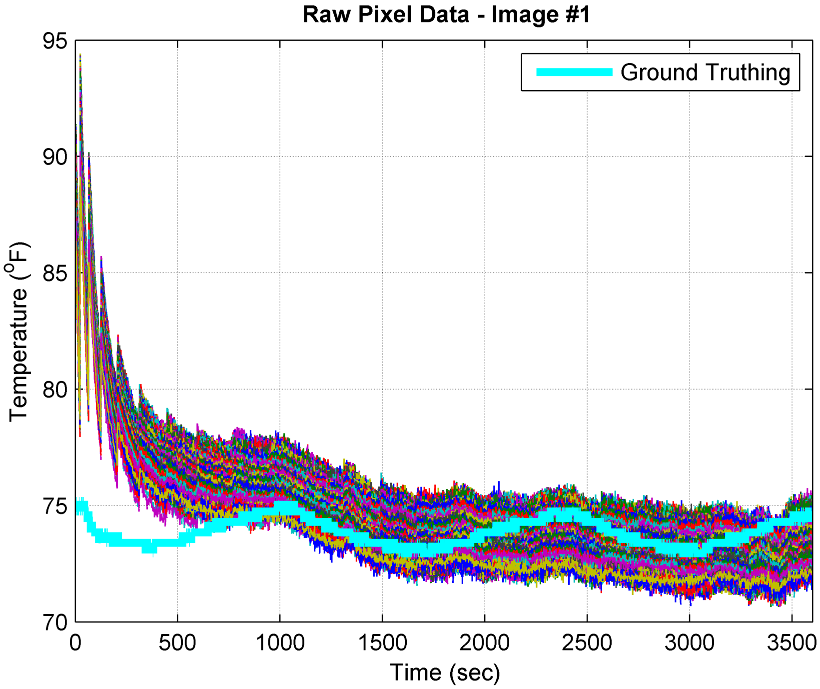

**Figure 4.2:** Raw thermal pixel data.

### 4.4.1 Transient & Steady State

All Hurst maps show a strong presence of LRD such that, $H > 0.8$, when analyzing all data. In general the correlating variance maps show an inversely proportional relationship with the Hurst exponent. Some image samples exhibited larger Hurst exponents along the perimeter of the image. However, the general morphology in the center of the Hurst maps did not show any particular trends or patterns. It is interesting to note that in Image #6, the morphology is flat in the center and that two edges of the image contain a bias of higher Hurst exponents. In addition, all variance maps displayed a blanket-like shape where the highest points are centralized and the lowest points are in all four corners; see Fig. 4.3.

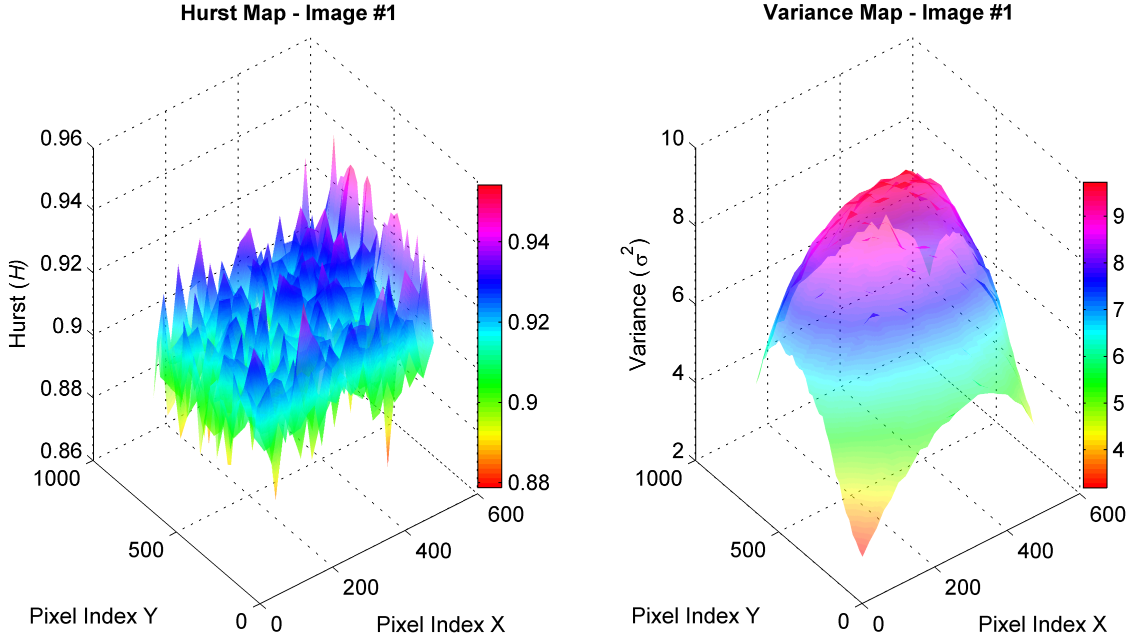

**Figure 4.3:** Hurst map and variance map of total pixel data.

### 4.4.2 Steady State

The steady state pixel data exhibited significantly higher Hurst exponents. All sample images displayed a clear bias of larger Hurst exponents along the edges of the image as shown in Fig. 4.4. It was also observed that the Hurst exponents were lowest in the center of the image. It is interesting to note that Image #6 is the only image that did not change drastically in Hurst map morphology but still increased in Hurst exponent value; especially along two edges of the image. As for the variance maps, the variances were typically lower by half in most samples with the exception of Image #6. After further review, the raw pixel data in Image #6 displayed a very short transient period.

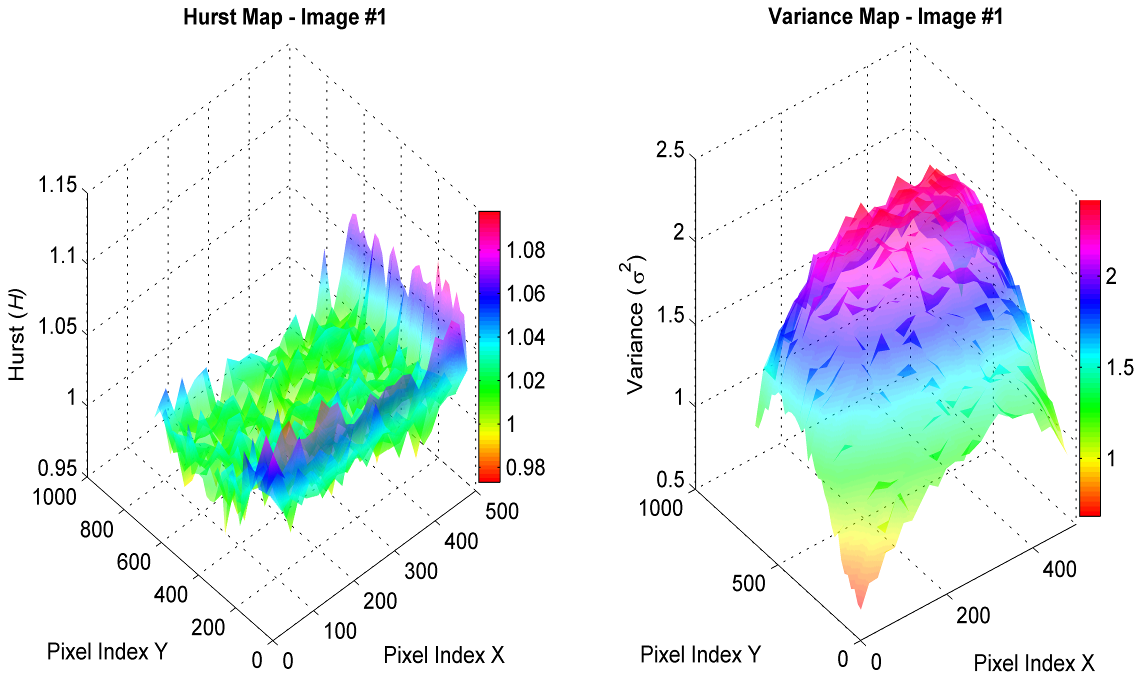

**Figure 4.4:** Hurst map and variance map of steady state pixel data.

## 4.5 Conclusion

The results highlight the strong presence of LRD within each selected pixel. All pixels, 100%, in both total and steady state analysis had a $H > 0.8$. When analyzing only steady state data, it was clearly seen that the lowest variances correlated to highest Hurst values especially along the pixel index X. This goes hand in hand with the statistical significance of LRD; the variances increase slowly as lag time increase, thus preserving memory in the thermal data. Knowing that LRD exists in these thermal images, one can exploit fractal properties from them. For example, a fractional order filter could be tuned to clean up the noise in each pixel or groups of pixels in a region. Another suggestion is using the presence of LRD for calibration purposes. The presence of LRD in the thermal pixels may decay over long periods of time without calibration and could help inform the user as well as optimize calibration scheduling.

# Chapter 5

# ARRHYTHMIA DETECTION FROM HEART RATE VARIABILITY USING HURST ESTIMATORS

## 5.1 Introduction

Heart rate and arterial blood pressure are common diagnostic measurements collected in the medical field. Unfortunately, these physiological signals are limited in their effectiveness in detecting temperate ailments such as cardiac arrhythmia which can be life threatening [16]. Cardiac arrhythmia is defined as a change in electrical activity within the heart which manifests as irregular heartbeats. Typically arrhythmias are harmless since they can be innervated by physical or mental activity. When a person experiences a transition in physical activity such as walking to running, the heart is subjected to a transient state which can be perceived as an arrthymia. Arrhythmic evaluation is not typically incorporated into general diagnostic measurements due to its commonly harmless nature. In extreme cases, arrhythmia can be induced by damaged cardiac tissue or abnormal cardiac anatomy which may lead to a stroke or heart attack [16]. Current methods to detect arrhythmias include electrocardiogram (ECG) readings and analysis [42].

The Hurst exponent, $H \in (0, 1)$, may be indicative of cardiac health [7,43]. It is known that physiological signals contain fractal properties that are associated with long range dependence (LRD) where $H \in (0.5, 1)$ [26, 44, 45]. In previous studies, the Hurst has been utilized as an index for a multitude of applications in various disciplines [4, 6, 7]. For instance, electroencephalogram signals were analyzed using a Hurst estimator to determine discrepancies in LRD at different stages of sleep [4].

In this study, six Hurst estimators are individually implemented into three algorithmic frameworks to analyze heart rate variability (HRV) for the purpose of cardiac arrhythmia dection. The three algorithmic frameworks are called total time series estimation (TSE), cumulative window estimation (CWE), and sliding window estimation (SWE) which are used for data partitioning. These algorithmic frameworks were influenced by previous studies [4, 34, 46]. The six Hurst estimators utilized are called aggregated variance, absolute value, difference variance, diffusion entropy, Peng, and rescaled range [5, 24]. Herein, it is proposed that utilizing Hurst estimators, as an additional diagnostic tool may provide an indication of cardiac arrhythmia [26, 47, 48].

## 5.2 Data Acquisition

The HRV data was obtained from PhysioNet, an online resource that offers a collection of recorded physiological signals [49]. Specifically the normal and abnormal HRV data were collected from the MIT-BIH Normal Sinus Rhythm (NSRDB) and MIT-BIH Arrhythmia (ADB) database, respectively. Both databases utilized a lead II ECG configuration for measuring cardiac electrical activity. The ECG readings were reviewed by cardiologists who manually annotated each heartbeat.

### Samples

In the NSRDB there are 18 samples with an approximate recording time of 24 hours; one sample was omitted due to data acquisition complications. Therefore, only 17 NSRDB samples were utilized. In addition, the samples in the NSRDB were truncated such that each sample had a total recording time of 30 minutes. In the ADB, there are 48 samples with a recording time of 30 minutes. See Table 5.1 for database information given by PhysioNet [49].

**Table 5.1:** Arrhythmia & Normal HRV Database Information

| **Database** | **Sample #** | **Duration (typical)** | **Signals** |
|---|---|---|---|
| mitdb | 48 | 30 minutes | ECG (2 leads) |
| nsrdb | 18 | 24 hours | ECG (2 leads) |

## 5.3 Experimental Methods

Previous studies [4,34,46] have estimated the Hurst exponent on data that has been partitioned using different algorithmic frameworks. The Hurst estimators [5] are applied to the algorithmic frameworks titled TSE, CWE, and SWE. In TSE the entire HRV time series of each sample is used to estimate the Hurst exponent. This is a common use of Hurst estimator(s) and is found in previous research, such as hydrological studies in the Nile River to determine optimal dam sizing [24]. As for the CWE, the Hurst exponent is estimated at the first minute proceeded by an incremental growth of the HRV data by one minute until the entire data is analyzed. This approach is motivated by studies [34, 46] that have presented an estimation of the Hurst exponent for different incremental sizes of data; as shown in video data traffic studies where Moving Picture Expert Group (MPEG) sequences were used to estimate the Hurst exponent for different data sizes with respect to time. In the last algorithmic framework, SWE, the HRV data is truncated with a window ($w_t$) and moves with a slide ($s_t$) of time length of $t$. The Hurst exponent is estimated for each truncated segment. A study in electroencephalogram signals utilized a sliding window method to estimate the Hurst exponent in different parts of the sleep cycle [4].

### 5.3.1 Total Time Series Estimation

The Hurst exponent $(H)$ is estimated at 30 minutes for both normal and abnormal HRV data. This method is expressed in the following equation,

$$H_{sample} = H\big[x(t)\big]_0^{30}, \tag{5.1}$$

where $H[\,]$ is a generalized Hurst method, $x(t)$ is the HRV time series, and $H_{\text{sample}}$ represents the Hurst exponent for a human sample.

### 5.3.2 Cumulative Window Estimation

A cumulative growing window is used to estimate a Hurst exponent series. The initial window size is one minute and grows by an increment of one minute until a cumulative window size of 30 minutes is achieved. At each incremental growth, a Hurst exponent is estimated. The Peng and rescaled range methods were not able to compute at one minute for the initial window, therefore both of these methods begin at two minutes. The box periodogram varied in initial window size as well. The approximate initial window size is five and six minutes for normal and abnormal HRV data, respectively. To preserve consistency for the box periodogram, the initial window is established at six minutes; thus neglecting the first five minutes of HRV data. The following equation represents the cumulative window estimation,

$$H_{sample}(t) = H\big[x(t)\big]_0^{t} \tag{5.2}$$

as $t = 1, 2, 3, ...30$. Where *H[ ]* is a generalized Hurst method, $x(t)$ is the HRV time series, and $H_{\text{sample}}(t)$ represents a series of estimated Hurst exponents for human sample.

### 5.3.3 Sliding Window Estimation

The sliding window and how it is optimized is explained in detail in Chapter 1, Section 2. The optimizing parameter $(OP)$ used was the variance of the sliding window variable $(SWV)$, which is the Hurst, for each respective combination of $w_t$ and $s_t$. The variance was selected as the $OP$ to minimize variability in $SWV$. An orthogonal view of the 3D plot with a optimized trace of $s_t$ with respect to $w_t$ for all Hurst methods are shown in in Fig. 5.1. Please note that the difference variance, Peng, and rescaled range methods were unable to calculate at $(w_t = 1,\ s_t = 1)$. In addition, the diffusion entropy method was unable to for $w_t < 3$ and their respective slides.

Using the trace line as a guide, the optimal $w_t$ and $s_t$ were chosen heuristically. Once again, refer to Chapter 1, Section 2 for the heuristic guideline to ultimately choose optimal slide and window length. The optimal combination of $w_t$ and $s_t$ for all methods are tabulated into Table 5.2. Experimental results from these optimal SWE parameters are shown in the SWE Subsection in the Results Section.

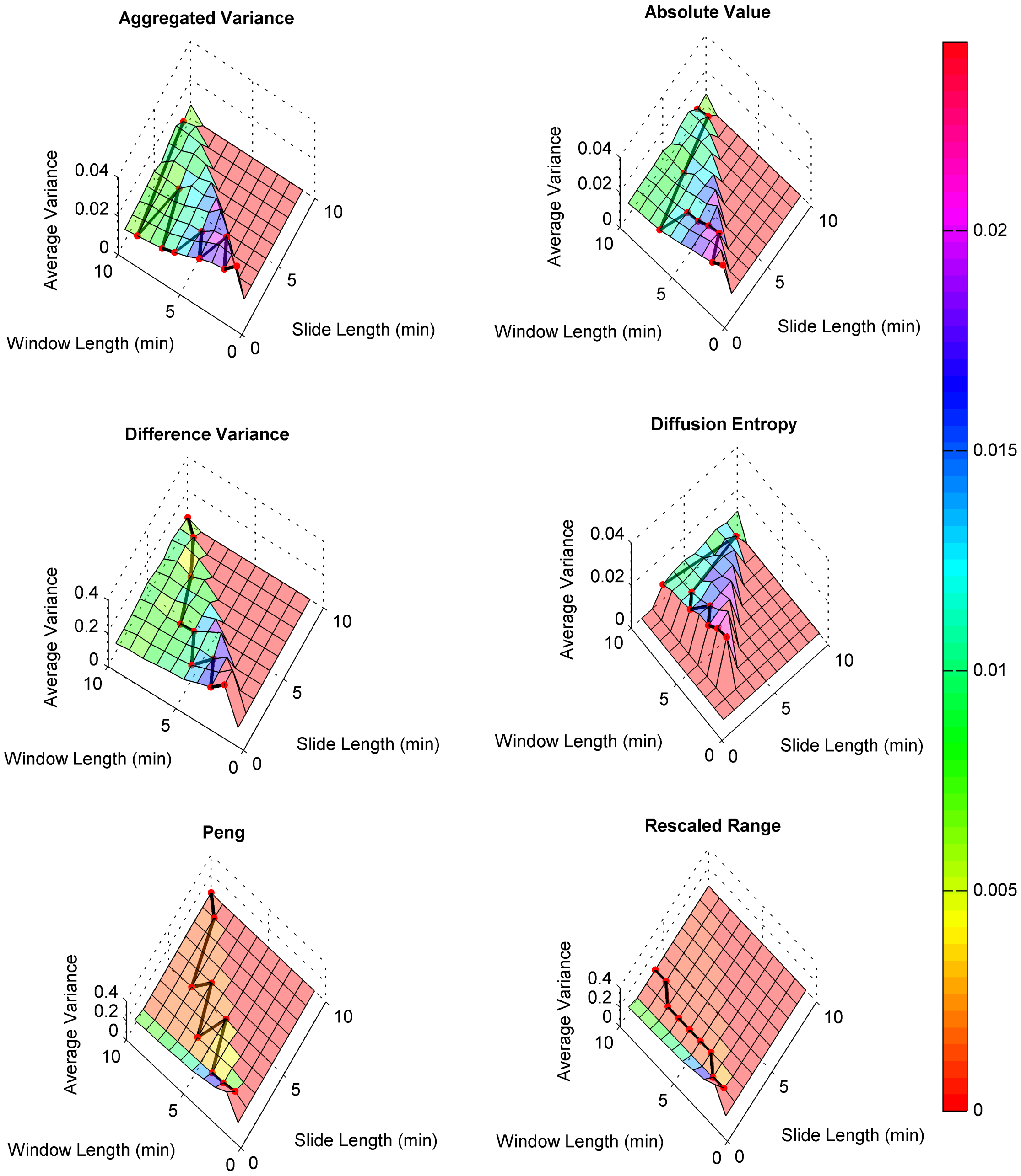

**Figure 5.1:** Orthogonal view of 3D trace line plot.

**Table 5.2:** Optimal Window ($w_t$) & Slide ($s_t$) for All Hurst Estimators

| | **Window Size $w_t$** | **Slide Size $s_t$** |
|---|---|---|
| **Aggregated Variance** | 7 minutes | 1 minutes |
| **Absolute Value** | 7 minutes | 1 minutes |
| **Difference Variance** | 7 minutes | 4 minutes |
| **Diffusion Entropy** | 7 minutes | 3 minutes |
| **Peng** | 6 minutes | 3 minutes |
| **Rescaled Range** | 5 minutes | 3 minutes |

## 5.4 Results & Discussion

The analysis of the results in this section are influenced by statistical findings, graphical tendencies, and a parameter called LRD%. The LRD% is defined as sample percentage of normal or abnormal HRV data that strictly display LRD where $H > 0.5$. For example, the Hurst series calculated for a given sample using the CWE or SWE must all have $H > 0.5$ in order to contribute to the LRD%.

### 5.4.1 Total Time Series Estimation

All methods display extremely high percentage of LRD for the bilateral HRV data; see Table 5.3. The difference variance method exhibited lower LRD% compared to the other methods, but also displays the largest drop in LRD% for the abnormal HRV data. However, a histogram of TSE processed HRV data suggests that the difference variance method is arguably the least effective next to the Peng method in differentiating between normal and abnormal HRV; see Fig. 5.2. There is a noticable segregation with some index aliasing between bilateral HRV data in the aggregated variance, absolute value, and rescaled range; these are not viable methods. The diffusion entropy histogram presents a significantly segregated index between bilateral HRV data; where 100% of abnormal indices fall below $H = 1.25$ and 94.12% of normal indices are found above $H = 1.25$. Ultimately, the diffusion entropy has proven to be the most viable method at differentiating between normal and abnormal HRV in the TSE approach.

**Table 5.3:** Total Time Series Estimation: LRD%

| | $LRD_{normal}$ | $LRD_{abnormal}$ |
|---|---|---|
| **Aggregated Variance** | 100% | 97.92% |
| **Absolute Value** | 100% | 97.92% |
| **Difference Variance** | 94.12% | 70.83% |
| **Diffusion Entropy** | 100% | 97.92% |
| **Peng** | 100% | 97.92% |
| **Rescaled Range** | 100% | 97.92% |

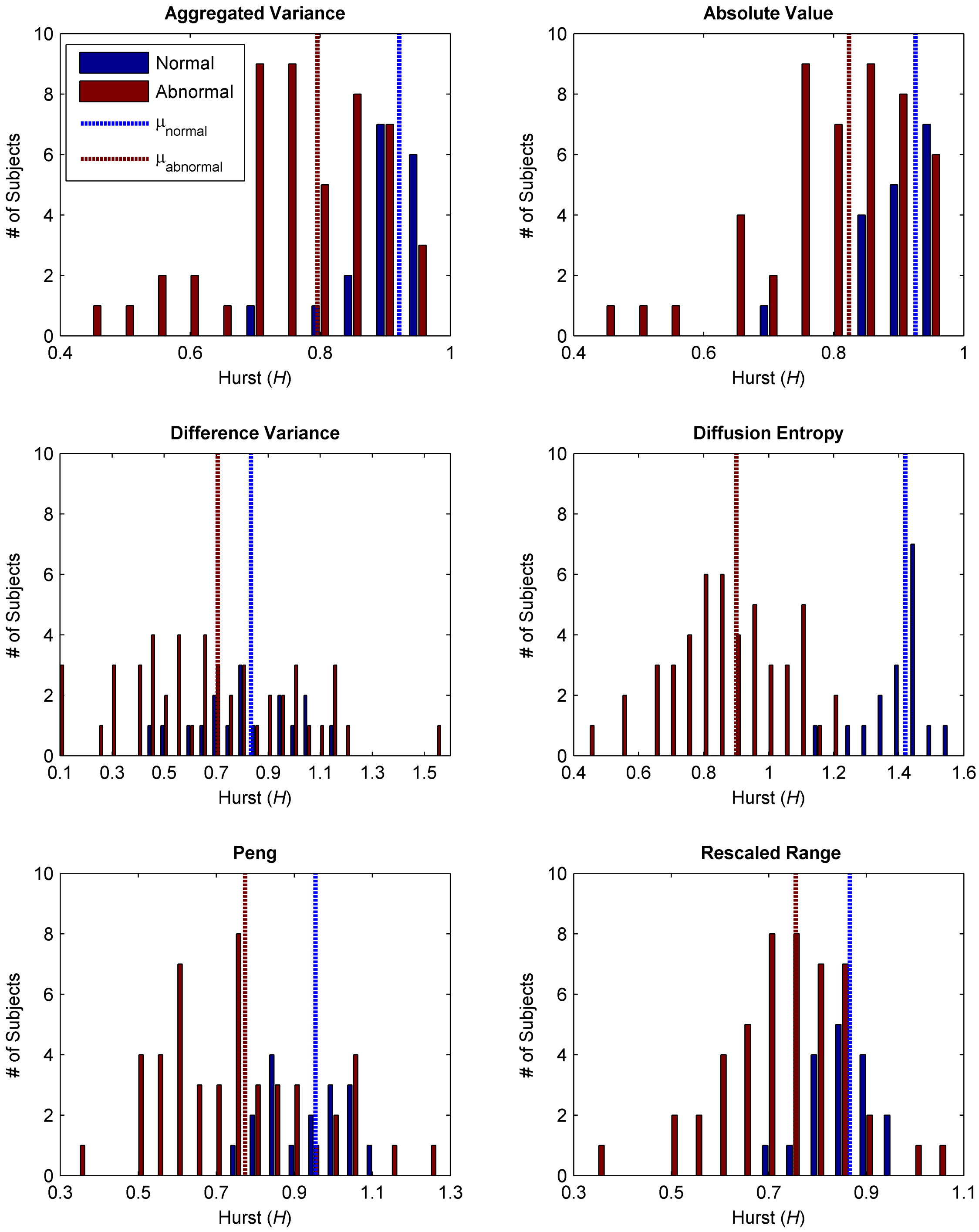

**Figure 5.2:** Histogram of all Hurst methods using TSE; bin size is 0.05.

### 5.4.2 Cumulative Window Estimation

Compared to the TSE approach, all methods show significant decreases in LRD% for abnormal HRV data. A dichotomy of high and low LRD% for normal and abnormal HRV data, respectively, is blatantly shown in Table 5.4. All methods with the exception of the difference variance, pose as a potentially useful index because of their dichotomous LRD% between normal and abnormal. In Fig. 5.3, one normal and abnormal HRV sample were compared using CWE for all methods. Results reflect that of the results from the TSE; this is no surprise since the CWE trends up to the overall Hurst exponents estimated in TSE.

**Table 5.4:** Cumulative Window Estimation: LRD%

| | *LRD_normal* | *LRD_abnormal* |
|---|---|---|
| **Aggregated Variance** | 88.24% | 41.67% |
| **Absolute Value** | 100% | 50% |
| **Difference Variance** | 29.41% | 6.25% |
| **Diffusion Entropy** | 100% | 62.50% |
| **Peng** | 100% | 35.42% |
| **Rescaled Range** | 94.12% | 58.33% |

### 5.4.3 Sliding Window Estimation

The HRV data was processed using the optimized SWE parameters in Table 5.2. The same samples employed for CWE in Fig. 5.3 are used to compare all methods using the SWE; see 5.4. Only the Peng and rescaled range exhibited a significant dichotomy between normal and abnormal in regards to LRD%. Upon review of the Hurst series, all methods were able to differentiate, to a degree, between HRV data. Unfortunately, there is a crossover between normal and abnormal indices which compromises the purpose of the index; to differentiate between normal and abnormal HRV. See Appendix B for complete sample results.

**Table 5.5:** Sliding Window Estimation: LRD%

| | *LRD_normal* | *LRD_abnormal* |
|---|---|---|
| **Aggregated Variance** | 88.24% | 60.42% |
| **Absolute Value** | 88.24% | 64.58% |
| **Difference Variance** | 47.06% | 14.58% |
| **Diffusion Entropy** | 100% | 83.33% |
| **Peng** | 88.24% | 39.58% |
| **Rescaled Range** | 100% | 52.08% |

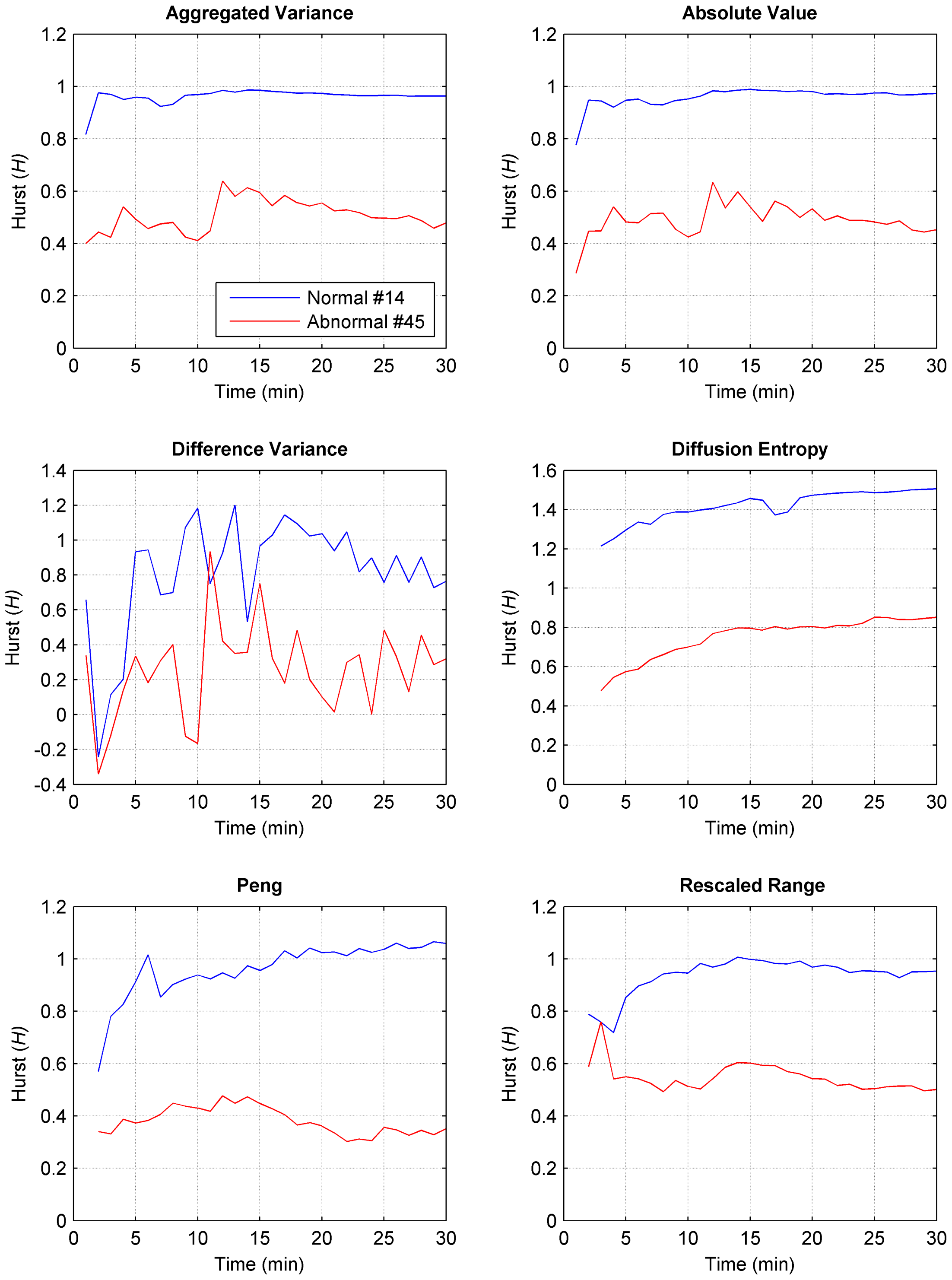
Aggregated Variance

Absolute Value

Difference Variance

Diffusion Entropy

Peng

Rescaled Range

**Figure 5.3:** Normal and abnormal HRV comparison using CWE.

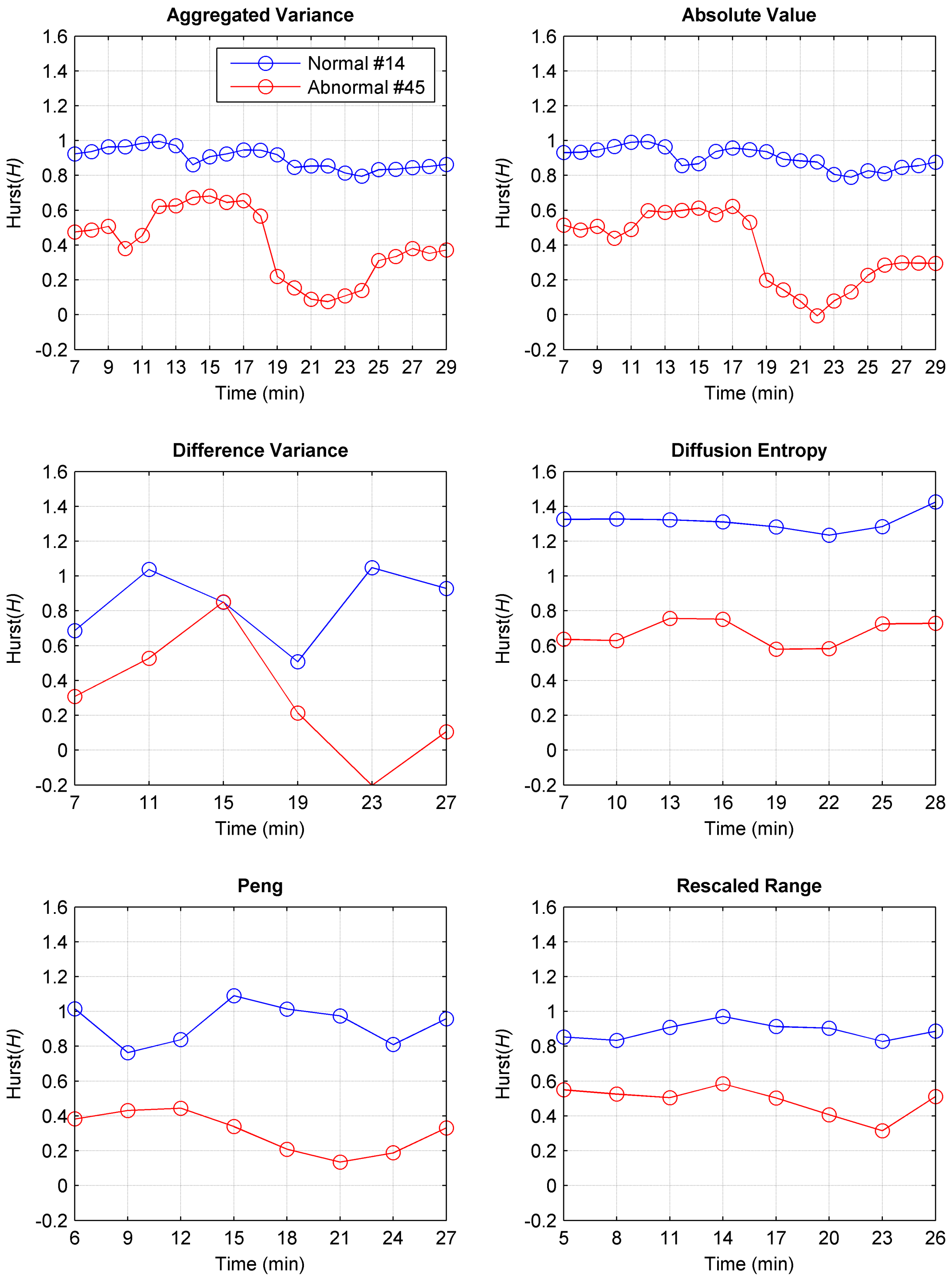

**Figure 5.4:** Normal and abnormal HRV comparison using SWE.

## 5.5 Conclusion

In this study, three approaches using seven Hurst estimation methods to differentiate between normal and abnormal HRV were evaluated. Bilateral results indicate that most HRV data exhibit LRD in all approaches. This implies that both normal HRV and abnormal HRV both have a persistent characteristic. It is paramount to note that the normal HRV typically expressed higher Hursts, indicating that normal HRV has a higher persistency than that of abnormal HRV.

The TSE approach reinforces the concept of LRD being an innate characteristic in physiological signals. Furthermore, the lower Hurst exponent seen in the abnormal HRV data is a direct result of the stochastic characteristics embedded in arrhythmias, irregular heartbeats. These stochastic characteristics compromise and reduce the presence LRD found, hence the Hurst exponent is lower in abnormal HRV. A weak division between normal and abnormal HRV Hurst distributions is apparent in the TSE histogram shown in the results section. The diffusion entropy method is the only method that significantly exhibits segregation between normal and abnormal Hurst indices. If we utilize $H = 1.25$ as an index partition in the diffusion entropy method, then 94.12% of normal and 100% of abnormal remain above and below this index partition, respectively. It would be worth wild to investigate the slight index overlap since mild or non-severe arrhythmias may have an index similar to normal HRV.

The CWE approach provides little insight on top of the TSE. This is due to the fact that the CWE trends or estimates the eventually Hust index sound in TSE. However, the CWE was able to exacerbate the anti-persistency, where $H < 0.5$, in the abnormal HRV. This shows that some sort of data partitioning is useful in analyzing the differences between normal and abnormal HRV.

The SWE approach did not exhibit any dichotomy of LRD between normal and abnormal HRV. Heuristically, the diffusion entropy seemed to be the best cardiac index. The raw SWE data, found in Appendix B, exhibited a varying degree of index overlap in regards to all methods. Further research on optimal slide and window length would have to be done to truly determine the effectiveness of this approach.

In the end, most methods were unable to significantly distinguish between normal and arrhythmic HRV completely; some normal subjects exhibited lower Hurst exponent values than that of arrhythmic subjects and vice versa. After analyzing the RR-interval of the normal and arrhythmic subjects, there are some arrhythmic subjects that have a lesser or more extreme case of cardiac arrythmia. This may have contributed to index aliasing between normal and abnormal HRV. In this study, repeatedly found through all approaches that normal HRV contains a higher intensity of LRD than that of abnormal HRV. The diffusion entropy method utilized in conjunction with the TSE approach is best at differentiating between normal and abnormal HRV.

## Chapter 6

# STRESS DETECTION FROM HEART RATE VARIABILITY USING DIFFUSION ENTROPY

### 6.1 Introduction

The biological description of stress is defined as when factors, called stressors, act on an organism and cause the body to move away from homeostasis [16, 50, 51]. When exposed to a stressor, the human body reacts by activating the autonomic nervous system (ANS) [51]. Consequently hormones such as adrenaline and epinephrine are released, catalyzing arterial vasconstriction which increases blood pressure, muscle tension and heart rate variability (HRV) [51, 52]. Principally, stress is a physiological response to physical or mental provocation [52].

Current methods of stress detection utilize single or multiple physiological signals such as galvanic skin conductance [53], blood pressure [54], muscle tension [55], respiratory activity [56], and HRV using electrocardiogram (ECG) [50, 57–59].

These methods require continuous retrieval of information, from invasive or noninvasively placed sensors, over a period of time in order to differentiate between normal and stress-induced activity. There are also psychological approaches to stress assessment that involve interviewing or questionnaires. Unfortunately, these processes are limited by the individuals ability to accurately recall their stress symptoms and thus is not the most reliable practice.

Ultimately, stress does not always manifest in an intuitive manner such as increases in blood pressure or heart rate that can be detected by medical devices or recalled by an individual. However, fractal properties in these physiological signals [47] can be exploited to detect stress. In previous physiological studies, fractional calculus has been used to model [60, 61], classify [6, 42], and analyze [48, 62] fractal properties.

The term HRV refers to the regulation of the sinoatrial node, the natural pacemaker of the heart, through the sympathetic and parasympathetic branches of the ANS [51]. HRV exhibits self-similar properties as shown in prior studies [6, 43, 45, 63]. Typically self-similar processes exhibit long range dependence (LRD) characteristics [30]. It is known that physiological signals, such as HRV, have LRD present [45, 47, 52]. Utilizing the correlation between the ANS and HRV activity in conjunction with LRD characteristics, it is possible to analyze HRV to measure the level of mental stress.

Herein, we use diffusion entropy analysis to exploit inherent fractal properties of HRV to detect mental stress of automobile drivers [59]. The HRV data was acquired from an online database called PhysioNet [49]. Sections of the HRV time series that are purely rest and purely stress were evaluated using the diffusion entropy analysis to estimate the Hurst exponent to set a Hurst baseline, which will be referred to as Hurst sectional estimation (HSE). Once a HSE is calculated, the sliding window approach is utilized to estimate the Hurst exponent of truncated portions of the HRV time series for stress detection.

## 6.2 Data Acquisition

The HRV data analyzed in this paper were obtained from the Stress Recognition in Automobile Drivers (SRAD) database which was found on PhysioNet; an online resource that offers a multitude of recorded physiological signals [49]. Herein, HRV data analyzed were derived from the ECG samples in the SRAD database. The ECG electrodes were placed in a modified lead II configuration [59].

### Data Processing

It is important to note that the SRAD database only provides raw ECG. In order to procure a HRV time series, one must obtain the time index of the each R-peak which is generally the highest peaks in the ECG then subtract neighboring R-peaks in a chronological order to extract the RR-intervals, also known as HRV. An online R-peak detector [64] was used to obtain the time index of the R-peaks which was reviewed and edited by one of the authors. The R-peaks were then differenced in tandem, which yields the HRV data. This protocol is explained in depth in Appendix A.

### Samples

The SRAD database offered 17 HRV samples of which only 13 were utilized in this study. Four samples were omitted due to processing issues for two samples, one partitioned sample, and a duplicate sample. Each sample drove a set route for approximately 50 to 90 minutes [49]. All samples were at rest, i.e. parked, for the first and last 15 minutes of the experiment [59]. The rest and drive sections are partitioned and analyzed using the diffusion entropy method.

**Table 6.1:** Stress Database Information

| **Database** | **Sample #** | **Duration (typical)** | **Signals** |
|---|---|---|---|
| drivedb | 17 | 60-90 minutes | ECG, EMG, GSR, resp |

## 6.3 Experimental Methods

There exists numerous methods to estimate the Hurst exponent, also known as the Hurst parameter. The HRV data is analyzed using diffusion entropy analysis. The diffusion entropy analysis method is able to effectively estimate the Hurst exponent for data that may contain detrending characteristics [30]. The quantitative definition of the diffusion entropy method is discussed in Chapter 3, Section 3. It is important to note that diffusion entropy analysis was chosen over all other methods due to its ability to analyze smaller amounts of data [33]. The ability to work with smaller data is crucial for algorithmic frame work of the sliding window approached utilized.

### 6.3.1 Hurst Sectional Estimation

The HRV time series data used in this study was partitioned into three sections: first rest ($R_1$), drive ($D$), and last rest ($R_2$). For a given time ($t$) in minutes with length ($N$), $t = 1, 2, 3.....N$. Now consider $x(t)$ as the HRV time series where $x(t) = x_1, x_2, x_3...x_N$. As mentioned before, the first and last rest sections are each 15 minutes. The drive section is a variable length dependent on how long each participant took to drive through the route in each sample. The HSE is expressed in the following equations: Eq.(6.1), Eq.(6.2), and Eq.(6.3).

$$x_{R1}(t) = x(t)_0^{15} \tag{6.1}$$

$$x_D(t) = x(t)_{15}^{N-15} \tag{6.2}$$

$$x_{R2}(t) = x(t)_{N-15}^{N} \tag{6.3}$$

The equations Eq.(6.4), Eq.(6.5), and Eq.(6.6) result from taking the Hurst of each section: first rest ($R1$), drive ($D$), and last rest ($R2$); which are referred to as the HSEs in the results and discussion section. Hurst estimation using the diffusion entropy method is denoted as $H[]$.

$$H_{R1} = H[x(t)]_0^{15} \tag{6.4}$$

$$H_D = H[x(t)]_{15}^{N-15} \tag{6.5}$$

$$H_{R2} = H[x(t)]_{N-15}^{N} \tag{6.6}$$

### 6.3.2 Sliding Window

The sliding window and how it is optimized is explained in detail in Chapter 1, Section 2. The optimizing parameter ($OP$) used was the root mean squared error (RMSE) of the sliding window variable ($SWV$), which is the Hurst, for each respective combination of $w_t$ and $s_t$. The RMSE was selected as the $OP$ to minimize error between $SWV$ and the HSEs. An orthogonal view of the 3D plot with a optimized trace of $s_t$ with respect to $w_t$ for first rest, drive, and last rest using diffusion entropy is shown in in Fig. 6.1, Fig. 6.2, and Fig. 6.3. Using the trace line as a guide, the optimal $w_t$ and $s_t$ were chosen heuristically. The optimal trace line converged at appoximately $w_t = 6min$ in first rest, drive, and last rest with $s_t$ values of 6, 4, and 5 minutes; respectively. The combinatory sliding window parameters $(w_t = 6, s_t = 4), (w_t = 6, s_t = 5), and (w_t = 6, s_t = 6)$ were all taken into consideration and their sliding window data are in Appendix B. The optimal sliding window parameters $w_t = 6$ and all $s_t = 4$ were chosen because the smallest $s_t$ is desired to promote more data analysis and output.

$$RMSE = \sqrt{\frac{1}{N}\sum_{i=1}^{N}(x_i - \overline{x}_i)^2} \tag{6.7}$$

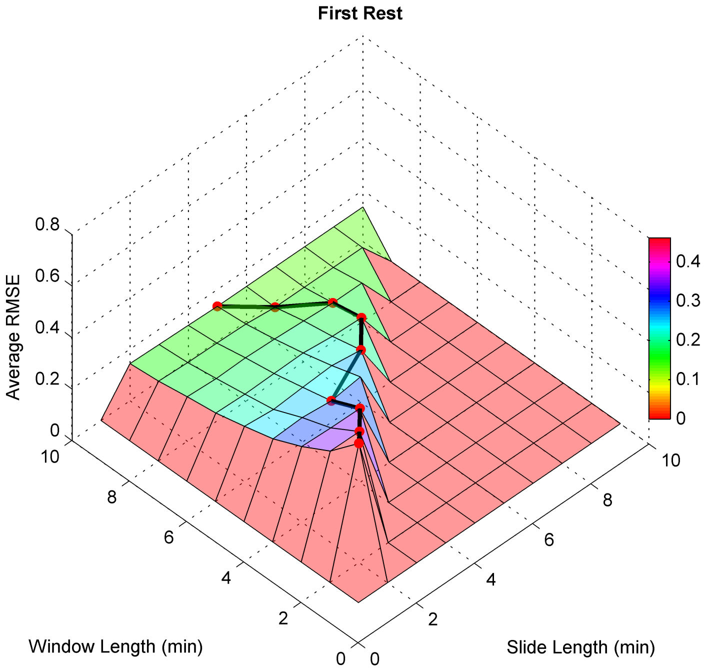

**Figure 6.1:** 3D plot of optimal trace line for first rest (R1).

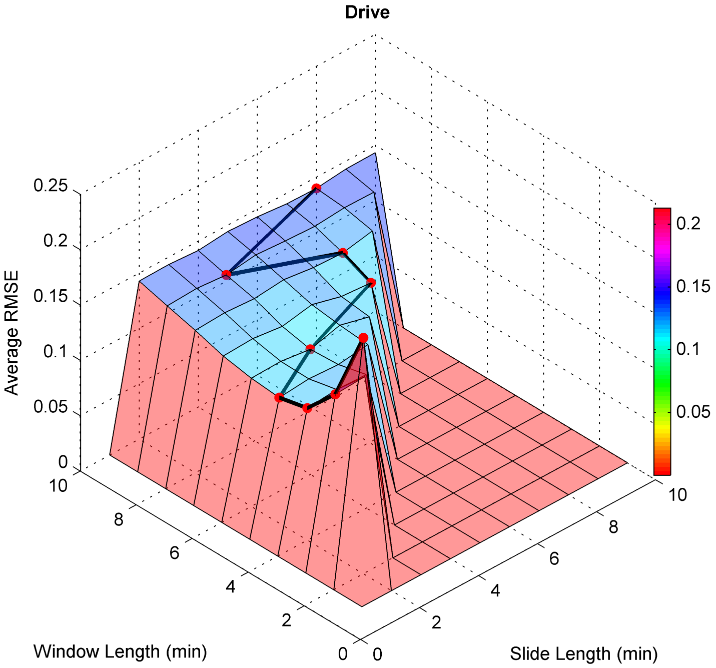

**Figure 6.2:** 3D plot of optimal trace line for drive (D).

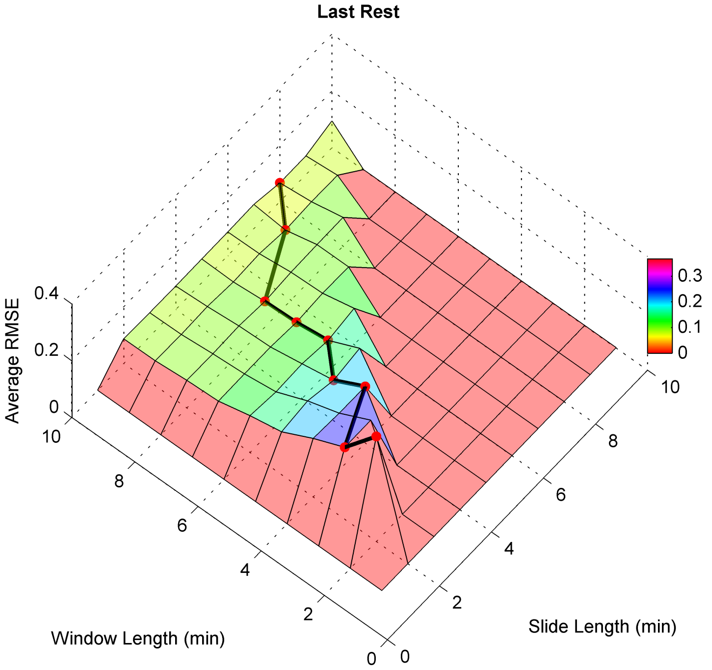

**Figure 6.3:** 3D plot of optimal trace line for last rest (R2).

## 6.4 Results & Discussion

The HSE and sliding window approaches are analyzed. The HSE data is tabulated for first rest ($R1$), drive ($D$), and last rest ($R2$) for all 13 samples. The tabulated data is presented in a graph with respect to each sample and a boxplot with respect to each section as shown in Fig. 6.5 and Fig. 6.4. As for the sliding window approach, the parameters used for the sliding window were $w_t = 6$ and $s_t = 4$. Subject #13 is the only sliding window sample displayed in Fig. 6.6; see Appendix B for all sliding window results.

### 6.4.1 Hurst Sectional Estimation Analysis

The Hurst exponent was highest during the drive section of the dataset for approximately 61% of samples, shown in Table 6.2; $H_D$ was higher than both $H_{R1}$ and $H_{R2}$. The box plot of the sectional Hurst exponents shown in Fig. 6.4 suggest that there exists a slight differentiation between rest and stress conditions. Unfortunately, the rest and stress Hurst dichotomy does not exist within this stress HRV dataset. This highlights the difficulty of indexing stress from samples. The Hurst exponent is found to be high due to the innate LRD found in physiological signals. Consequently, this makes it difficult to utilize the Hurst exponent to detect stress. Especially since mental stress does not alway manifest in a physical manner such as increased heart rate. Only three samples, had a $H_D < H_{R1}$ and $H_{R2}$. Two separate samples had a case where the Hurst exponent continuously decreased and increased such that $H_{R1} < H_D < H_{R2}$ and $H_{R1} > H_D > H_{R2}$, respectively.

**Table 6.2:** Hurst Sectional Estimation

| **Driver #** | $H_{R1}$ | $H_D$ | $H_{R2}$ |
|---|---|---|---|
| **1** | 0.99 | 0.88 | 0.77 |
| **2** | 0.77 | 0.92 | 0.84 |
| **3** | 0.76 | 0.82 | 0.61 |
| **4** | 0.86 | 0.98 | 0.83 |
| **5** | 0.88 | 1.03 | 0.96 |
| **6** | 0.96 | 1.11 | 0.95 |
| **7** | 1.06 | 0.97 | 0.99 |
| **8** | 0.92 | 1.02 | 0.80 |
| **9** | 1.01 | 0.88 | 0.91 |
| **10** | 0.88 | 0.86 | 0.88 |
| **11** | 0.89 | 0.95 | 0.92 |
| **12** | 0.76 | 0.89 | 0.96 |
| **13** | 0.94 | 1.14 | 0.65 |

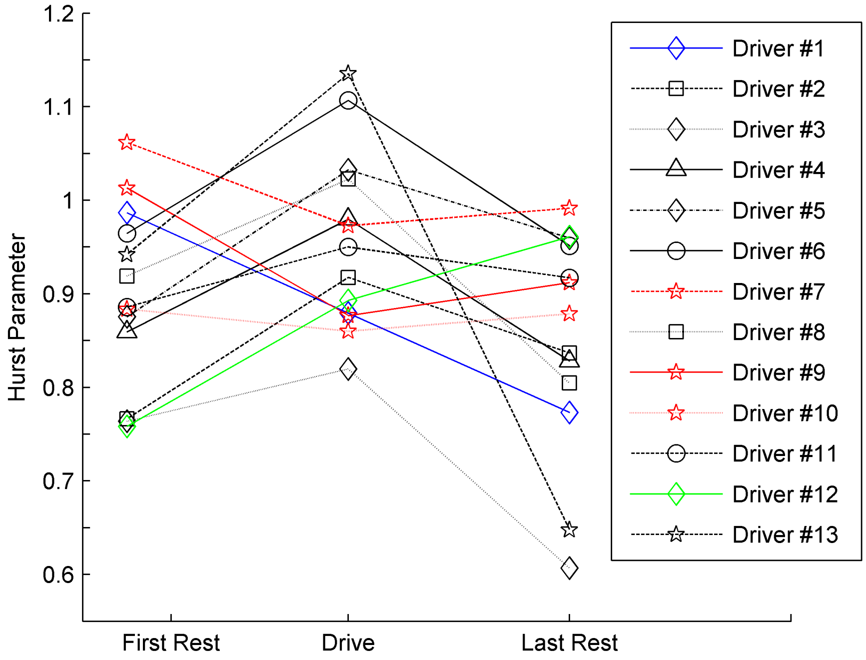

**Figure 6.4:** Hurst sectional estimation plot.

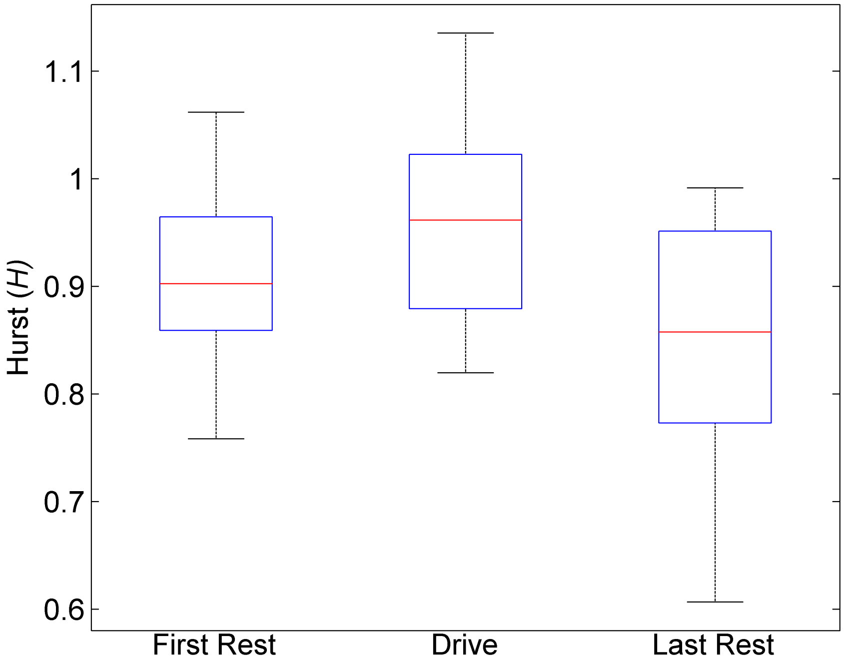

**Figure 6.5:** Hurst sectional estimation boxplot.

### 6.4.2 Sliding Window Analysis

The optimized parameters used for the sliding window were $w_t = 6$ and all $s_t = 4$. Two observations were utilized in analyzing the sliding window results. One of the observations was the proximity of slide values compared to their sectional values. Heuristically, it was seen that in approximately half the data the slide values were relatively close to sectional values. The other observation was slide morphology over all three sections. More often than not, it was seen that the drive section contained more stochastic characteristics compared to the rest sections. See Fig. 6.6 for sliding window result from one subject.

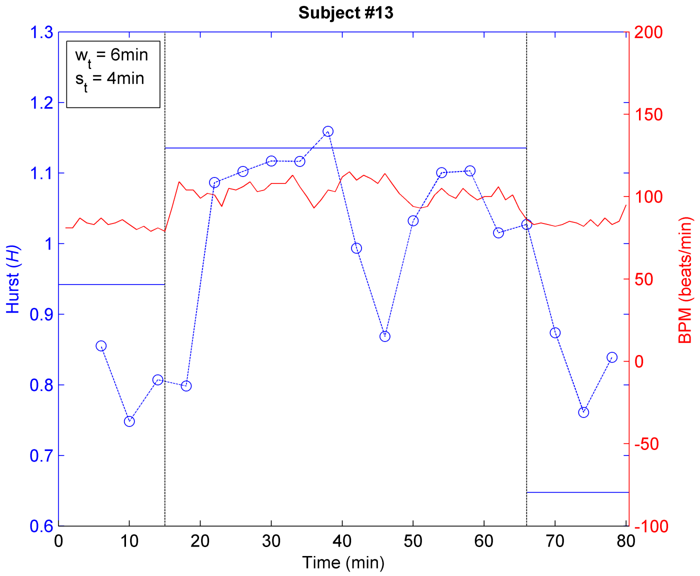

**Figure 6.6:** Sample of sliding window displayed as blue dots. The HSEs are shown as blue horizontal bars.

## 6.5 Conclusion

HRV has been examined in both rest and mental stress states. The rest HSEs were generally lower than stress HSE, approximately 61% of the time. The HSE is potentially a practical algorithmic framework with the assumption that the user would complete a diagnostic survey so that the heart monitoring sensors can record resting HRV and stress HRV. However, the potential of the sliding window algorithmic framework is questionable due to the large combinatory amount of window and slide lengths. The findings of this paper suggest that $w_t =$ and $s_t = 4$ may potentially be the optimal window and slide length parameters. Ultimately, more samples will be required to assess the quality of the sliding window algorithmic framework and to properly determine optimal window and slide length.

# Chapter 7

# SUMMARY & FUTURE RESEARCH

The characterization of long range dependence (LRD) for signal processing is the recurring theme in this thesis. The notion and mathematical significance of LRD is highlighted in Chapter 3. Hurst estimators were utilized to identify LRD, classify arrhythmia, and detect stress in Chapter 4, 5, and 6, respectively. A brief summary and future research direction are given below for the research project based Chapters 4, 5, and 6.

Research presented in Chapter 4 established the strong presence of LRD in thermal infrared (TIR) imaging. Steady state analysis clearly showed a Hurst bias running along pixel index X which suggests that specific regions of the image should be filter differently that the rest of the pixels. Ultimately, the statistical features of LRD in each pixel may be exploited to potentially filter out temporal noise in TIR images and well as calibrational purposes. Utilizing LRD found in pixels, further investigation could be done to monitor individual pixel health or detect dead pixels.

Research presented in Chapter 5 strongly suggests that the quantification of LRD presence in heart rate variability (HRV) via Hurst exponent estimation can be utilized for cardiac arrhythmia detection. Samples with normal HRV typically displayed higher Hurst exponent values since LRD is an innate characteristic of physiological signals. On the other hand, samples with arrhythmias generally exhibited smaller Hurst exponents. Results show that most methods are able to differentiate between normal and arrhythmic HRV with the exception of the difference variance method. Potentially the Hurst exponent can be used as an arrhythmia classification index for extreme cases of cardiac arrhythmia. One possible future research direction of this project is to engineer a device that can process HRV data and calculate one's Hurst exponent for cardiac health monitoring. A simple control diagram of a Hurst health monitoring device is shown in Fig. 7.1 . The input for this device is a person's cardiac output. Also, the sensor was left ambiguous since it could be as complex as an electrocardiogram or as simple as optical monitoring which uses a light emitting diode (LED). I envision the end goal of this project assisting physicians monitor elderly patients heart health via telemedicine, where the Hurst exponent is utilized as a classification index of heart health.

An attempt at mental stress detection using LRD characterization is presented in Chapter 6. However, physiological signals such as HRV naturally have a strong LRD presence. As a result, distinction between mental stress and rest HRV in terms of Hurst exponent were not completely clear. More mental stress HRV data would be required to determine whether LRD characterization can be utilized in stress detection or not. Perhaps, the sliding window is not the proper algorithmic framework to use. More samples are required in order to determine any research significant on this project. The online database used, physioNet, only offered 17 samples of which only 13 were utilized in the end due to complications in preliminary HRV signal processing, poor ECG readings, and an omitted duplicate sample. A suggestion for further research on this topic would be to obtain more samples under mental stress conditions. If possible, my personal suggestion would be to collect 20-30 HRV samples from samples who experience a rest condition and transition into performing a difficult mental task such as navigating an unmanned aerial vehicle (UAV) through a mission.

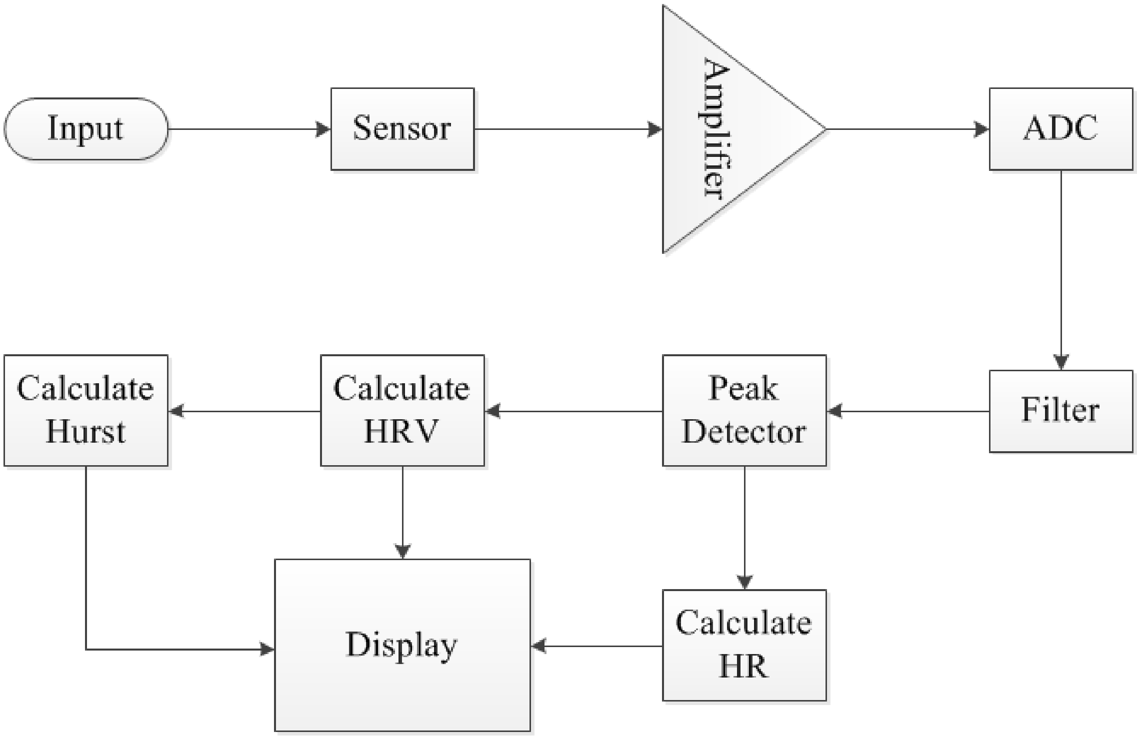

**Figure 7.1:** Control diagram of Hurst cardiac health monitoring system.

# BIBLIOGRAPHY

[1] G. W. Leibniz, Mathematische Schiften, Vol. 4, Berlin A. Asher, 1863.

[2] T. E. Duncan, Y. Hu, B. Pasik-Duncan, Stochastic calculus for fractional brownian motion i. theory, TSIAM Journal on Control and Optimization 38 (2) (2000) 582–612.

[3] H. Qian, Fractional brownian motion and fractional gaussian noise, in: G. Rangarajan, M. Ding (Eds.), Processes with Long-Range Correlations, Vol. 621 of Lecture Notes in Physics, Springer, 2003, pp. 22–33.

[4] H. Sheng, Y. Chen, T. Qiu, Fractional Processes and Fractional-Order Signal Processing: Techniques and Applications, Springer, 2012.

[5] C. Chen, Hurst parameter estimate, MATLAB Central, www.mathworks.com/matlabcentral/fileexchange/19148-hurst-parameter-estimate (2008).

[6] M. Gonzalez, J. Castro, M. Fernandez-Chimeno, A novel index based on fractional calculus to assess the dynamics of heart rate variability: Changes due to chi or yoga meditations, in: Computing in Cardiology (CinC), 2012, 2012, pp. 925–928.

[7] O. Barquero-Perez, J. de Sa, J. Rojo-Alvarez, R. Goya-Esteban, Changes in detrended fluctuation indices with aging in healthy and congestive heart failure subjects, in: Computers in Cardiology, 2008, 2008, pp. 45–48.

[8] Unknown, Discovery of Infrared Light, National Aeronautics and Space Administration (NASA), manual: Herschel Infrared Experiment.

[9] Unknown, Basic Principles Of Non-Contact Temperature Measurement, Optris, manual: Innovative Infrared Technology.

[10] W. Swiderski, V. Vavilov, Ir thermographic detection of defects in multi-layered composite materials used in military applications, in: Infrared and Millimeter Waves, 2007 and the 2007 15th International Conference on Terahertz Electronics. IRMMW-THz. Joint 32nd International Conference on, 2007, pp. 553–556.

[11] J. Teich, Digital infrared imaging for medicine. recent advances in i.r. focal plane array imaging technology, in: Engineering in Medicine and Biology Society, 1996. Bridging Disciplines for Biomedicine. Proceedings of the 18th Annual International Conference of the IEEE, Vol. 5, 1996, pp. 2079–2080.

[12] B. Stark, M. McGee, Y. Chen, Short wave infrared (swir) imaging systems using small unmanned aerial systems (suas), in: Unmanned Aircraft Systems (ICUAS), 2015 International Conference on, 2015, pp. 495–501.

[13] B. Wiecek, Review on thermal image processing for passive and active thermography, in: Engineering in Medicine and Biology Society, 2005. IEEE-EMBS 2005. 27th Annual International Conference of the, 2005, pp. 686–689.

[14] D. A. Scribner, M. Kruer, J. M. Killiany, Infrared focal plane array technology, Proceedings of the IEEE 79 (1) (1991) 66–85.

[15] J. M. Berg, J. L. Tymoczko, L. Stryer, Biochemistry, 6th Edition, W.H. Freeman, 2007.

[16] W. F. Boron, E. L. Boulpaep, Medical Physiology, 2nd Edition, Saunders Elsevier, 2012.

[17] G. D. Clifford, F. Azuaje, P. E. McSharry, Advanced Methods and Tools for ECG Data Analysis, Artech House, 2006.

[18] B. B. Mandelbrot, The fractal geometry of nature, 1st Edition, W.H. Freeman, 1982.

[19] K. Falconer, Fractal Geometry: Mathematical Foundations and Applications, 3rd Edition, Wiley, 2014.

[20] P. Doukhan, G. Oppenheim, M. S. Taqqu, Theory and Applications of Long-Range Dependence, Birkhäuser, 2003.

[21] T. Gneiting, M. Schlather, Stochastic models that separate fractal dimension and the hurst effect, SIAM Review 46 (2) (2004) 269–282.

[22] O. Barquero-Perez, Heart rate variability: A fractal analysis, Master's thesis, Universidade do Porto, masters Thesis (6 2008).

[23] H. Schepers, J. van Beek, J. Bassingthwaighte, Four methods to estimate the fractal dimension from self-affine signals (medical application), Engineering in Medicine and Biology Magazine, IEEE 11 (2) (1992) 57–64.

[24] M. S. Taqqu, V. Teverovsky, W. Willinger, Estimators for long-range dependence: An emperical study, Fractals 3 (4) (1995) 785–788.

[25] M. S. Granero, J. T. Segovia, J. G. Prez, Some comments on hurst exponent and the long memory processes on capital markets, Physica A: Statistical Mechanics and its Applications 387 (22) (2008) 5543–5551.

[26] B. J. West, Fractal Physiology and Chaos in Medicine, 2nd Edition, World Scientific, 2013.

[27] R. Costin, C. Rotariu, A. Pasarica, A practical guide to measuring the hurst parameter, in: International Journal of Simulation: Systems, Science & Technology, Vol. 7, 2006, pp. 3–14.

[28] J. Beran, Y. Feng, S. Ghosh, R. Kulik, Long-Memory Processes: Probabilistic Properties and Statistical Methods, Springer, 2013.

[29] R. Schilling, L. Partzsch, Brownian Motion: An Introduction to Stochastic Processes, De Gruyter, 2014.

[30] H. Sheng, Y. Chen, T. Qiu, On the robustness of hurst estimators, Signal Processing, IET 5 (2) (2011) 209–225.

[31] H. Sheng, Y. Chen, T. Qiu, Tracking performance and robustness analysis of hurst estimators for multifractional processes, Signal Processing, IET 6 (3) (2012) 213–226.

[32] B. Guo-ping, Y. Yi-rong, Hurst exponent estimation based on modified aggregated variance method, in: Service Operations and Logistics, and Informatics, 2006. SOLI '06. IEEE International Conference on, 2006, pp. 51–56.

[33] J. Qi, H. Yang, Hurst exponents for short time series, Physical Review E, APS 84 (6).

[34] S. Katsev, I. LHeureux, Are hurst exponents estimated from short or irregular time series meaningful?, Computers & Geosciences 29 (9) (2003) 1085–1089.

[35] H. E. Hurst, R. P. Black, Long-Term Storage. An Experimental Study., Constable, 1965.

[36] C. Nitschke, A. Nakazawa, H. Takemura, Eye reflection analysis and application to display-camera calibration, in: Image Processing (ICIP), 2009 16th IEEE International Conference on, 2009, pp. 3449–3452.

[37] R. Redlich, M. Figueroa, S. N. Torres, J. E. Pezoa, Embedded nonuniformity correction in infrared focal plane arrays using the constant range algorithm, Infrared Physics & Technology 69 (2015) 164–173.

[38] T. Kelly, Non-uniformity correction and calibration of a portable infrared scene projector, in: AUTOTESTCON Proceedings, 2002. IEEE, 2002, pp. 107–115.

[39] Y. Liu, H. Zhu, Y. Zhao, New scene-based nonuniformity correction algorithm of infrared focal-plane arrays, in: Image and Signal Processing and Analysis, 2007. ISPA 2007. 5th International Symposium on, 2007, pp. 274–277.

[40] E. Giard, B.-L. Nghiem, M. Caes, M. Tauvy, I. Ribet-Mohamed, R. Taalat, M. Delmas, J. Rodriguez, P. Christol, Noise measurements for the performance analysis of infrared photodetectors, in: Noise and Fluctuations (ICNF), 2013 22nd International Conference on, 2013, pp. 1–4.

[41] C. Liu, W. Jin, Y. Chen, B. Liu, Y. Cao, X. Liu, A self-adaptive nonuniformity correction algorithm for infrared images combined with two-point correction along the rim, in: Computer Symposium (ICS), 2010 International, 2010, pp. 240–245.

[42] A. K. Mishra, S. Raghav, Local fractal dimension based ecg arrhythmia classification, Biomedical Signal Processing and Control 5 (2) (2010) 114–123.

[43] M. Cusenza, A. Accardo, G. D'Addio, G. Corbi, Relationship between fractal dimension and power-law exponent of heart rate variability in normal and heart failure subjects, in: Computing in Cardiology, 2010, 2010, pp. 935–938.

[44] X. Ye, X. Xia, J. Zhang, Y. Chen, Effects of trends and seasonalities on robustness of the hurst parameter estimators, Signal Processing, IET 6 (9) (2012) 849–856.

[45] A. Leite, A. Rocha, M. Silva, S. Gouveia, J. Carvalho, O. Costa, Long-range dependence in heart rate variability data: Arfima modelling vs detrended fluctuation analysis, in: Computers in Cardiology, 2007, 2007, pp. 21–24.

[46] J.-C. Cano, P. Manzoni, On the use and calculation of the hurst parameter with mpeg videos data traffic, in: Euromicro Conference, 2000. Proceedings of the 26th, Vol. 1, 2000, pp. 448–455.

[47] B. J. West, Fractal physiology and the fractional calculus: A perspective, Frontiers in Physiology 1 (12).

[48] B. West, R. Zhang, A. Sanders, S. Miniyar, J. Zuckerman, B. Levine, Fractal fluctuations in cardiac time series, Physica A: Statistical Mechanics and its Applications 270 (3-4) (1999) 552–566.

[49] G. B. Moody, R. G. Mark, A. L. Goldberger, Physionet: Physiologic signals, time series and related open source software for basic, clinical, and applied research, in: Engineering in Medicine and Biology Society, EMBC, 2011 Annual International Conference of the IEEE, 2011, pp. 8327–8330.

[50] C. Cammarota, Time series analysis of data from stress ecg, in: Communications to SIMAI Congress, Vol. 3, 2009.

[51] R. Costin, C. Rotariu, A. Pasarica, Mental stress detection using heart rate variability and morphologic variability of eeg signals, in: Electrical and Power Engineering (EPE), 2012 International Conference and Exposition on, 2012, pp. 591–596.

[52] J. Taelman, S. Vandeput, A. Spaepen, S. V. Huffel, Influence of mental stress on heart rate and heart rate variability, in: 4th European Conference of the International Federation for Medical and Biological Engineering, Vol. 22, 2009, pp. 1366–1369.

[53] F.-T. Sun, C. Kuo, H.-T. Cheng, S. Buthpitiya, P. Collins, M. Griss, Activity-aware mental stress detection using physiological sensors, in: M. Gris, G. Yang (Eds.), Mobile Computing, Applications, and Services, Vol. 76 of Lecture Notes of the Institute for Computer Sciences, Social Informatics and Telecommunications Engineering, Springer, 2010, pp. 211–230.

[54] R. Singh, S. Conjeti, R. Banerjee, An approach for real-time stress-trend detection using physiological signals in wearable computing systems for automotive drivers, in: Intelligent Transportation Systems (ITSC), 2011 14th International IEEE Conference on, 2011, pp. 1477–1482.

[55] A. R. Subahni, L. Xia, A. S. Malik, Association of mental stress with video games, in: Intelligent and Advanced Systems (ICIAS), 2012 4th International Conference on, Vol. 1, 2012, pp. 82–85.

[56] R. R. Singh, S. Conjeti, R. Banerjee, Biosignal based on-road stress monitoring for automotive drivers, in: Communications (NCC), 2012 National Conference on, 2012, pp. 1–5.

[57] P. Karthikeyan, M. Murugappan, S. Yaacob, Ecg signals based mental stress assessment using wavelet transform, in: Control System, Computing and Engineering (ICCSCE), 2011 IEEE International Conference on, 2011, pp. 258–262.

[58] J. Taelman, S. Vandeput, I. Gligorijevic, A. Spaepen, S. V. Huffel, Time-frequency heart rate variability characteristics of young adults during physical, mental and combined stress in laboratory environment, in: Engineering in

Medicine and Biology Society, EMBC, 2011 Annual International Conference of the IEEE, 2011, pp. 1973–1976.

[59] J. Healey, R. Picard, Detecting stress during real-world driving tasks using physiological sensors, Intelligent Transportation Systems, IEEE Transactions on 6 (2) (2005) 156–166.

[60] R. L. Magin, Fractional calculus models of complex dynamics in biological tissues, Computers & Mathematics with Applications 59 (5) (2010) 1586–1593.

[61] R. L. Magin, M. Ovadia, Modeling the cardiac tissue electrode interface using fractional calculus, Journal of Vibration and Control 14 (9-10) (2008) 1431–1442.

[62] A. Eke, P. Hermán, L. Kocsis, L. Kozak, Fractal characterization of complexity in temporal physiological signals, Physiological Measurement 23 (1) (2002) 1–37.

[63] M. A. Garca-Gonzlez, M. Fernndez-Chimeno, L. Capdevila, E. Parrado, J. Ramos-Castro, An application of fractional differintegration to heart rate variability time series, Computer Methods and Programs in Biomedicine 111 (1) (2013) 33–40.

[64] H. Sedghamiz, Ecg qrs wave online dector, MATLAB Central, mathworks.com/matlabcentral/fileexchange/45404-ecg-q-r-s-wave-online-detector (2014).

# Appendix A

# PROTOCOLS

## A.1 Thermal Imaging Protocol

1. Setup Equipment
   - Place camera on stand such that lense is parallel to ground.
   - Place reflectance reference target underneath camera such that only the reflectance reference target is seen by the camera.
   - Double check camera view via camera monitor to ensure that only reflectance reference target is being viewed.
   - Place thermal couples on each opposite ends of the reflectance reference target material
   - Double check room thermostat to make sure temperature is set at $74^oC$. If not, set temperature to $74^oC$ and wait until room acclimates; then proceed.
2. Collect Images
   - Camera runs at a sample rate of 0.5Hz and takes pictures for approximately two hours. Only the first hour of data is utilized for data analysis.
3. Upload & Process Images.
   - Upload images to computer.
   - Use software called IR Flash, provided by ICI, to convert images to comma separated values (CSV) files.
4. Process Images
   - Create Hurst map using diffusion entropy analysis from every 20 pixel for each image sample; 825 pixels were analyzed per image sample.
   - See appendix C for MATLAB code to process TIR data into Hurst and Variance Maps.

## A.2 PhysioNet Protocol

This is a protocol for downloading and processing data from physioNet for specifically electrocardiogram (ECG) derived heart rate variability time series [49].

### PhysioBank: Data Selection

Find physiological data that you are interested in. An archive of physiological databases, physioBank, is available at www.physionet.org/physiobank/database/.

### PhysioToolkit: MATLAB Toolbox

Go to http://www.physionet.org/physiotools/matlab/wfdb-app-matlab/ and it will show you how to download the physioNet toolbox for MATLAB. See below for a quick procedure to download toolbox.

1. Go into folder or directory you wish to install toolbox
2. Copy and pase the following code into the command window:

```
[old_path]=which('rdsamp');
if(¬isempty(old_path)) rmpath(old_path(1:end-8)); end
wfdb_url='http://physionet.org/physiotools/matlab/ ...
    wfdb-app-matlab/wfdb-app-toolbox-0-9-9.zip';
[filestr,status] = ...
    urlwrite(wfdb_url,'wfdb-app-toolbox-0-9-9.zip');
unzip('wfdb-app-toolbox-0-9-9.zip');
cd wfdb-app-toolbox-0-9-9;cd mcode
addpath(pwd);savepath
```

3. There should now be folder labeled as "wfdb-app-toolbox-0-9-9" with a subfolder labeled "mcode". Go into the subfolder "mcode" click on "rdsamp.m". Inside "rdsamp.m" there are instructions on how to read samples from all databases found in physioBank. This is where you can read and save the data of interest.
4. A file called "rdann.m" should be utilized to further process the data by extracting annotation data; see inside "rdann.m" for instructions for usage. This is where the beat annotations can be acquired.

### MATLAB: Signal Processing HRV from ECG

Once the beat annotations are obtained. You can utilize the MATLAB function "diff(X)" where X is the beat annotations for one sample. This will take the differences between adjacent elements of X resulting in the time interval between each beat also known as heart rate variability (HRV).

## A.3 Electrocardiogram derived Heart Rate Variability

This is a protocol for deriving heart rate variability (HRV) from electrocardiogram (ECG) given by PhysioNet [49] using an online MATLAB QRS dector [64]: mathworks.com/matlabcentral/fileexchange/45404-ecg-q-r-s-wave-online-detector.

### Obtain ECG from PhysioNet

Download ECG data from PhysioNet as mentioned in Appendix B, Section A.2. You can also download from other websites or run your own experiments to obtain ECG data. High quality ECG data will help drastically reduce time in the ensuing steps. Avoid low quality ECG data.

### Save R-peaks using QRS Dector

The example code below converts EKG data [64], with a sample rate of 496 Hz, into R-peak time index data and saves it as an excel sheet. In addition, a graph of the processed and annotated EKG is saved.

```
load(data)                          % contains EKG data
EKGDouble = double(EKG);            % converts EKG data
SampleRate = 496;                   % sample rate: 496 Hz
ViewableTime = length(EKGDouble)/SampleRate;
[R_i,R_amp] = peakdetect(EKGDouble,SampleRate,ViewableTime);
R_Peak_Time = (R_i./SampleRate)';   % sample index --> time index
savefig('Processed_EKG_graph.fig');
filename = ['Drive_R_Peak_Time.xls'];
xlswrite(filename, R_Peak_Time);
```

### Review & Edit R-peaks

First, review the ECG section found in Chapter 2, Section 2.2.5 to understand the generalized ECG morphology. Afterwards, you can begin to evaluate the accuracy of the data once you have your excel sheet of R-peaks, with respect to time in seconds. This is done by simultaneously checking data from the excel sheet visually and the R-peaks from the graph by using the ”data cursor”. If the R-peaks are annotated incorrectly on the graphs, you will manually correct them to the best of your knowledge.

### Heart Rate Variability

Once the R-peaks are reviewed and finlized, utilize the MATLAB function ”diff(X)” where X is the beat annotations for one sample. This will take the differences between adjacent elements of X resulting in the time interval between each beat also known as heart rate variability (HRV).

# Appendix B

# DATA

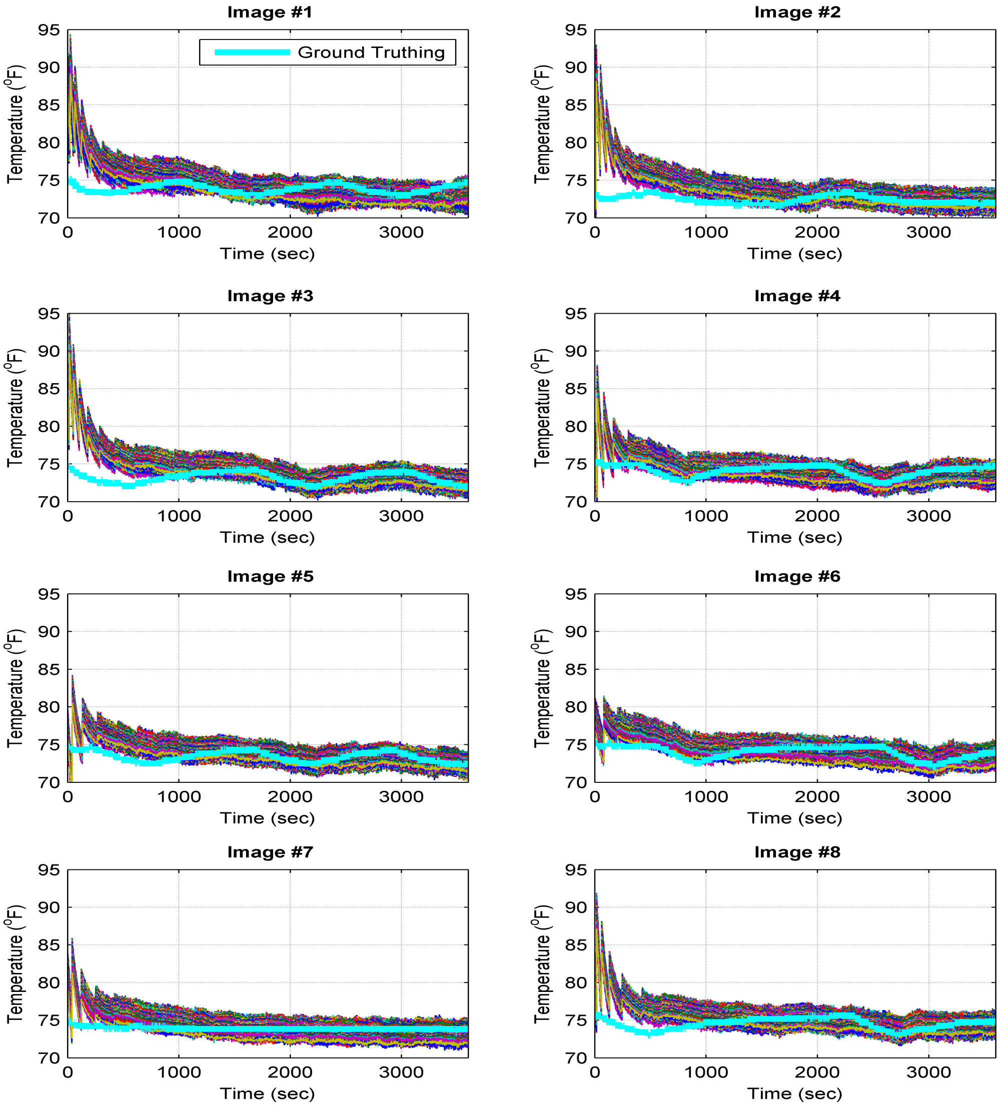

**Figure B.1:** TIR - Raw Pixel Data

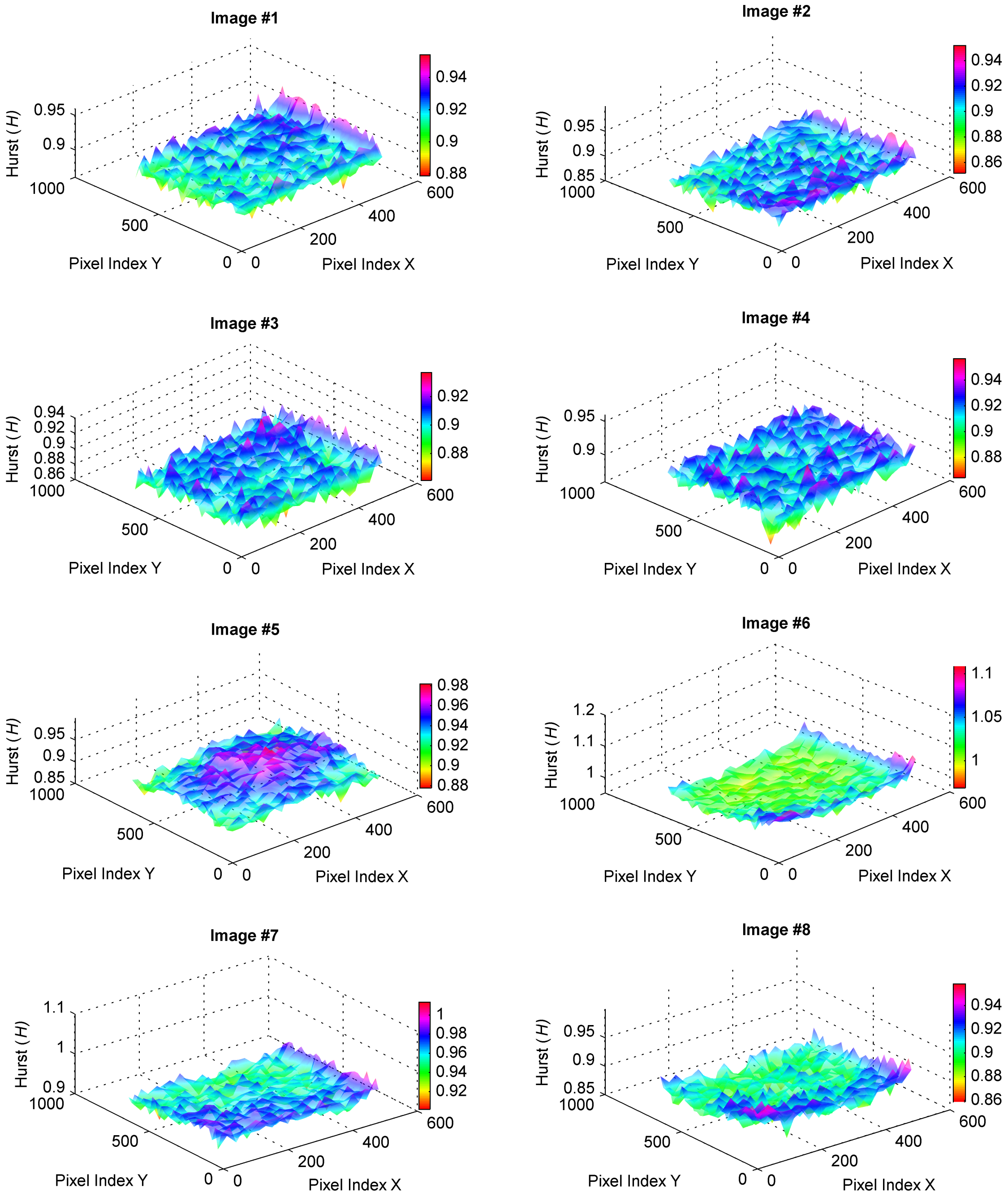

Image #1

Image #2

Image #3

Image #4

Image #5

Image #6

Image #7

Image #8

**Figure B.2:** TIR - Hurst Maps - Total Data

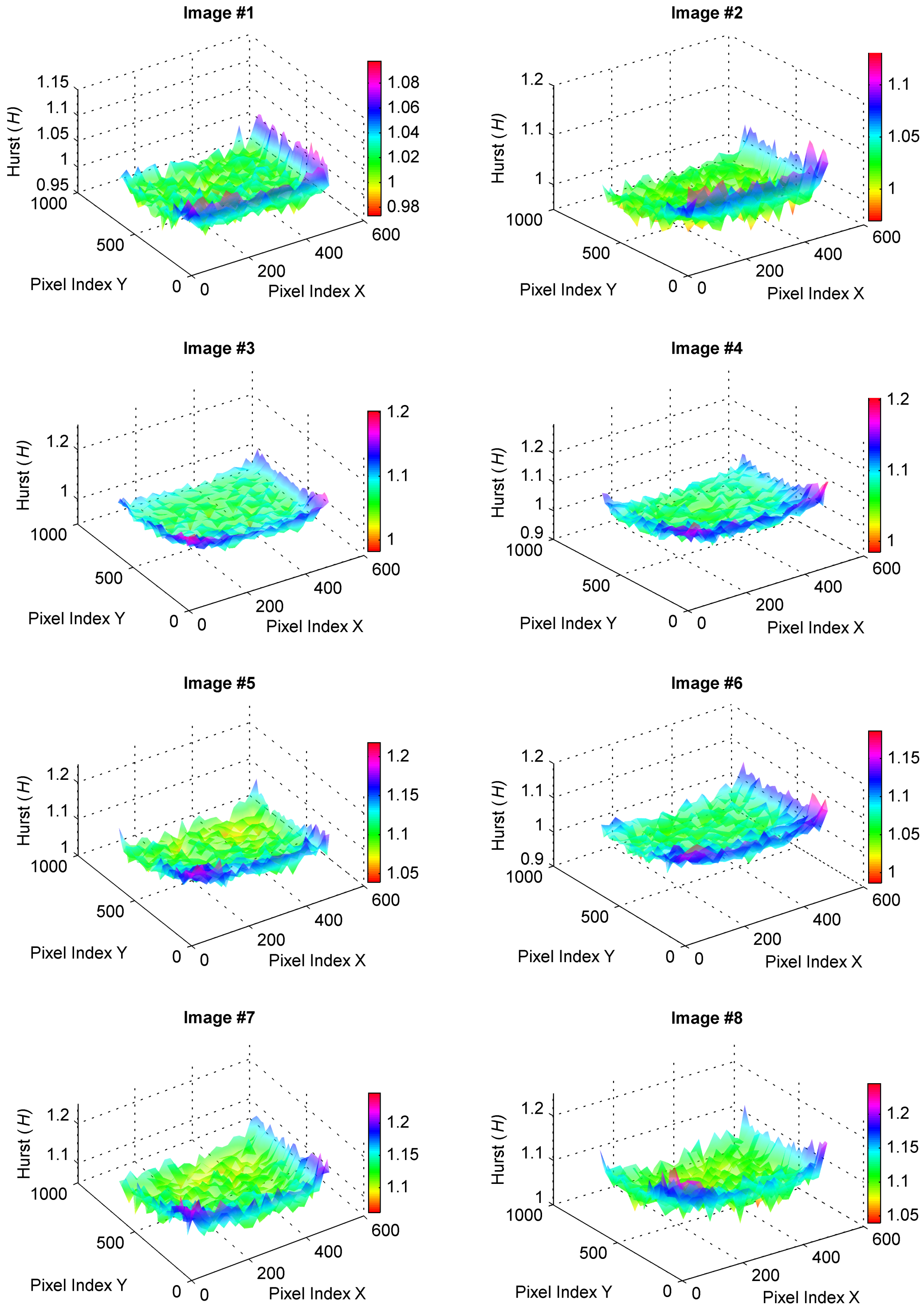

**Figure B.3:** TIR - Hurst Maps - Steady State Data

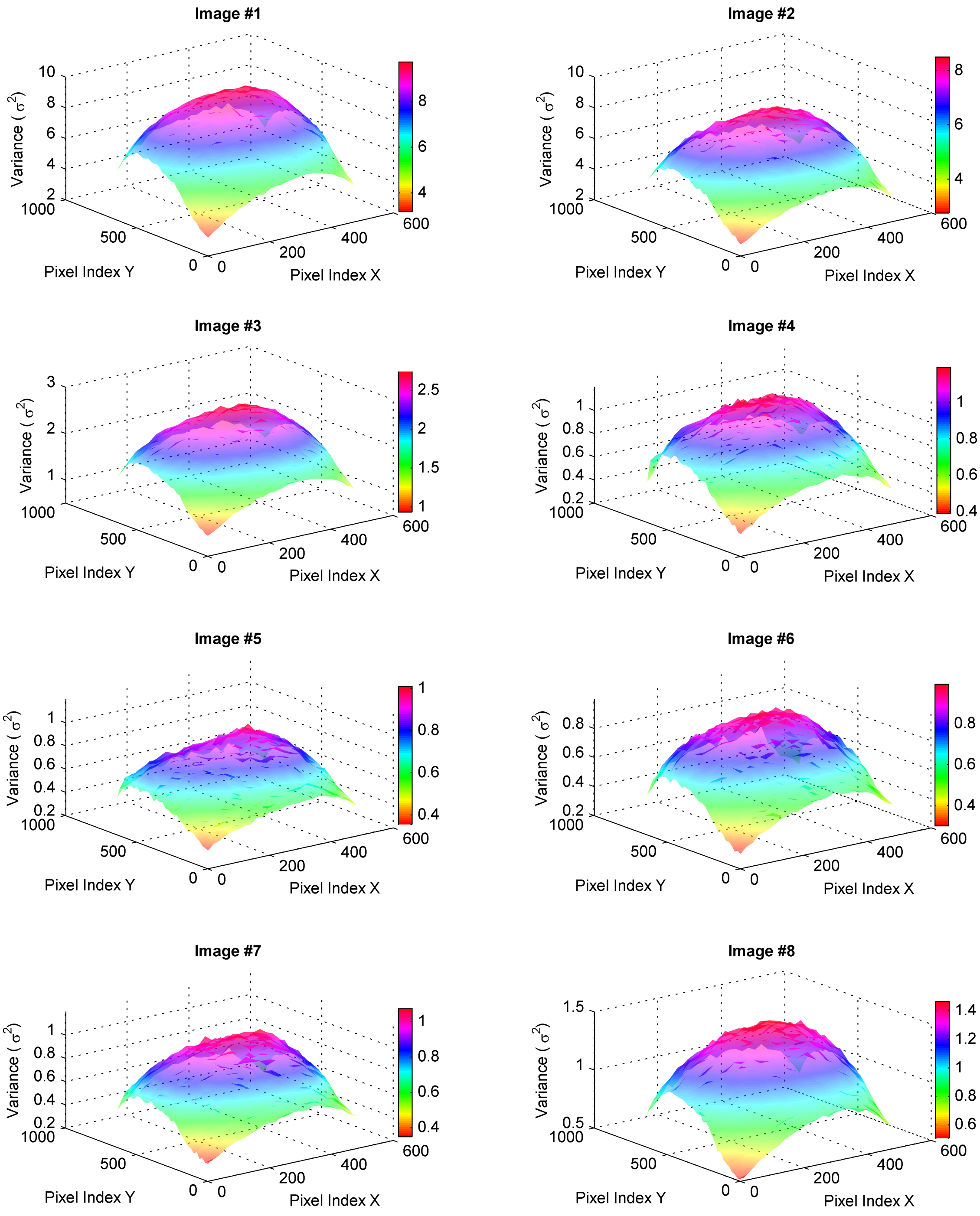

**Figure B.4:** TIR - Variance Maps - Total Data

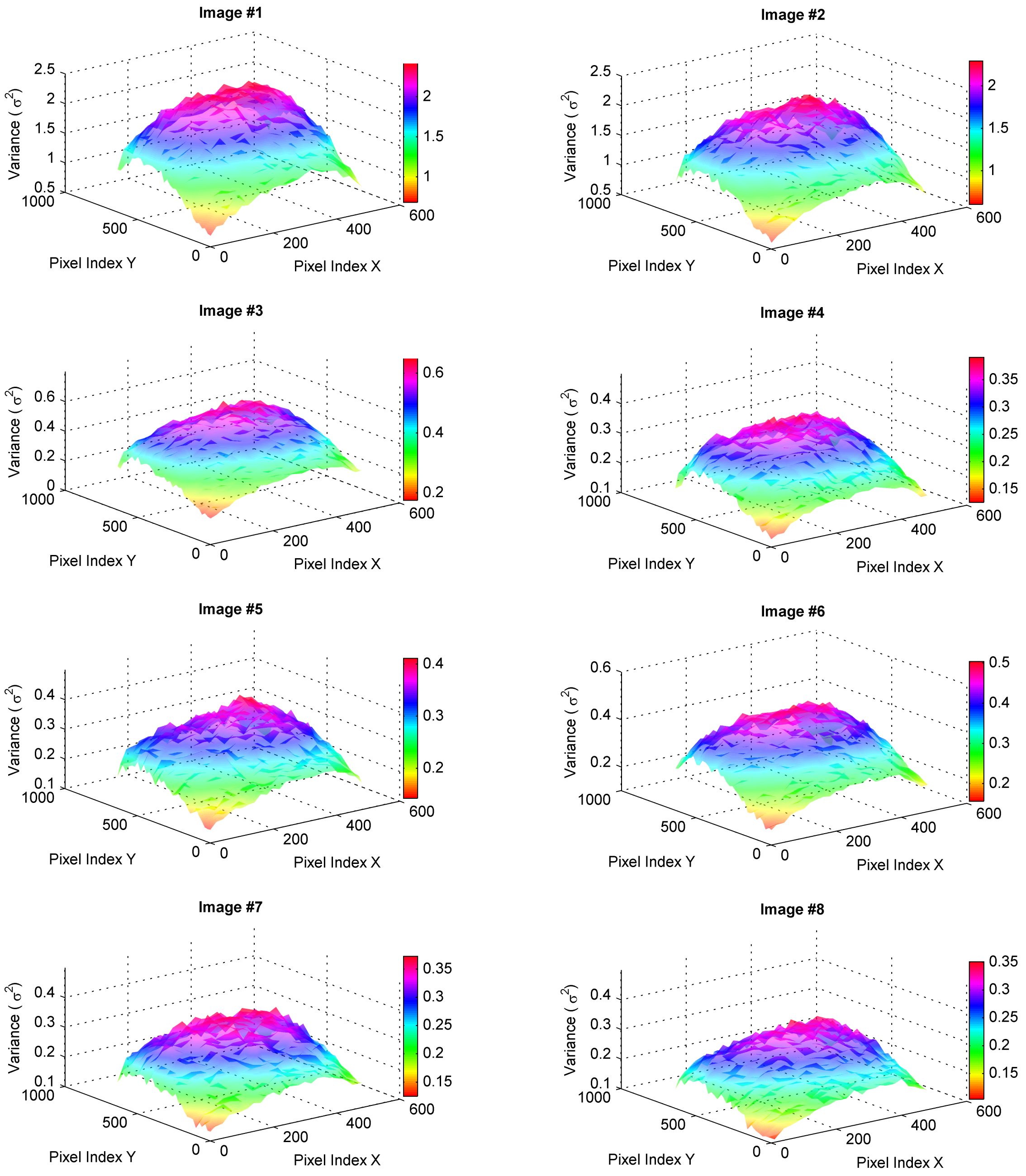

**Figure B.5:** TIR - Variance Maps - Steady State Data

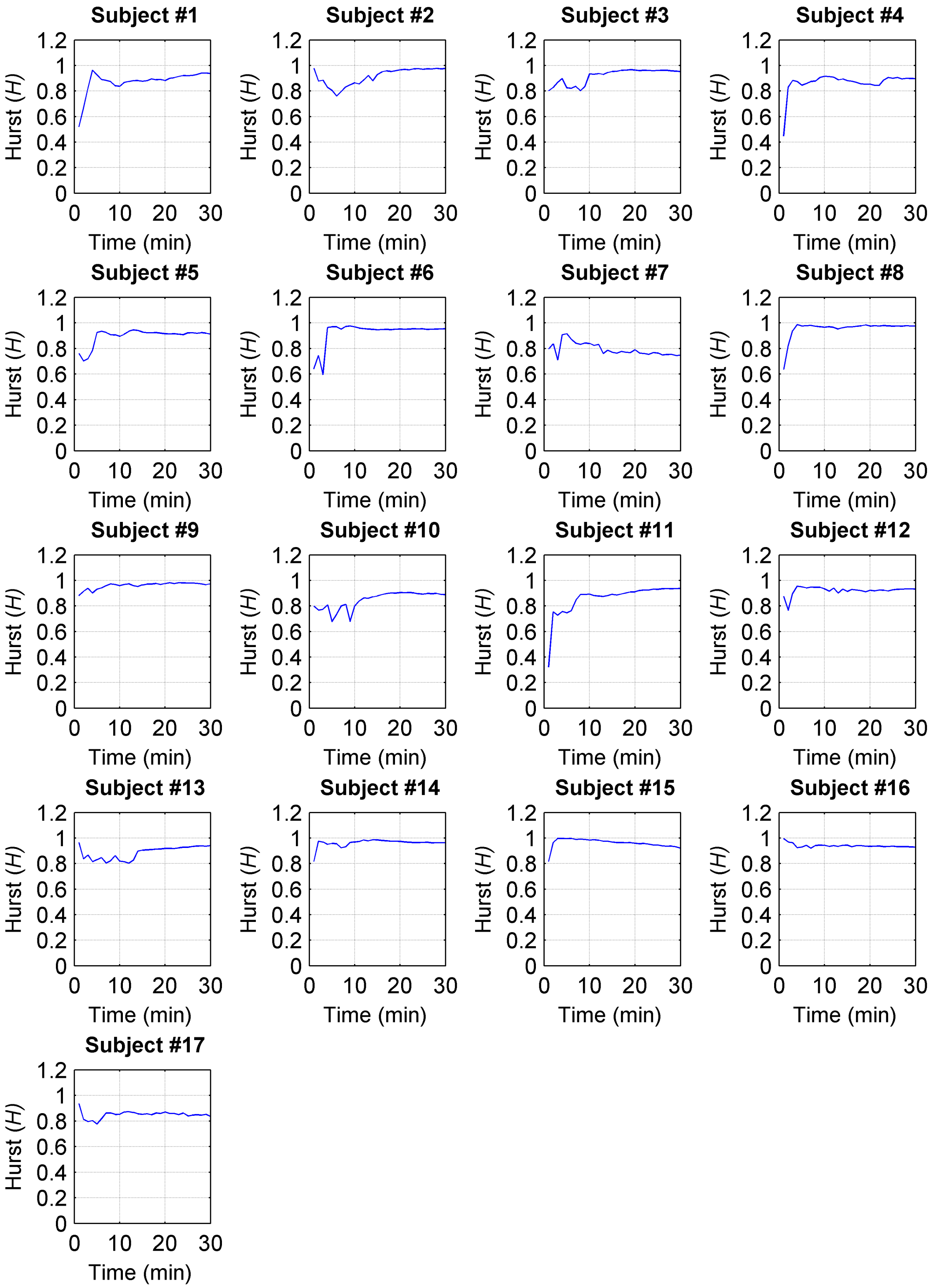

**Figure B.6:** Cardiac Index - CWE - Aggregated Variance - Normal HRV

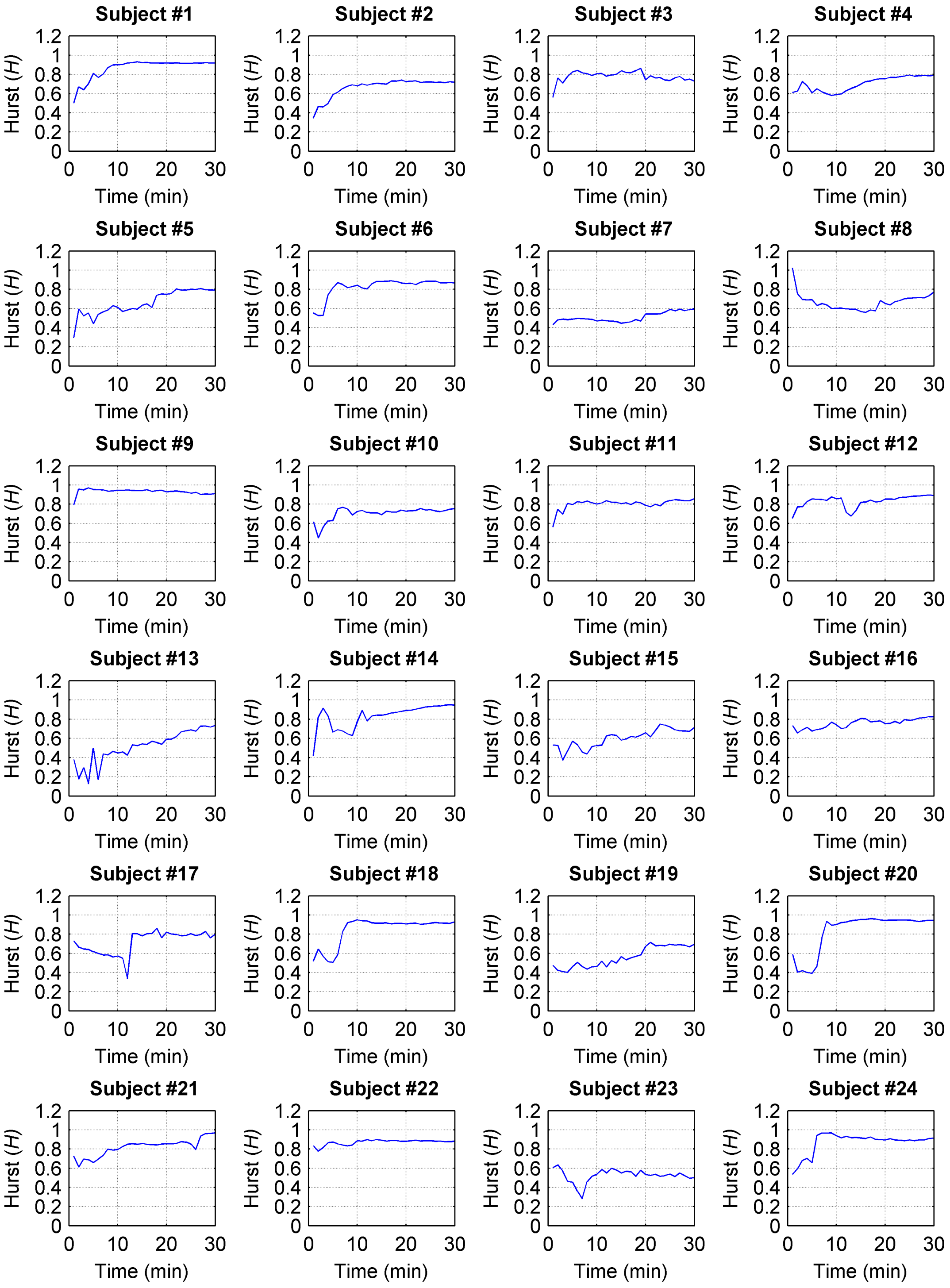

**Figure B.7:** Cardiac Index - CWE - Aggregated Variance - Abnormal HRV I

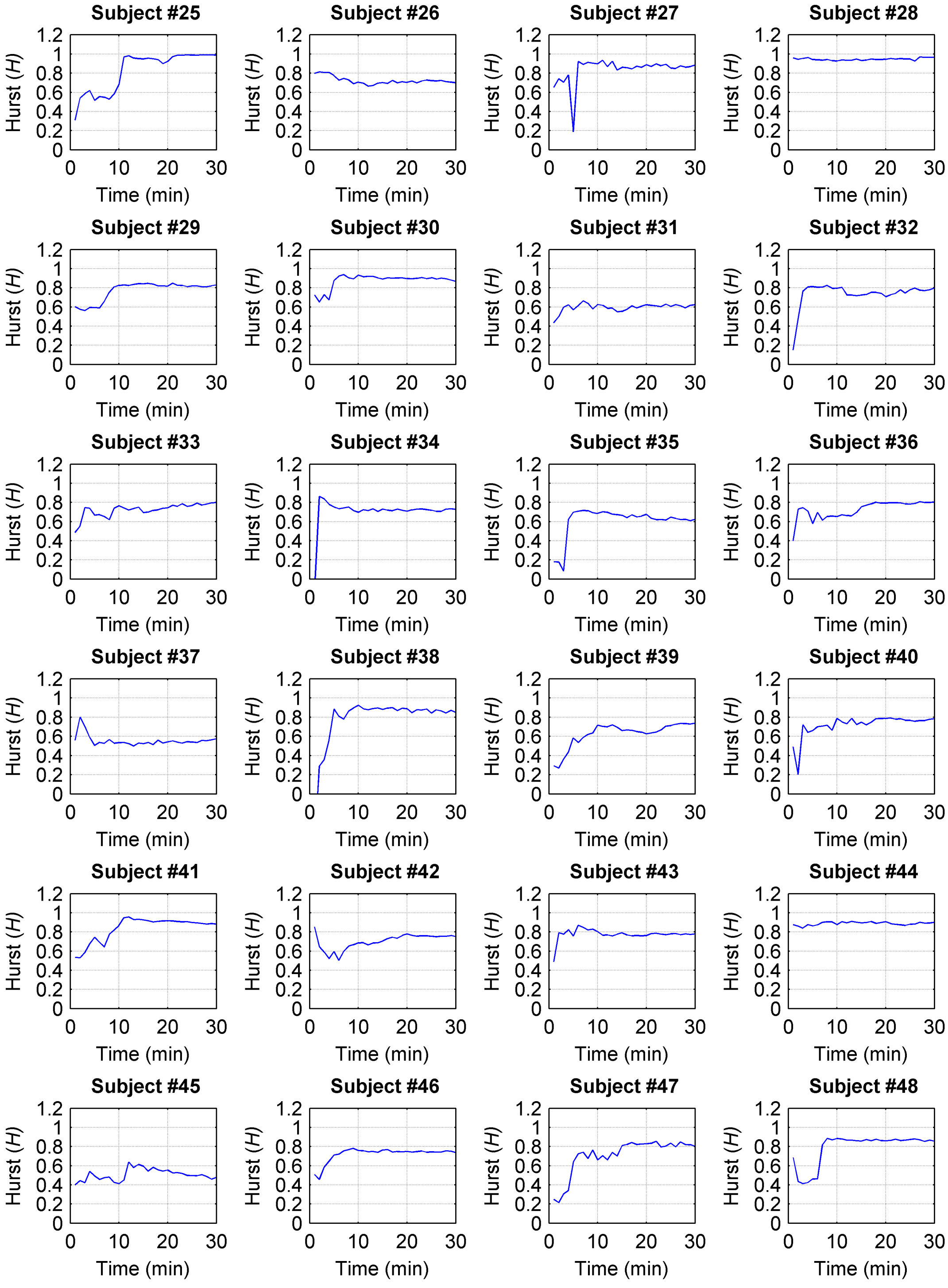

**Figure B.8:** Cardiac Index - CWE - Aggregated Variance - Abnormal HRV II

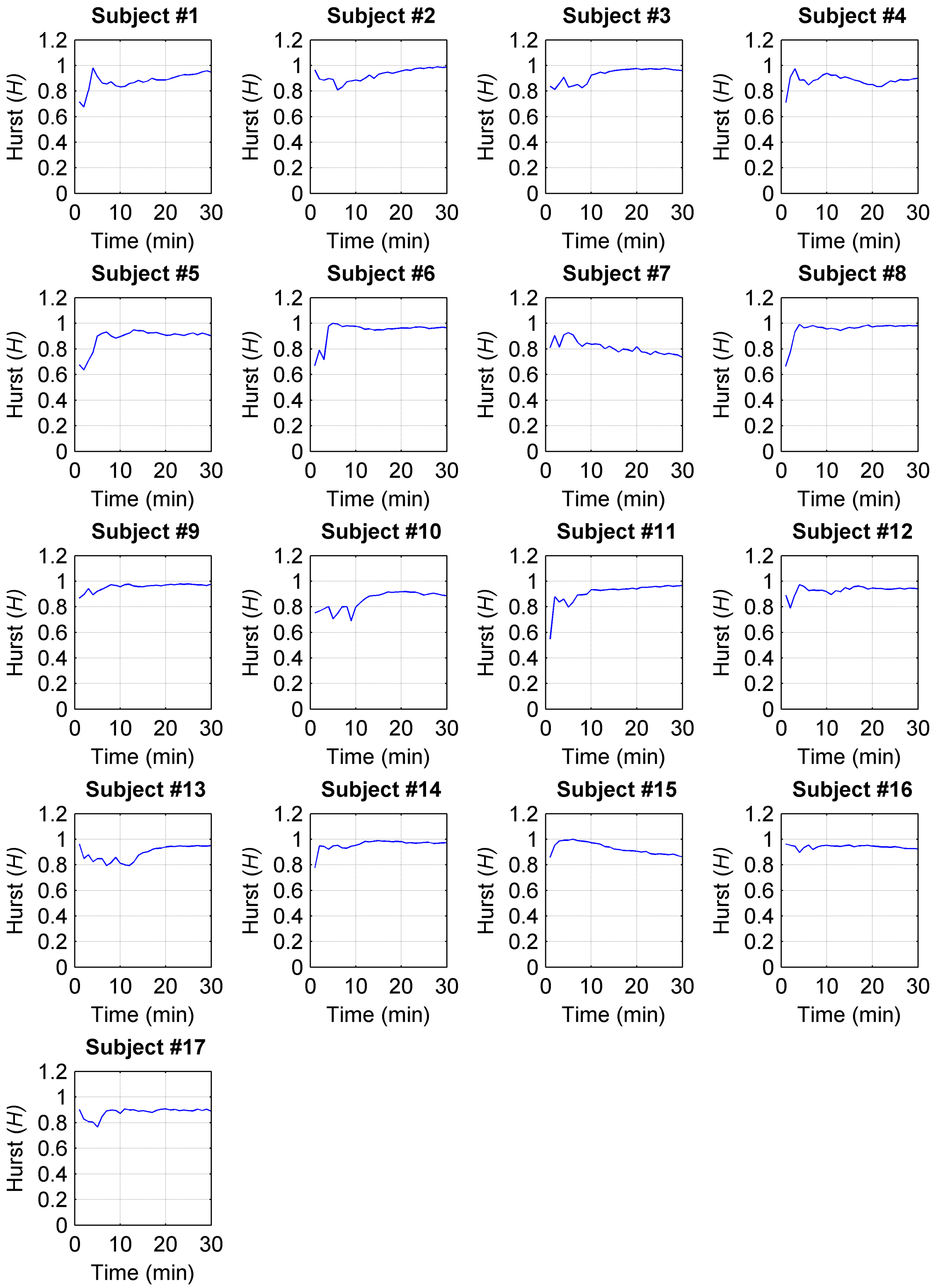

**Figure B.9:** Cardiac Index - CWE - Absolute Value - Normal HRV

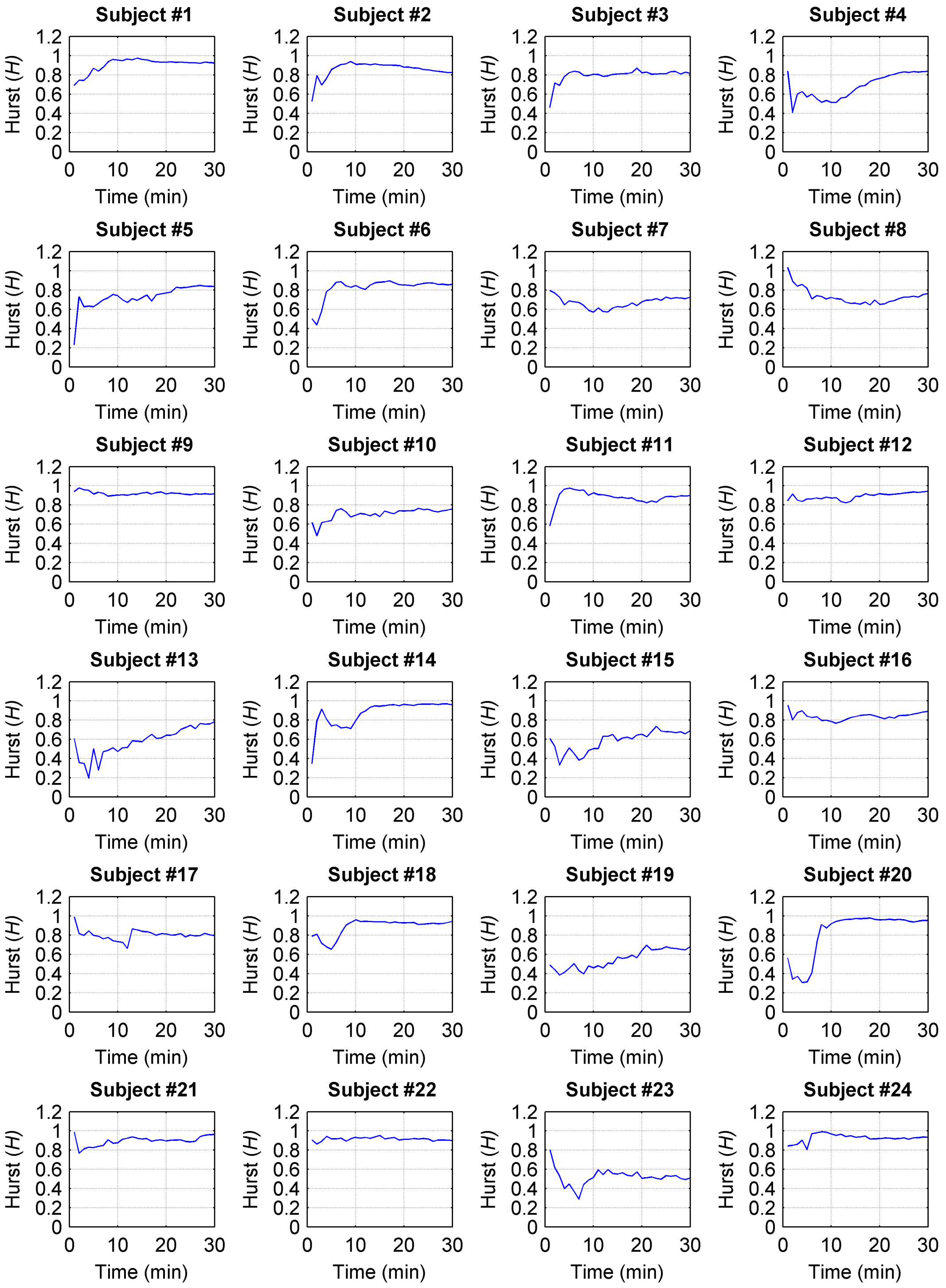

**Figure B.10:** Cardiac Index - CWE - Absolute Value - Abnormal HRV I

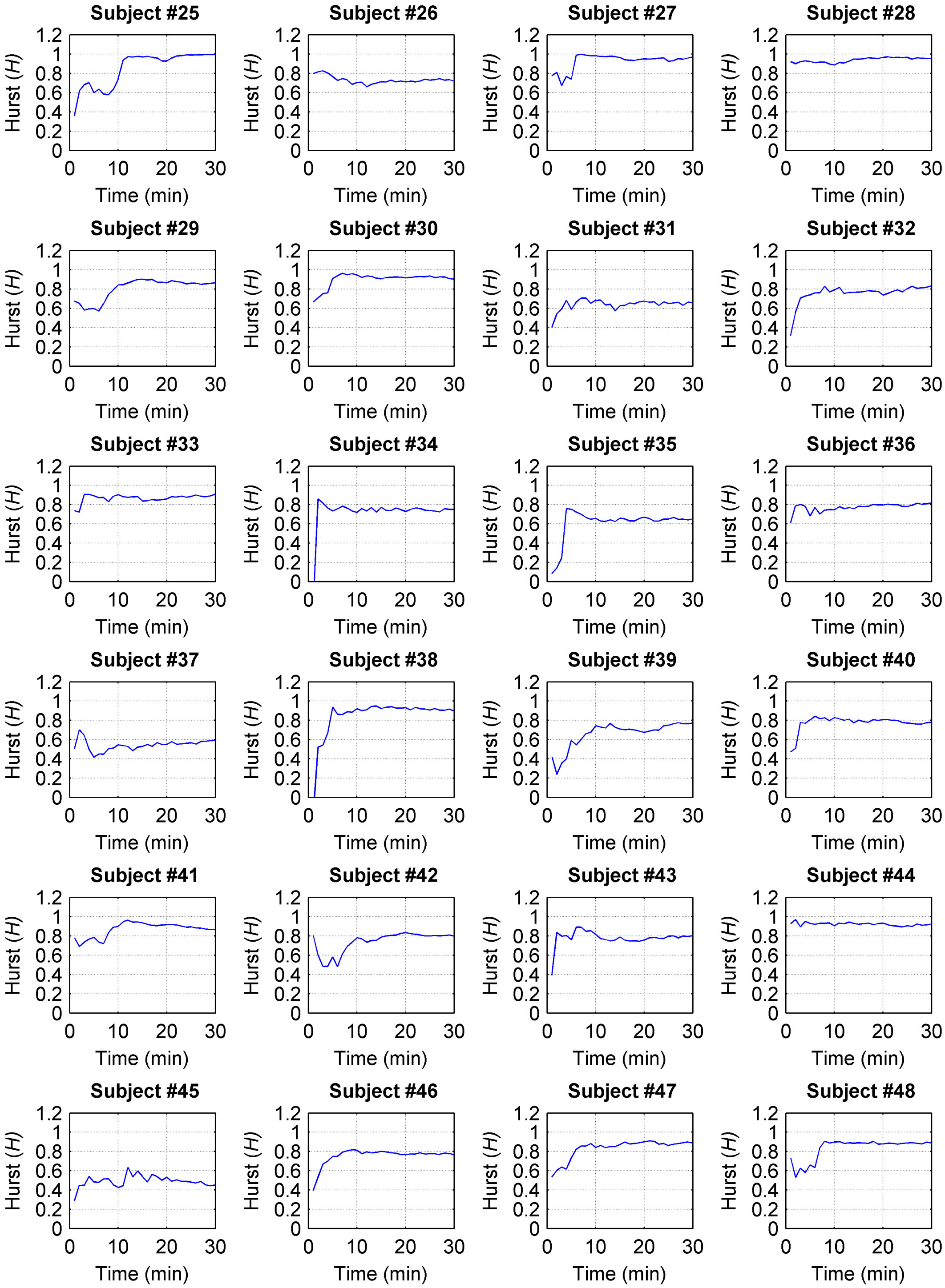

**Figure B.11:** Cardiac Index - CWE - Absolute Value - Abnormal HRV II

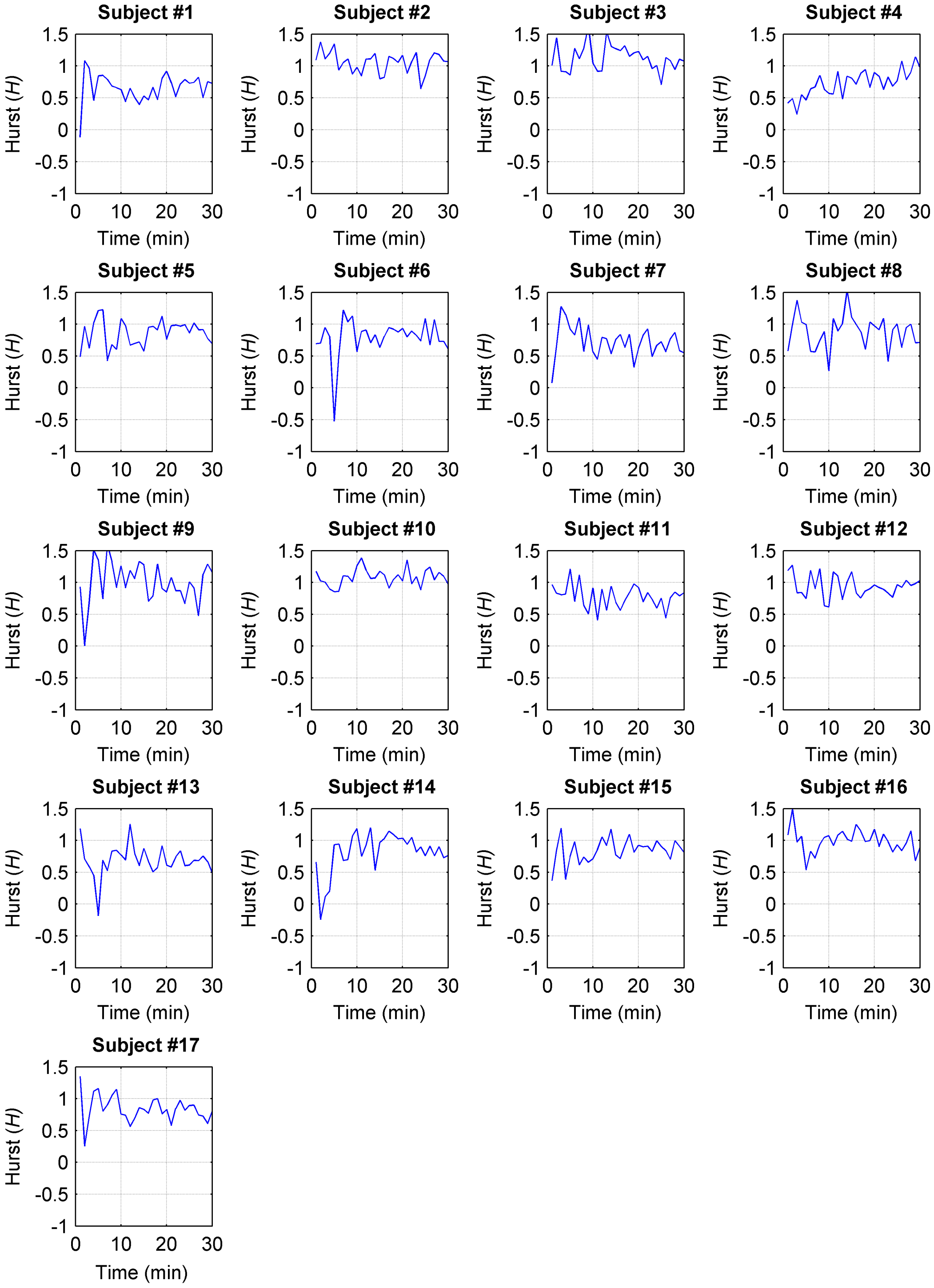

**Figure B.12:** Cardiac Index - CWE - Difference Variance - Normal HRV

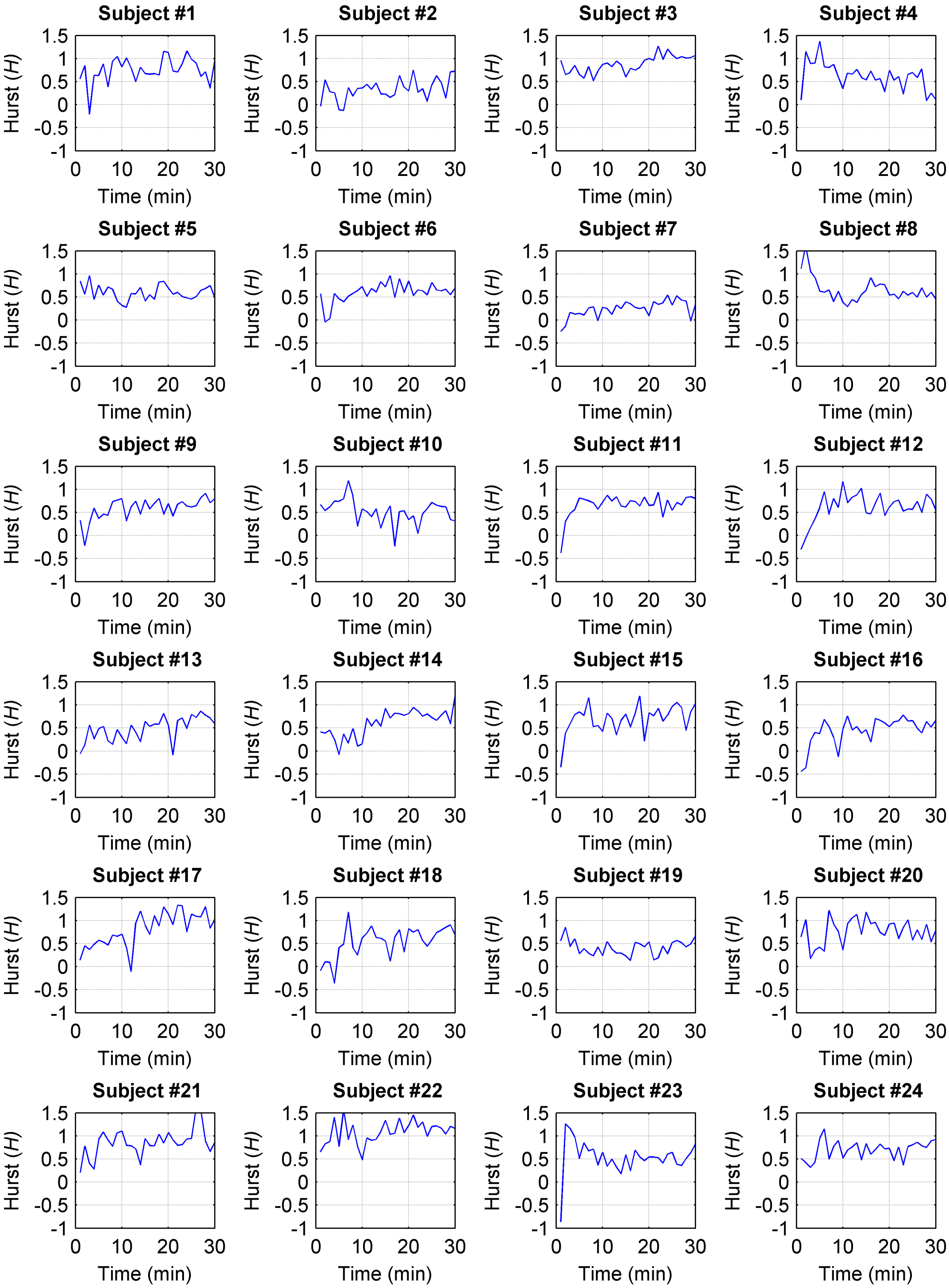

**Figure B.13:** Cardiac Index - CWE - Difference Variance - Abnormal HRV I

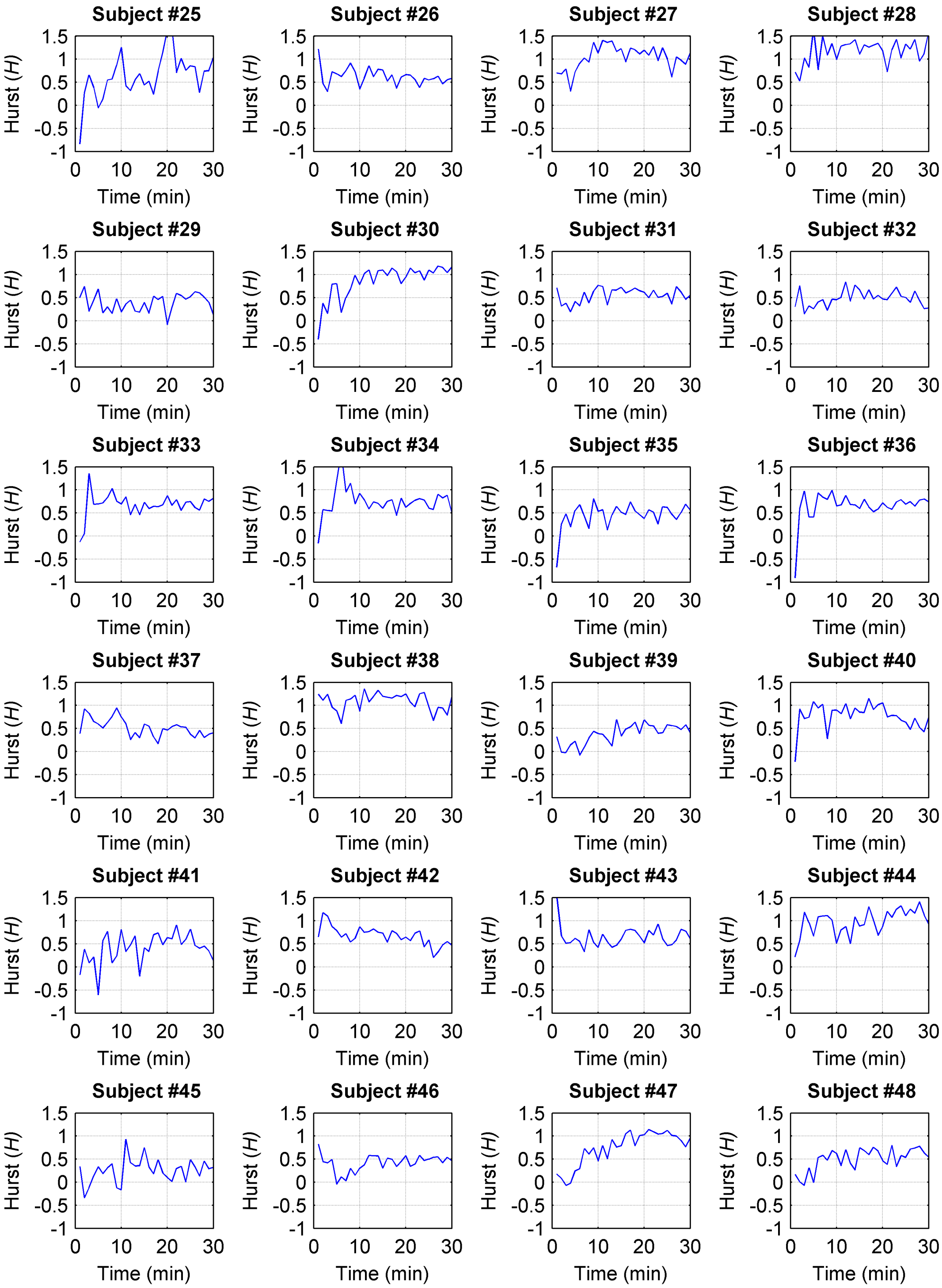

**Figure B.14:** Cardiac Index - CWE - Difference Variance - Abnormal HRV II

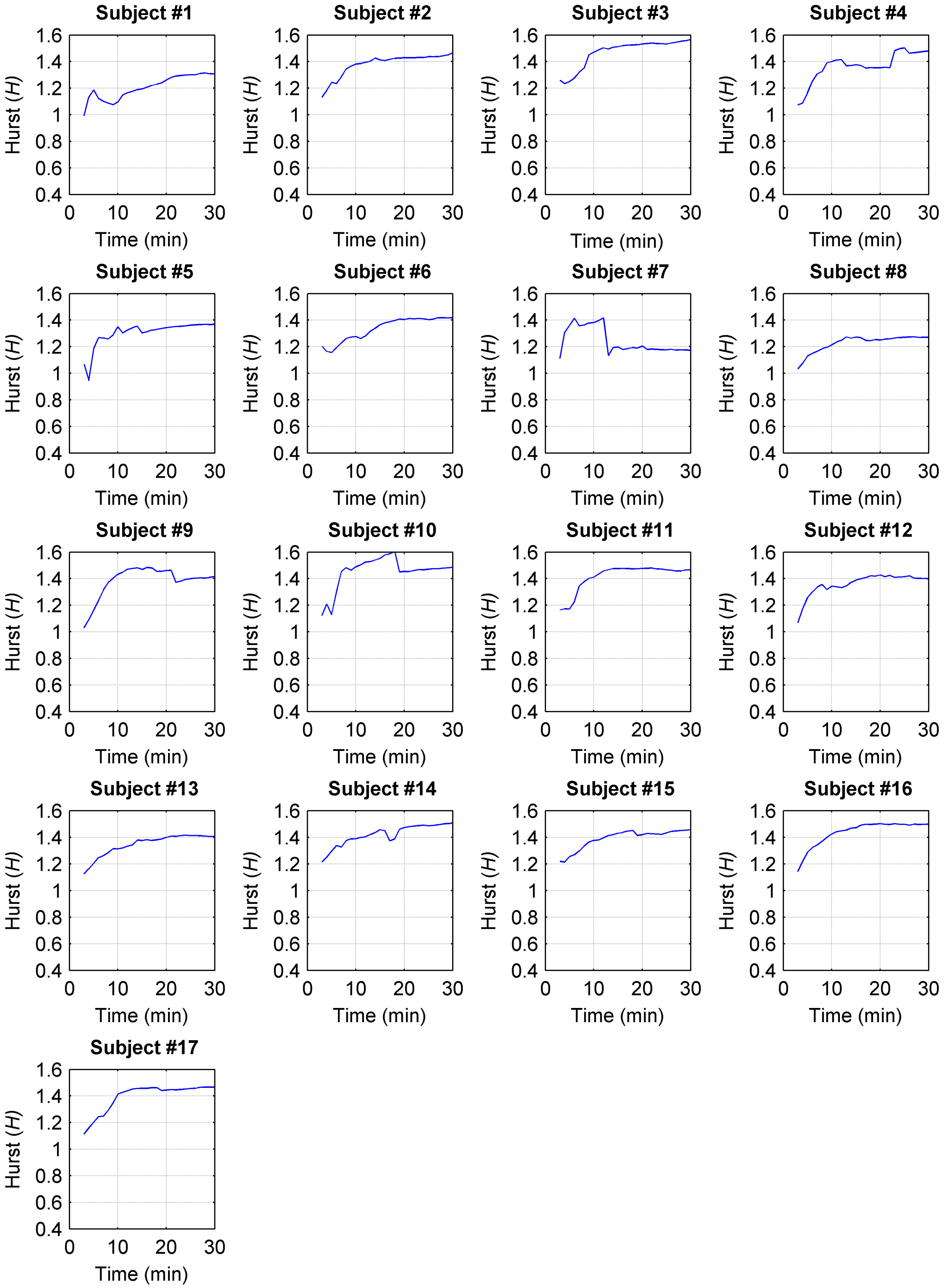

Subject #1 Subject #2 Subject #3 Subject #4 Subject #5 Subject #6 Subject #7 Subject #8 Subject #9 Subject #10 Subject #11 Subject #12 Subject #13 Subject #14 Subject #15 Subject #16 Subject #17

**Figure B.15:** Cardiac Index - CWE - Diffusion Entropy - Normal HRV

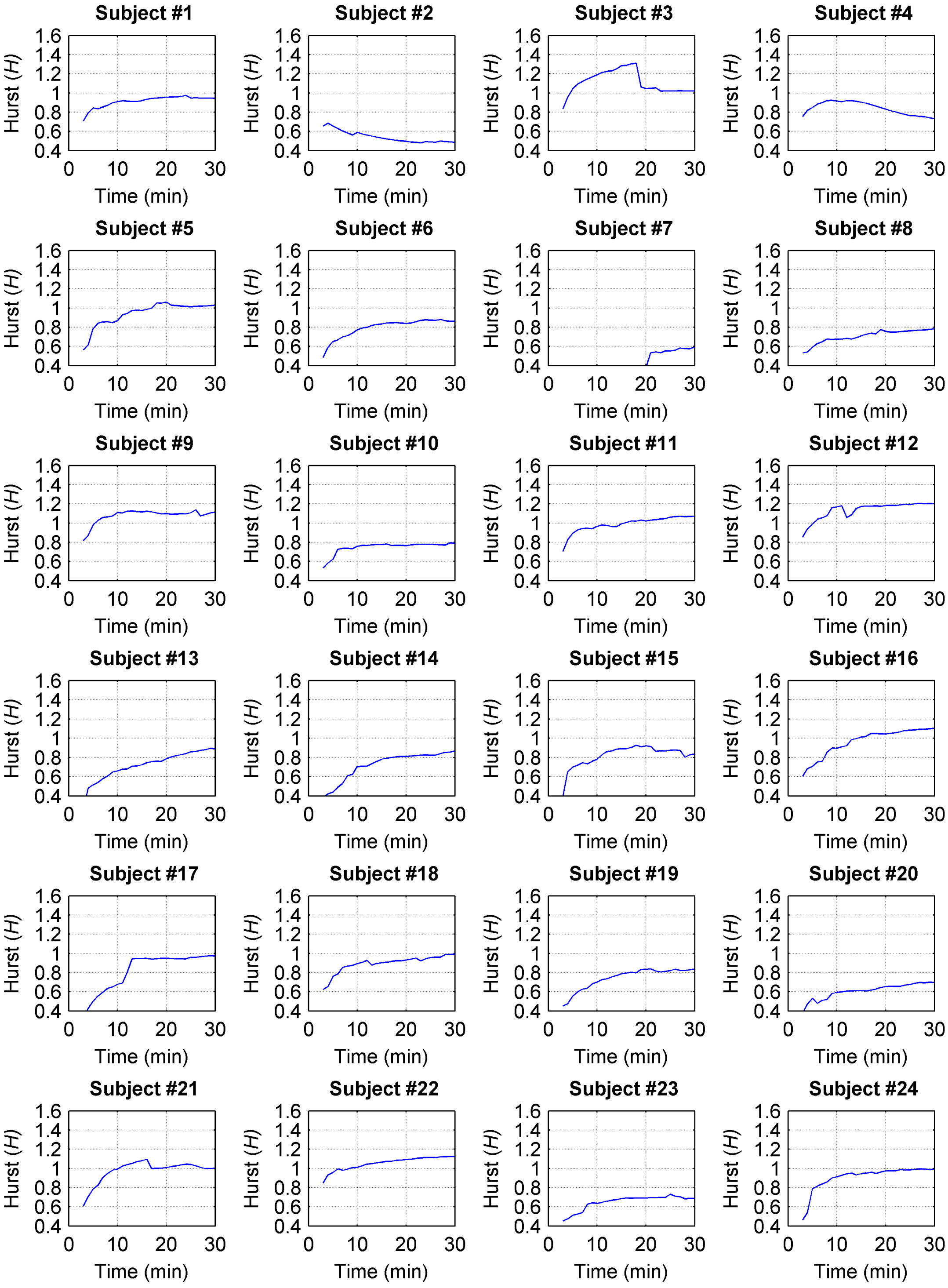

**Figure B.16:** Cardiac Index - CWE - Diffusion Entropy - Abnormal HRV I

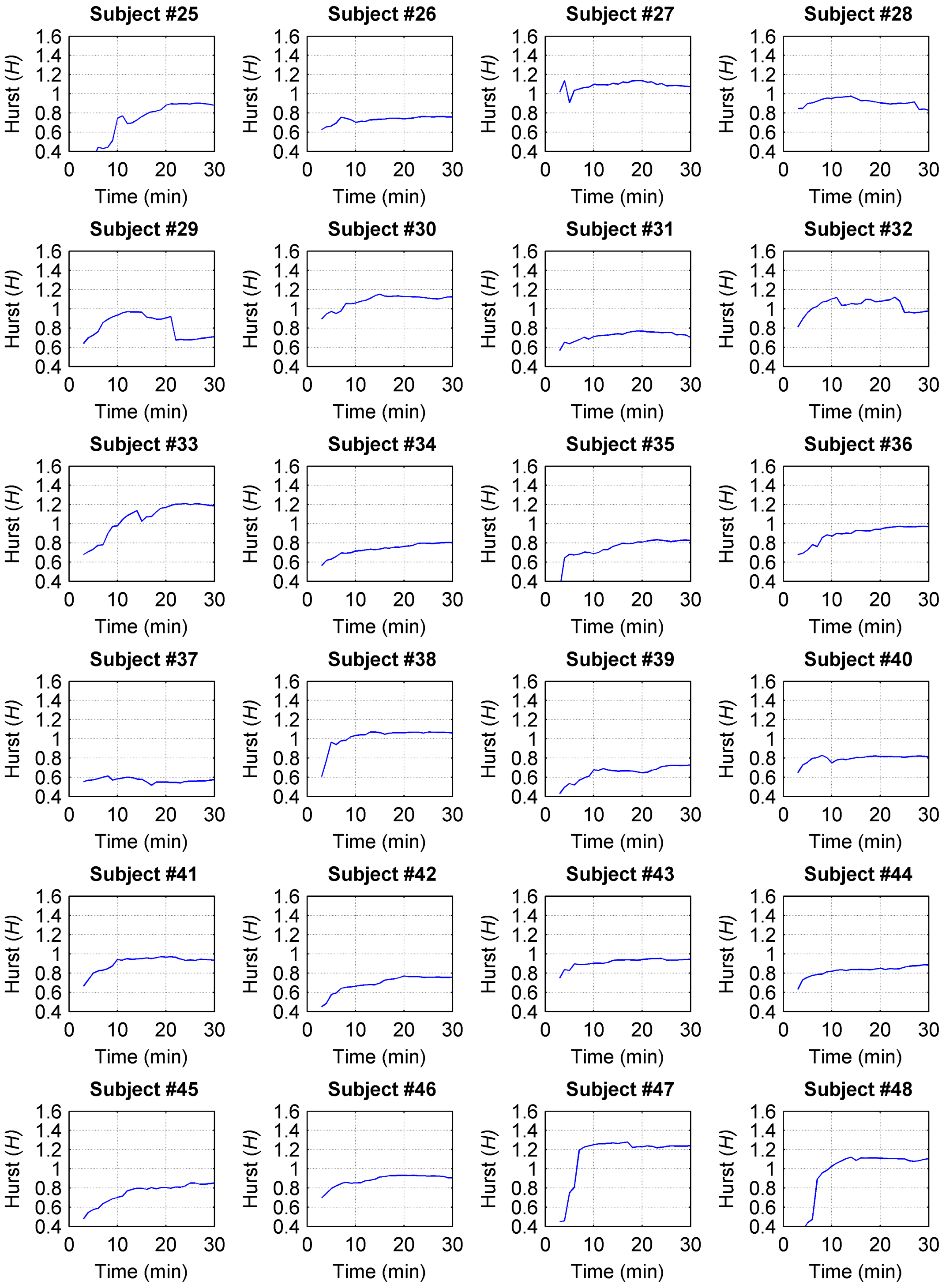

**Figure B.17:** Cardiac Index - CWE - Diffusion Entropy - Abnormal HRV II

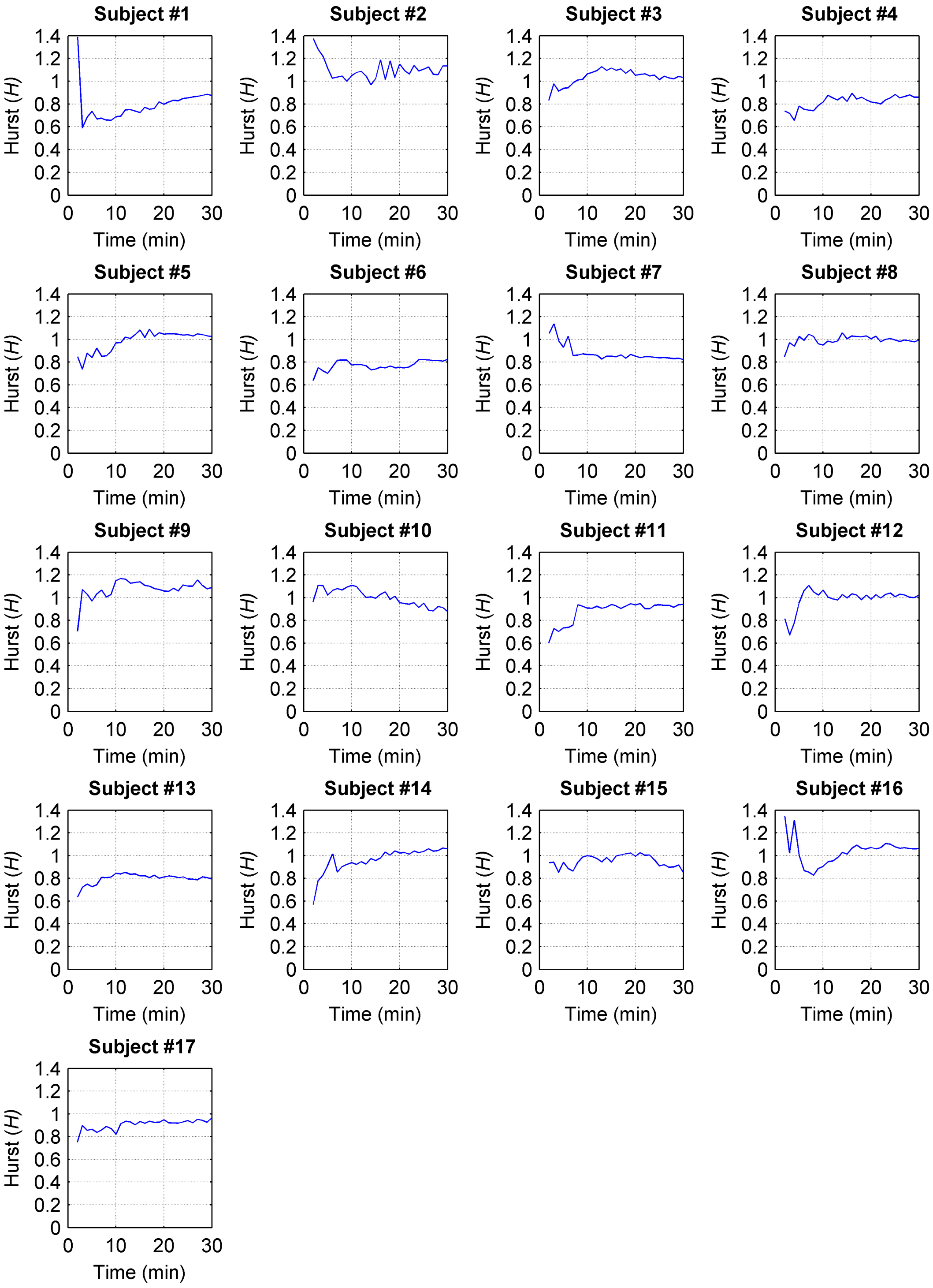

**Figure B.18:** Cardiac Index - CWE - Peng - Normal HRV

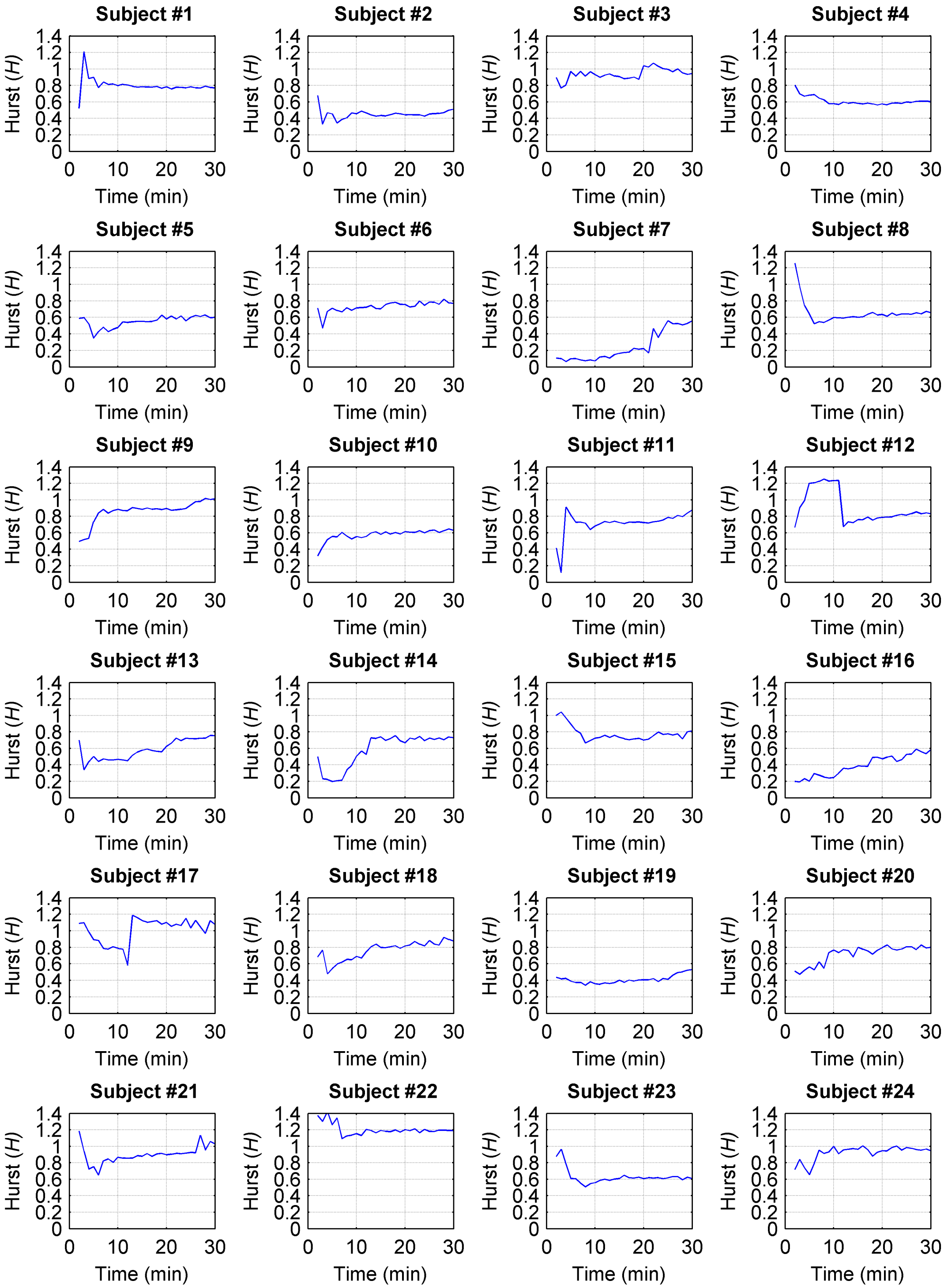

**Figure B.19:** Cardiac Index - CWE - Peng - Abnormal HRV I

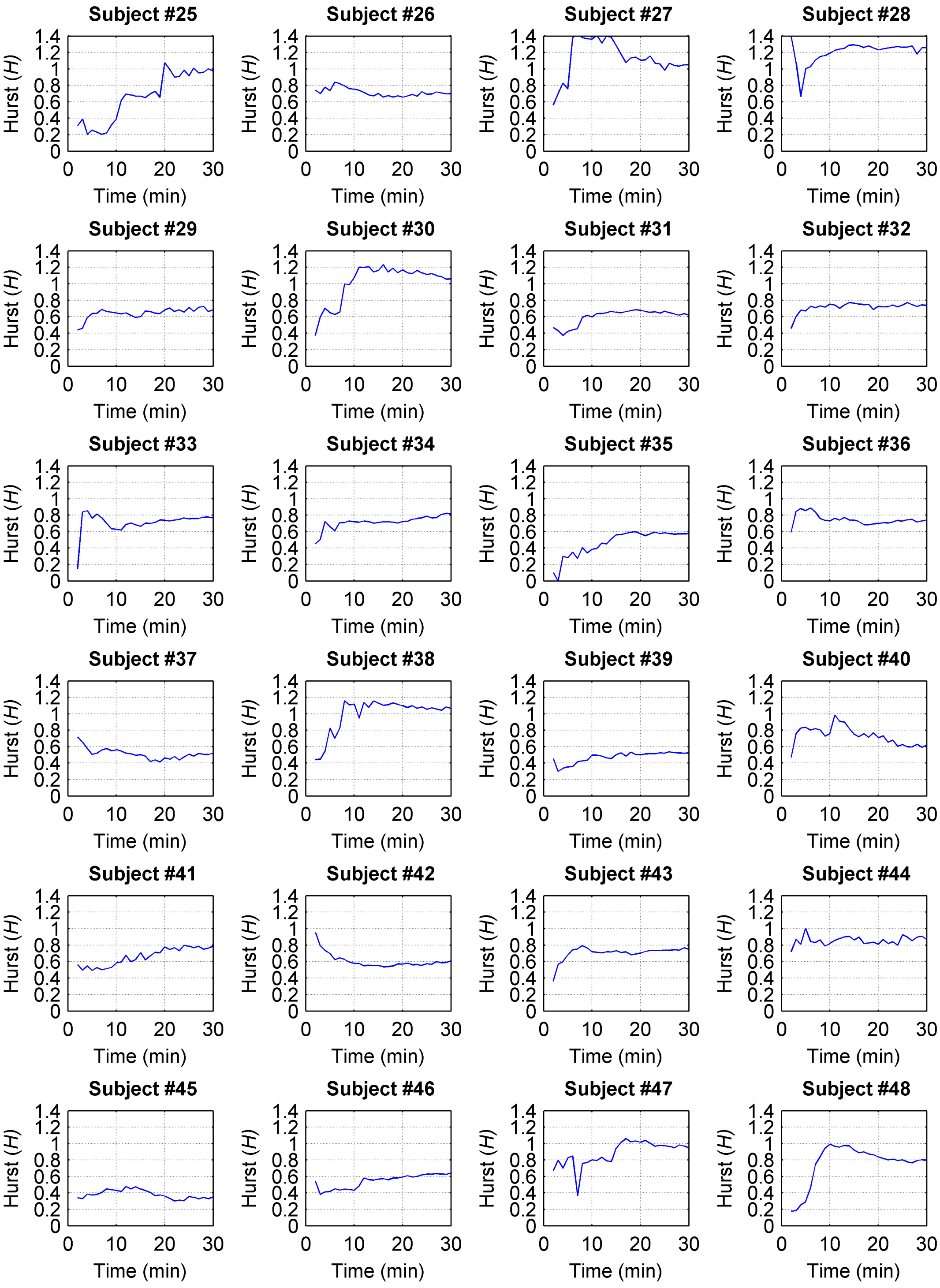

**Figure B.20:** Cardiac Index - CWE - Peng - Abnormal HRV II

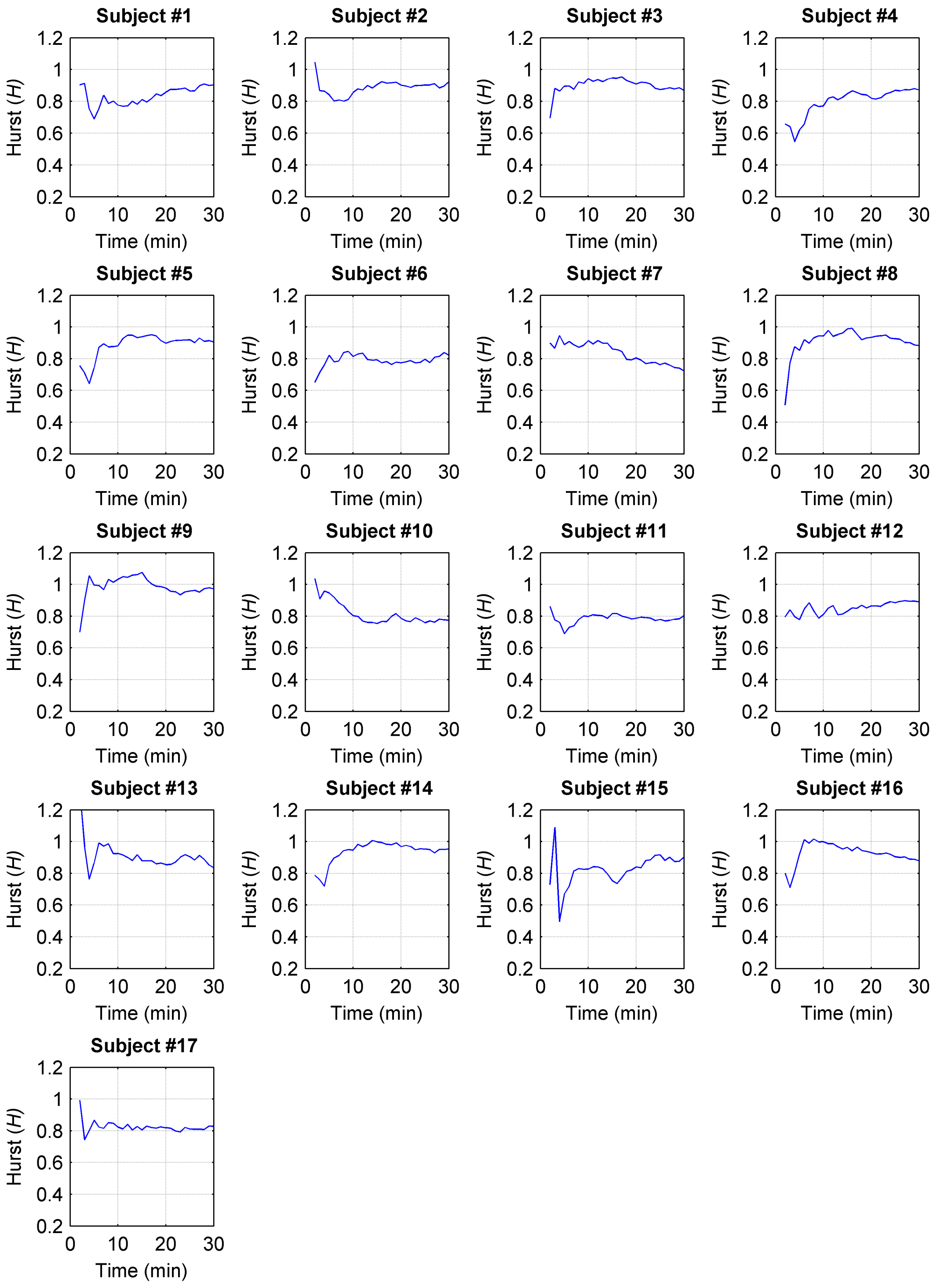

**Figure B.21:** Cardiac Index - CWE - Rescaled Range - Normal HRV

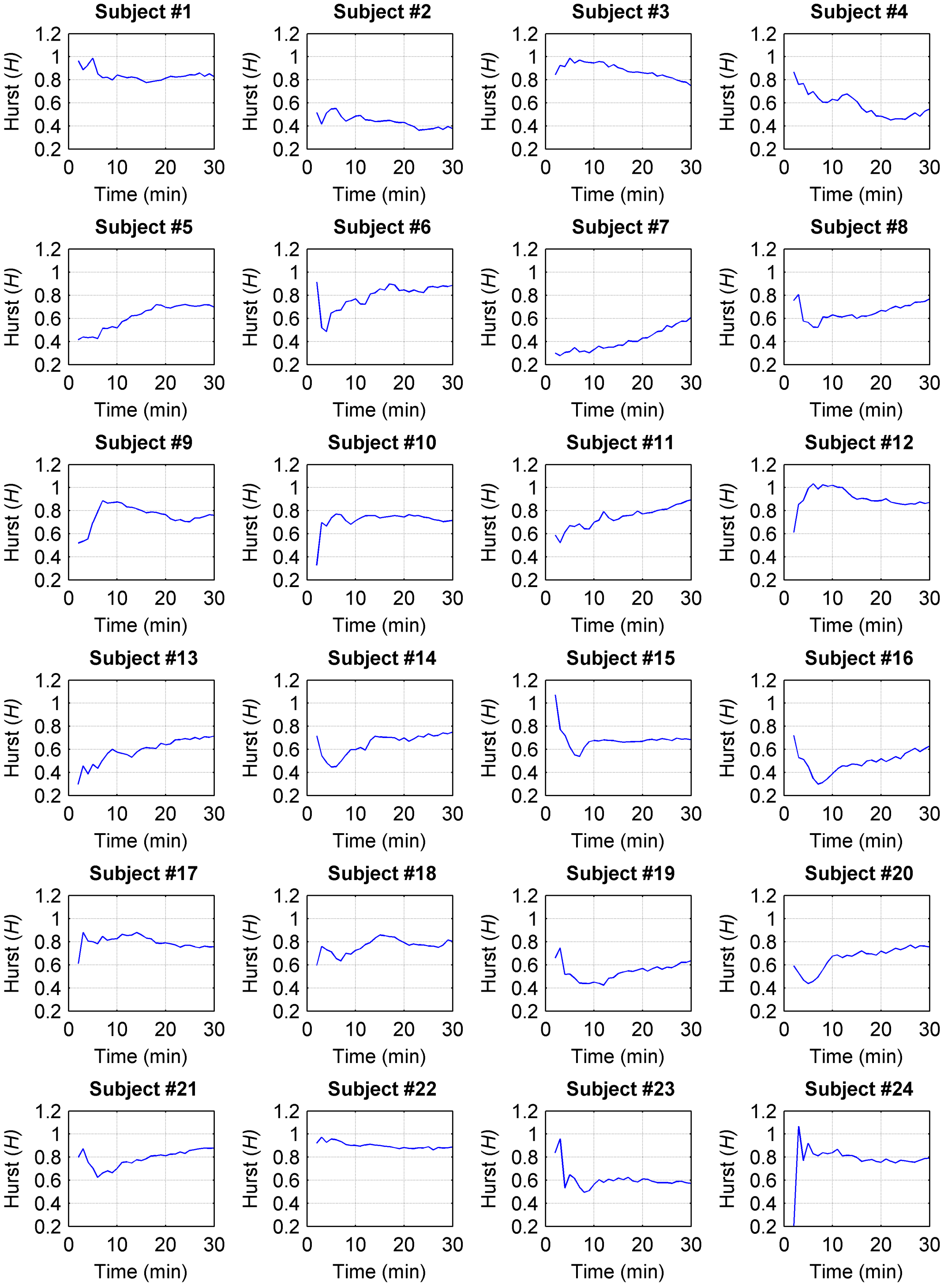

**Figure B.22:** Cardiac Index - CWE - Rescaled Range - Abnormal HRV I

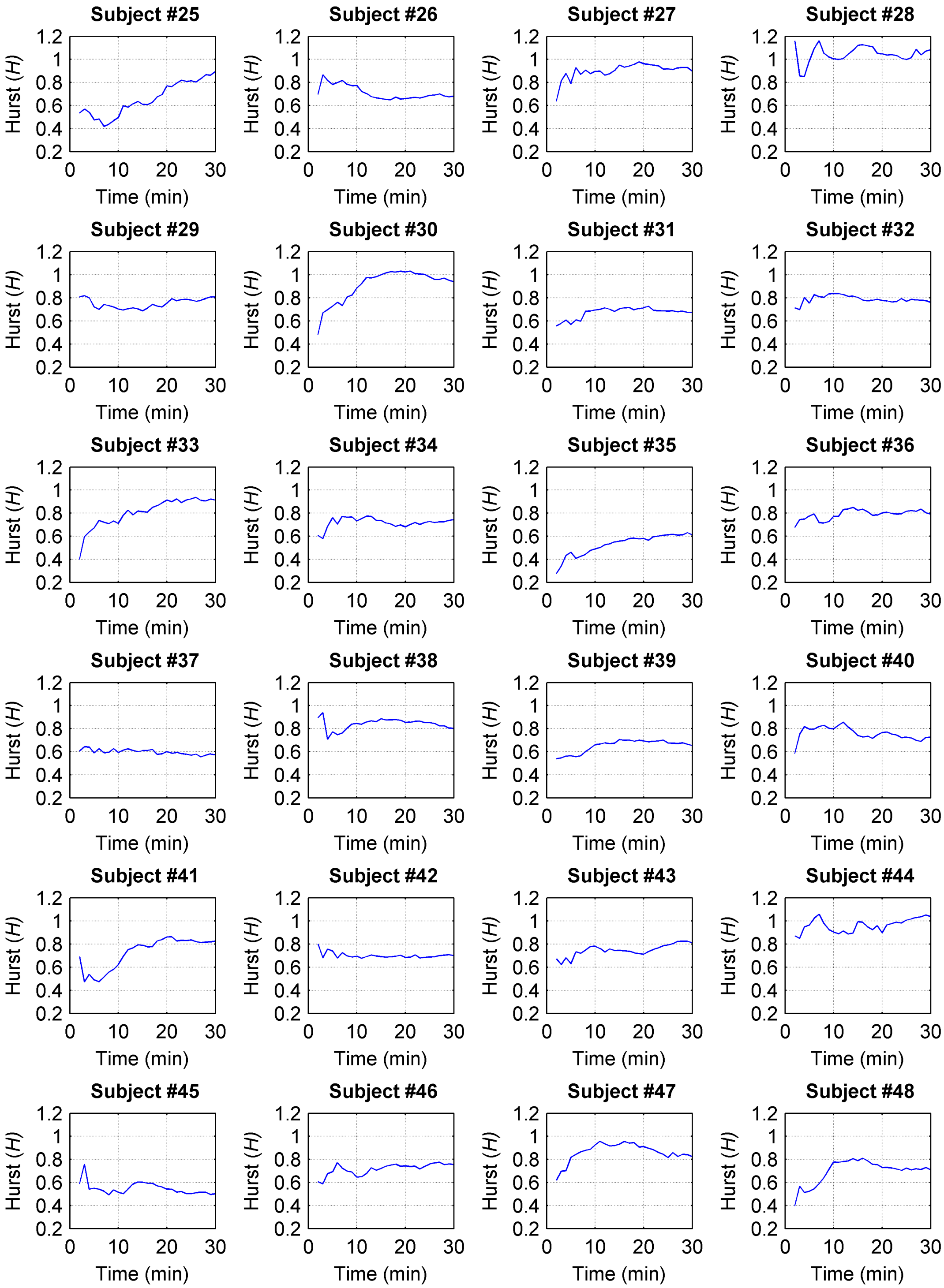

**Figure B.23:** Cardiac Index - CWE - Rescaled Range - Abnormal HRV II

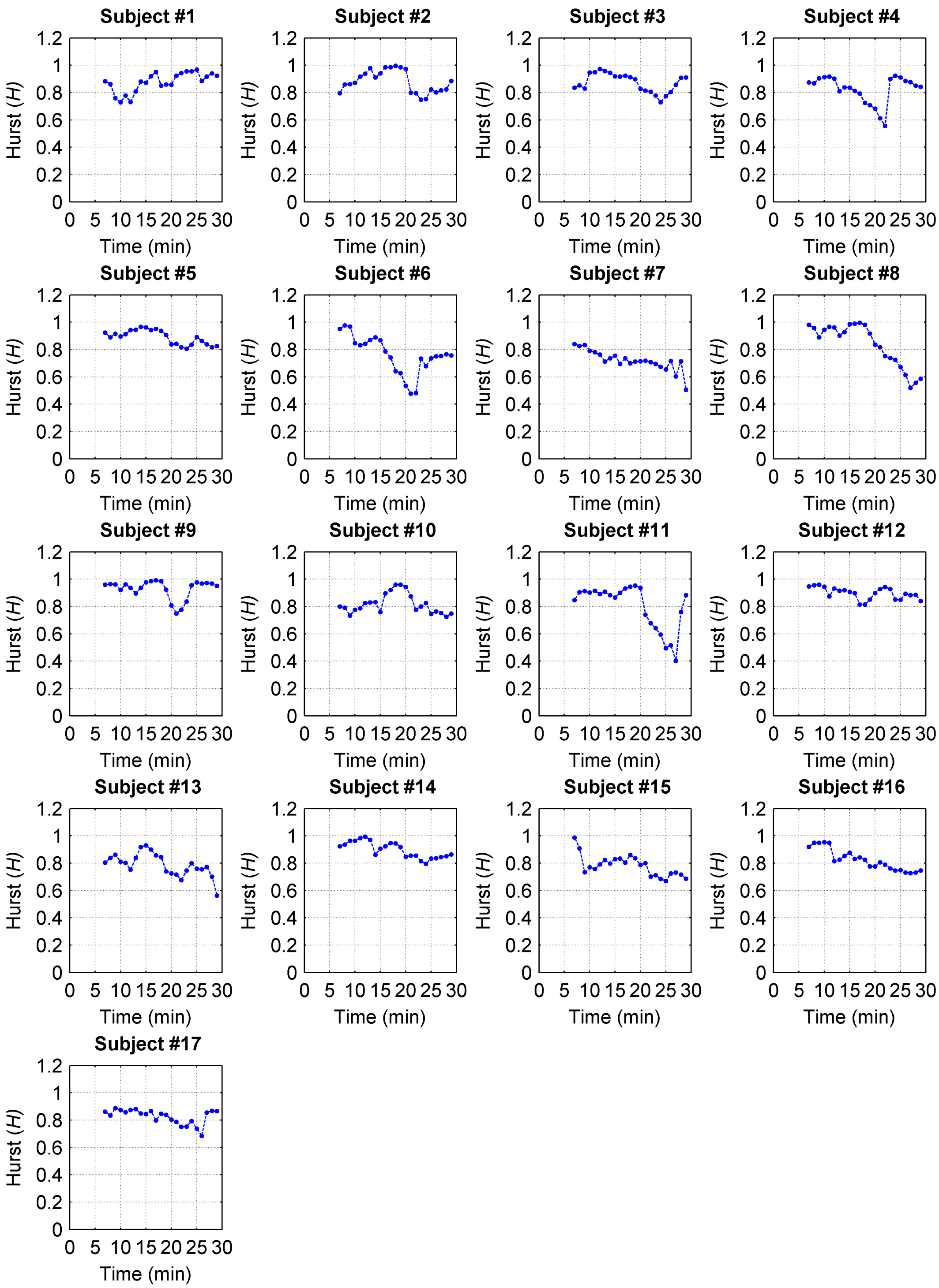

**Figure B.24:** Cardiac Index - SWE Aggregated Variance - Normal HRV

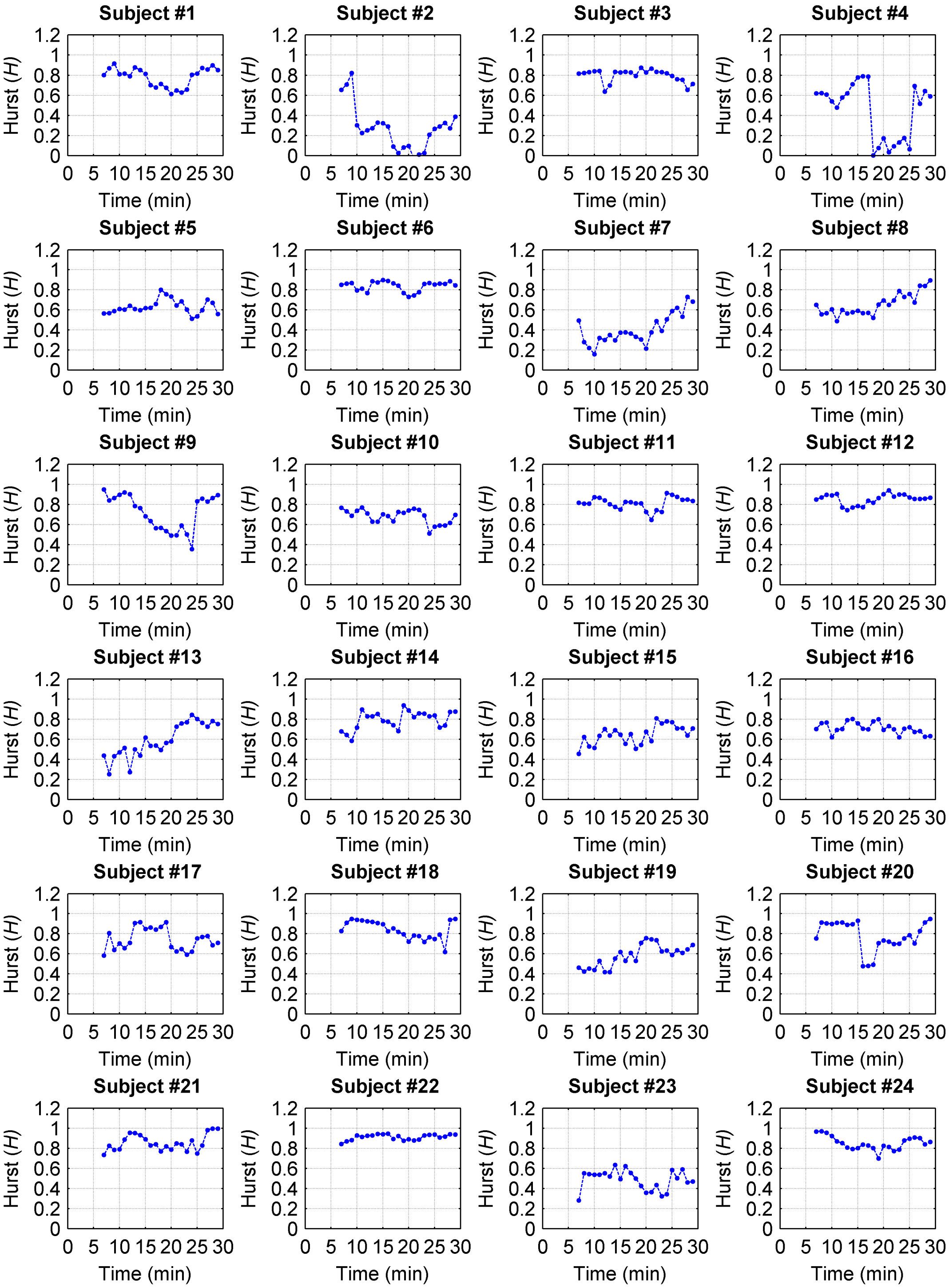

**Figure B.25:** Cardiac Index - SWE Aggregated Variance - Abnormal HRV I

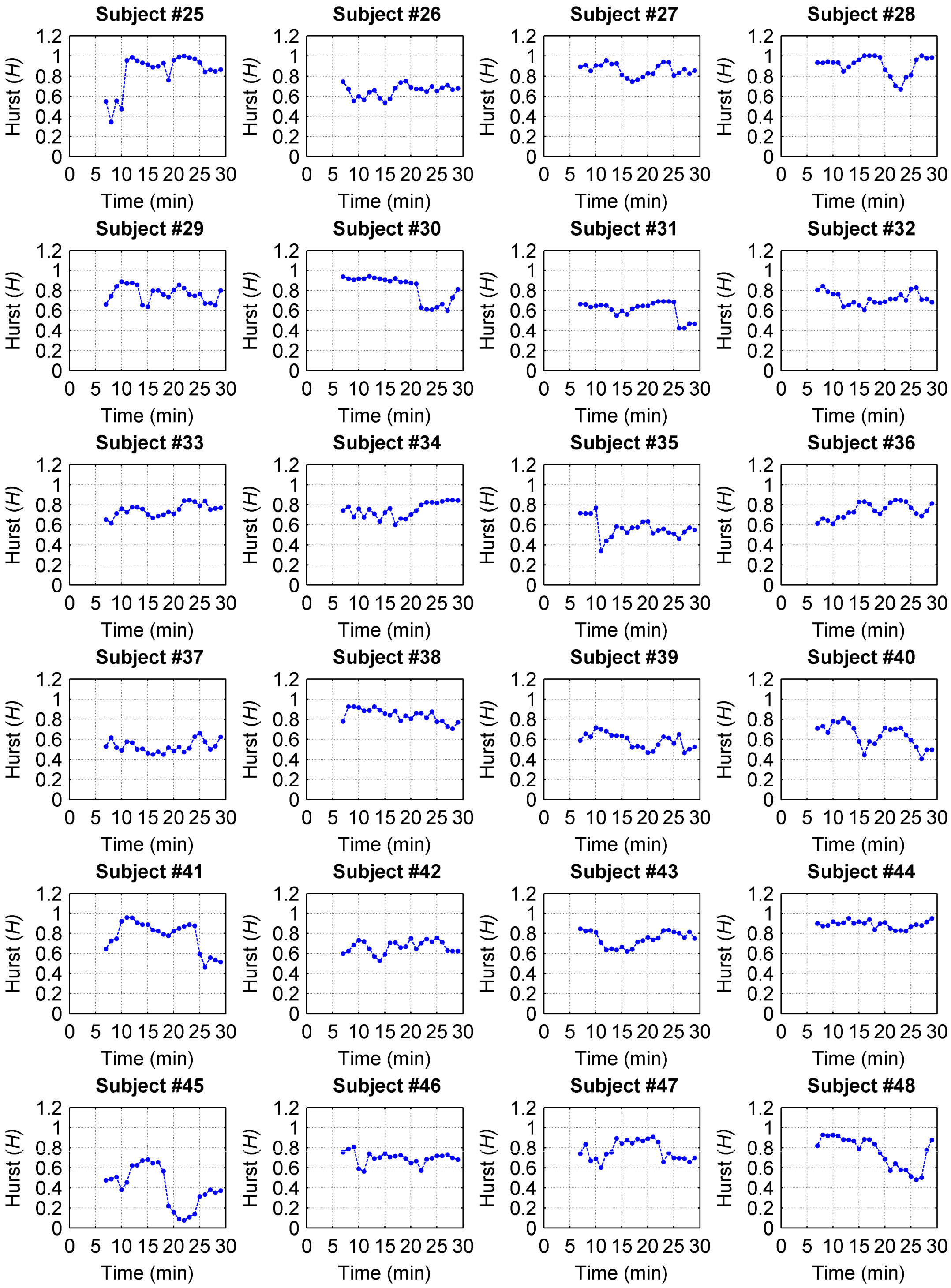

**Figure B.26:** Cardiac Index - SWE Aggregated Variance - Abnormal HRV II

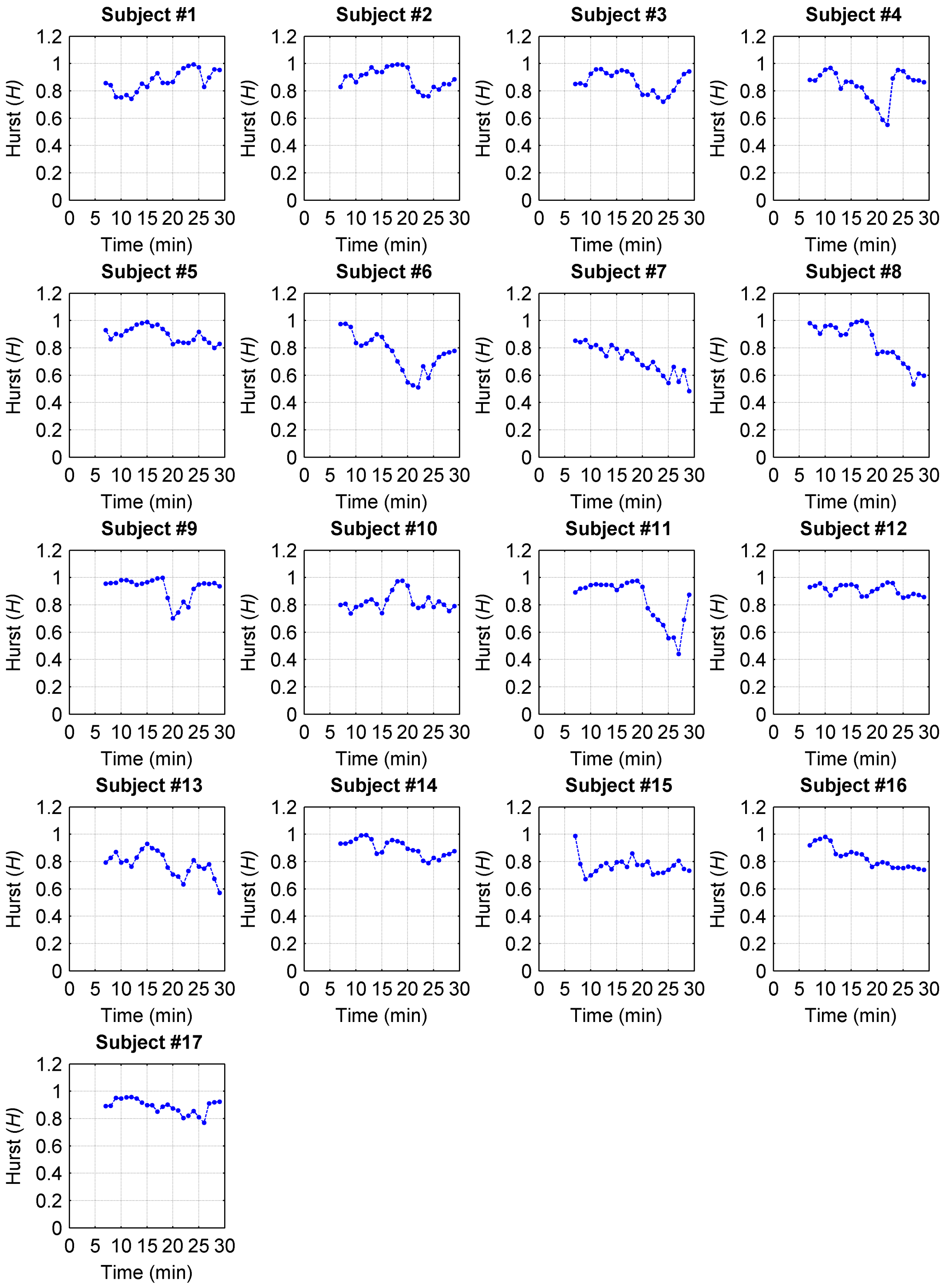

**Figure B.27:** Cardiac Index - SWE - Absolute Value - Normal HRV

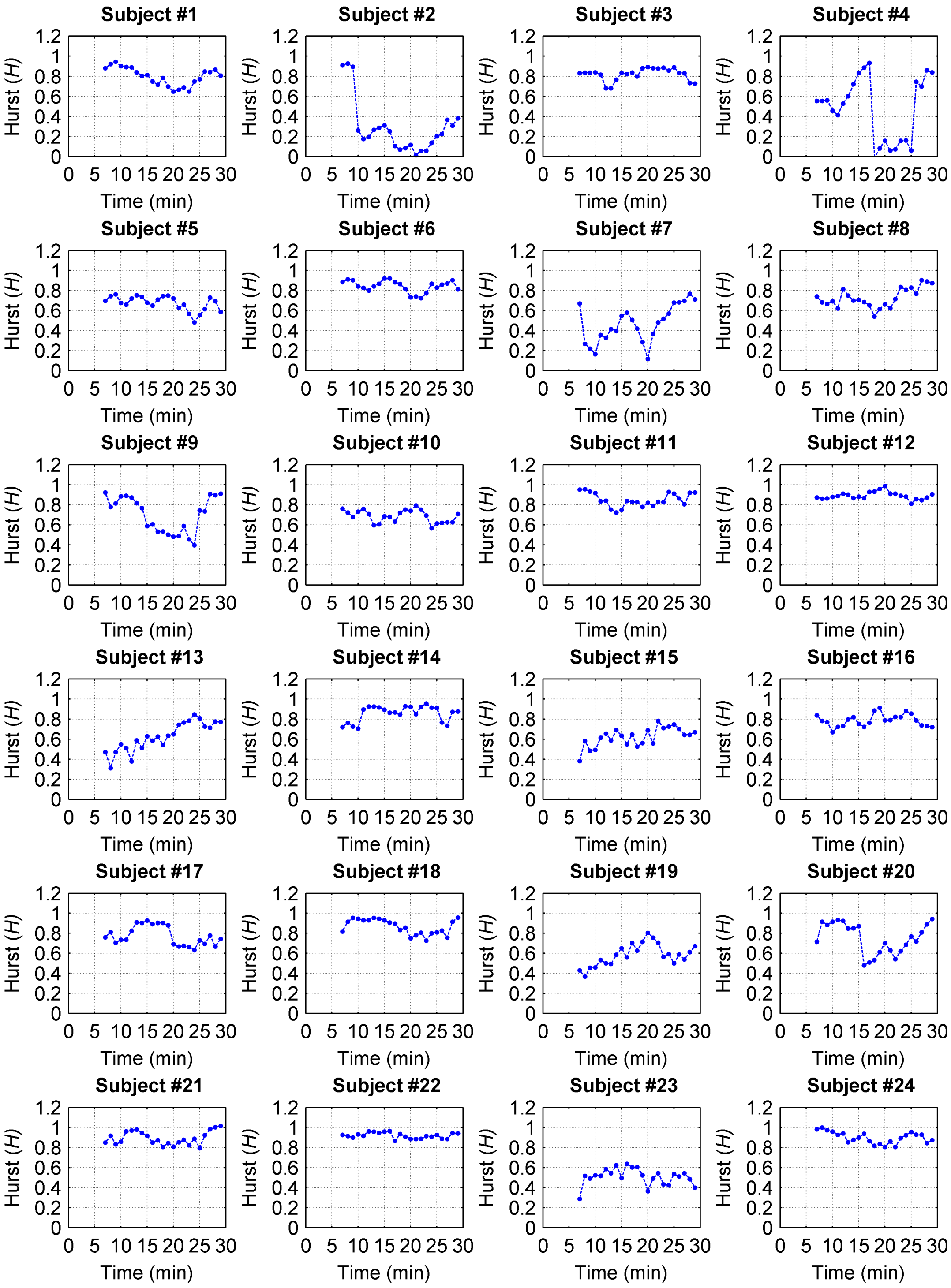
Subject #1 Subject #2 Subject #3 Subject #4 Subject #5 Subject #6 Subject #7 Subject #8 Subject #9 Subject #10 Subject #11 Subject #12 Subject #13 Subject #14 Subject #15 Subject #16 Subject #17 Subject #18 Subject #19 Subject #20 Subject #21 Subject #22 Subject #23 Subject #24

**Figure B.28:** Cardiac Index - SWE - Absolute Value - Abnormal HRV I

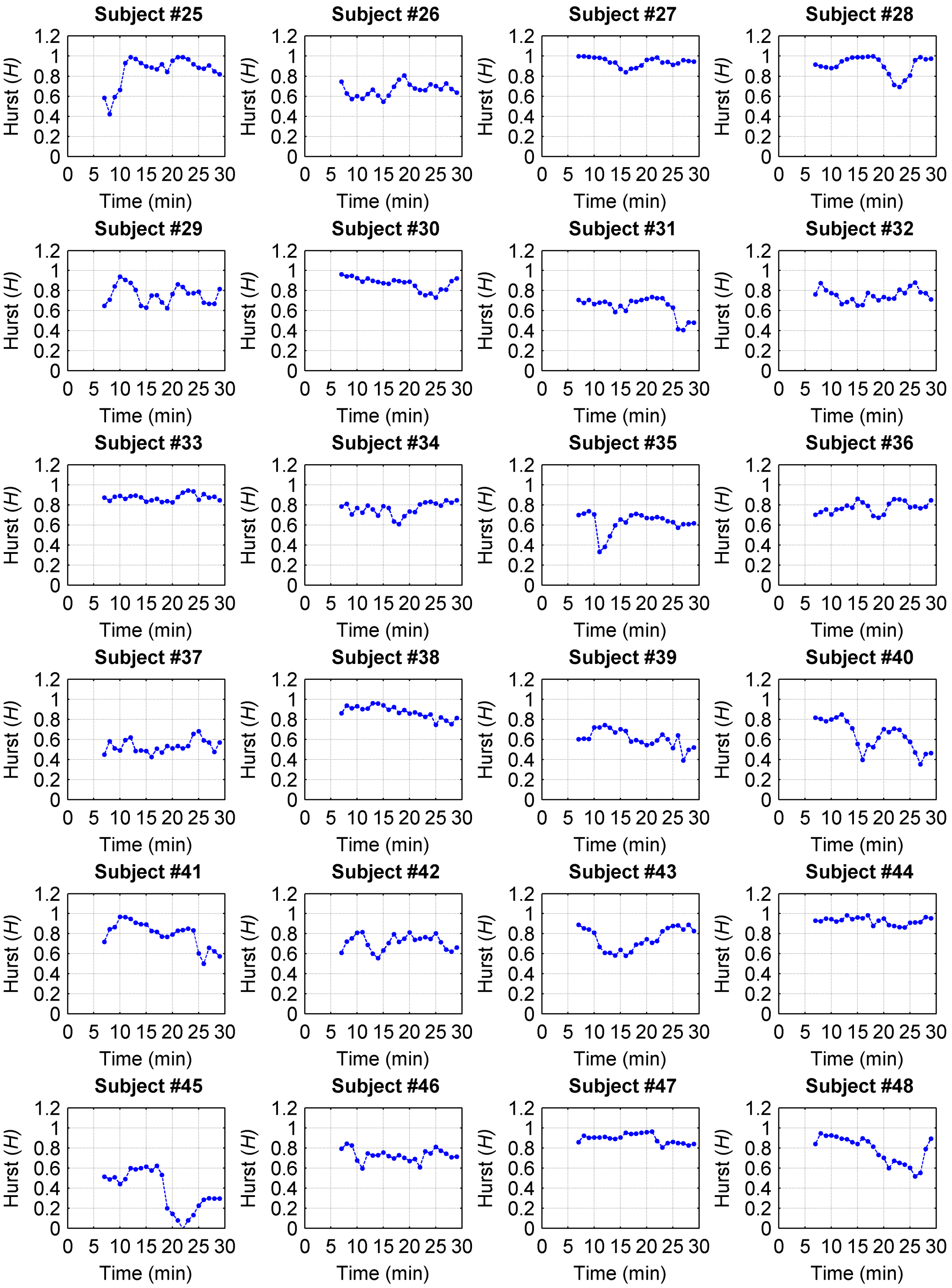

**Figure B.29:** Cardiac Index - SWE - Absolute Value - Abnormal HRV II

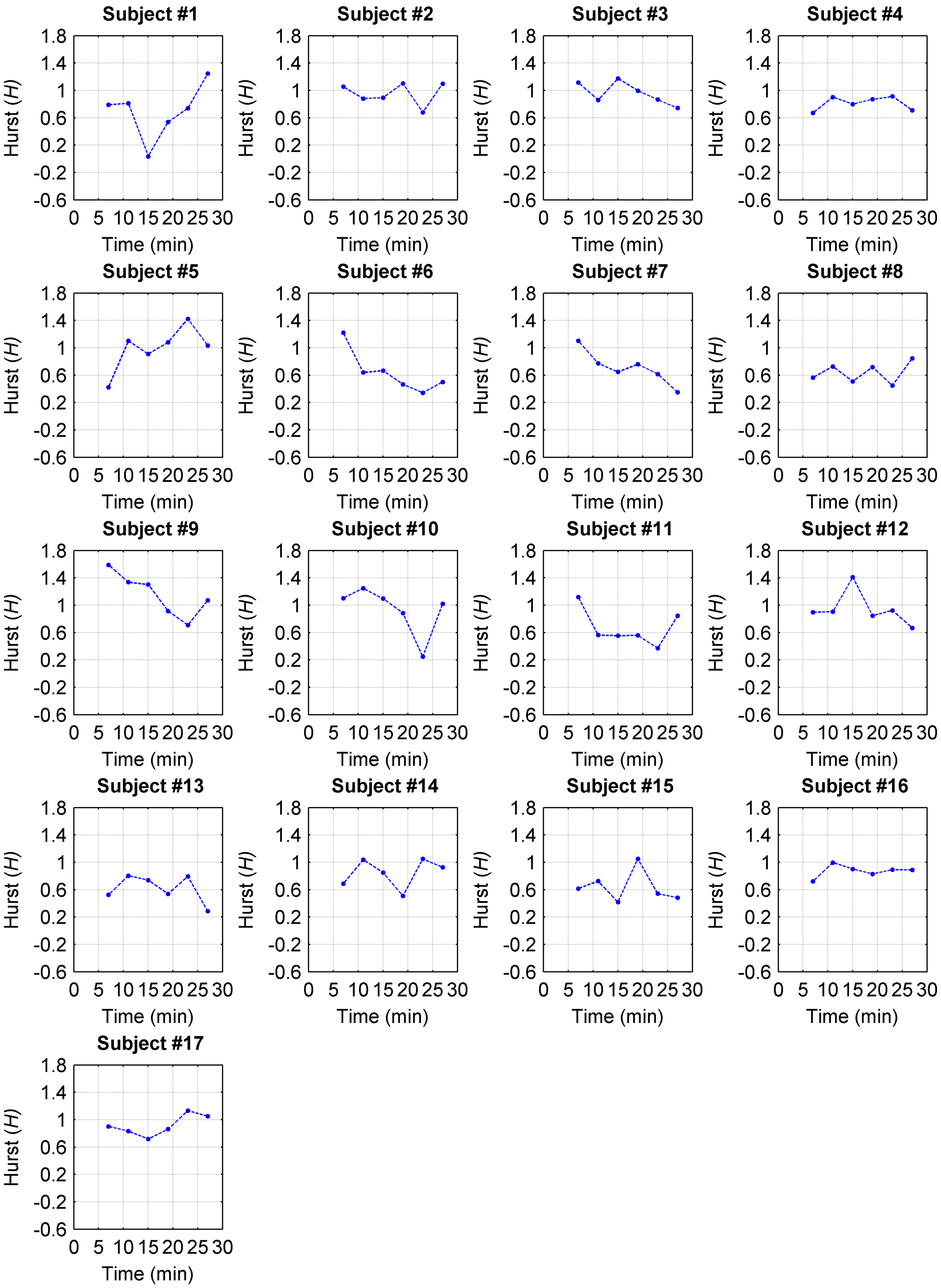

**Figure B.30:** Cardiac Index - SWE - Difference Variance - Normal HRV

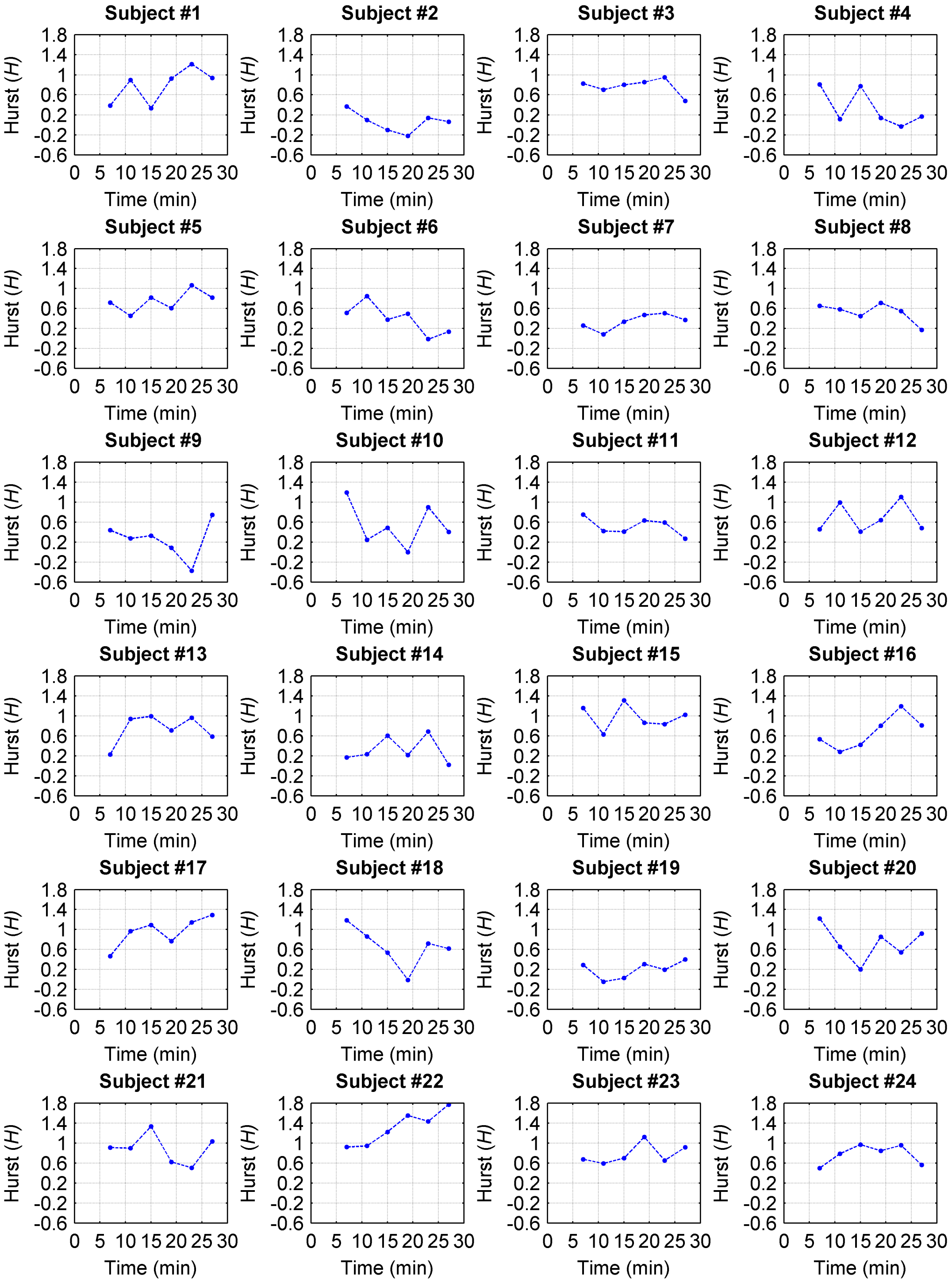

**Figure B.31:** Cardiac Index - SWE - Difference Variance - Abnormal HRV I

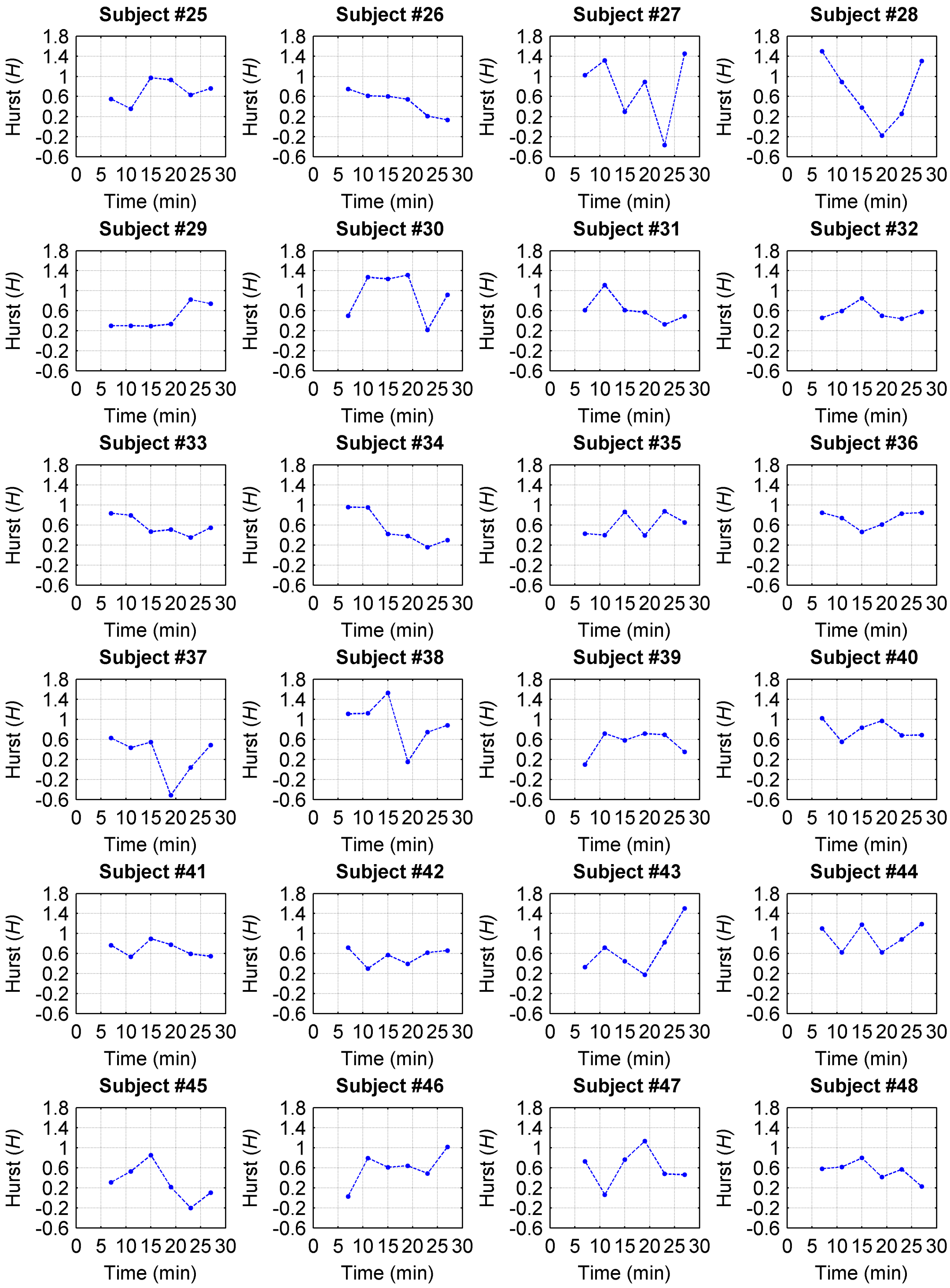

**Figure B.32:** Cardiac Index - SWE - Difference Variance - Abnormal HRV II

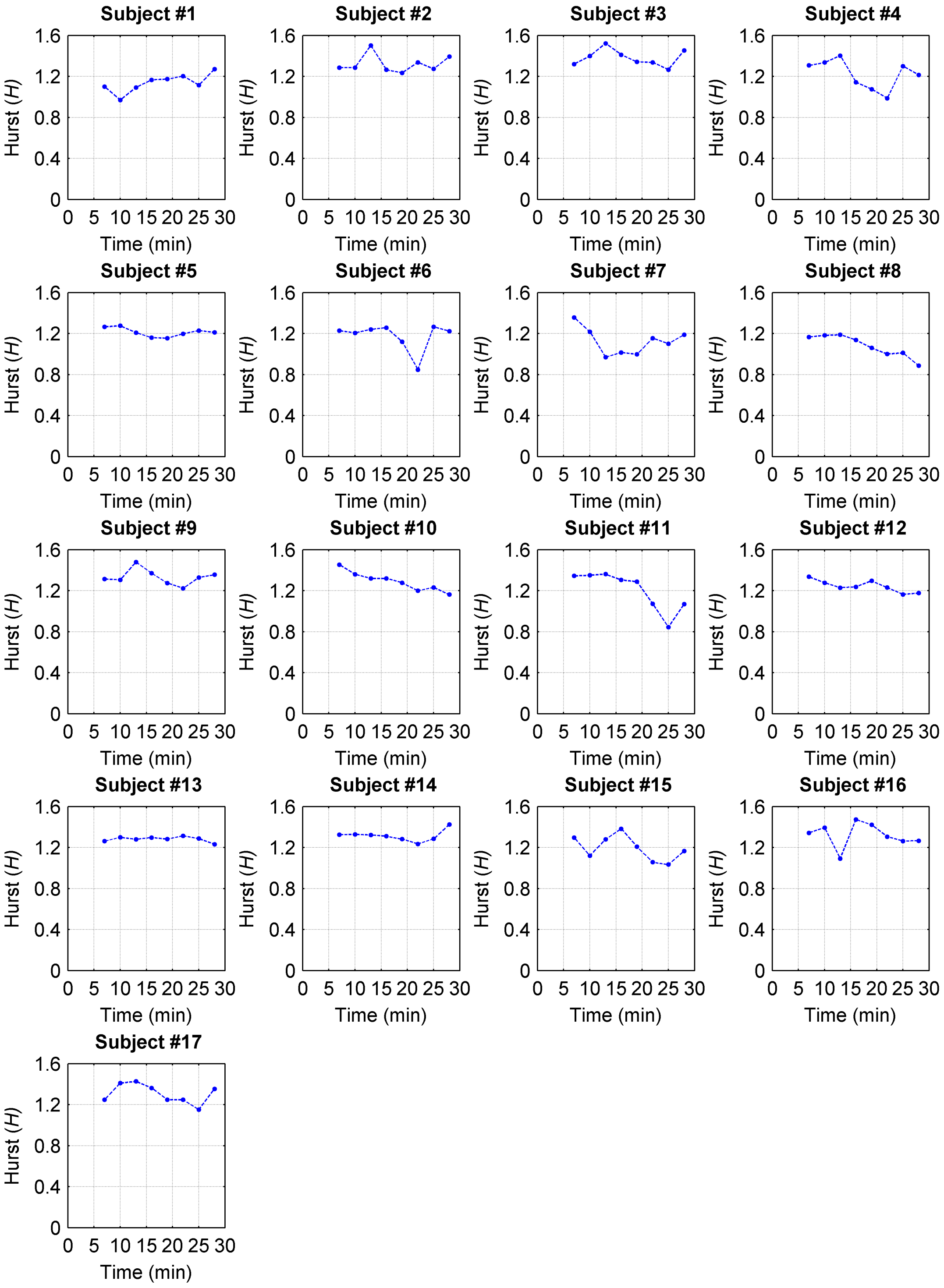

**Figure B.33:** Cardiac Index - SWE - Diffusion Entropy - Normal HRV

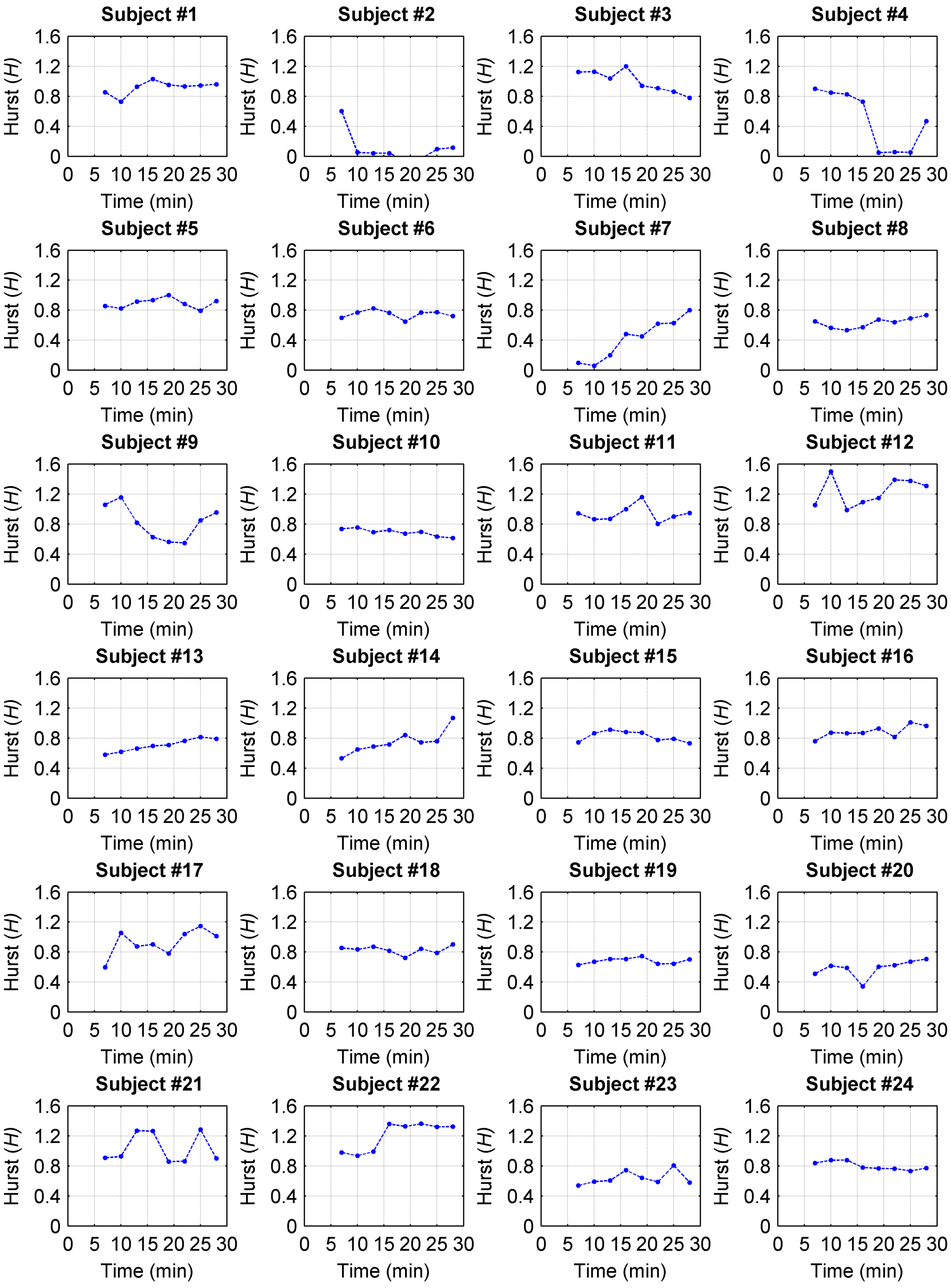

**Figure B.34:** Cardiac Index - SWE - Diffusion Entropy - Abnormal HRV I

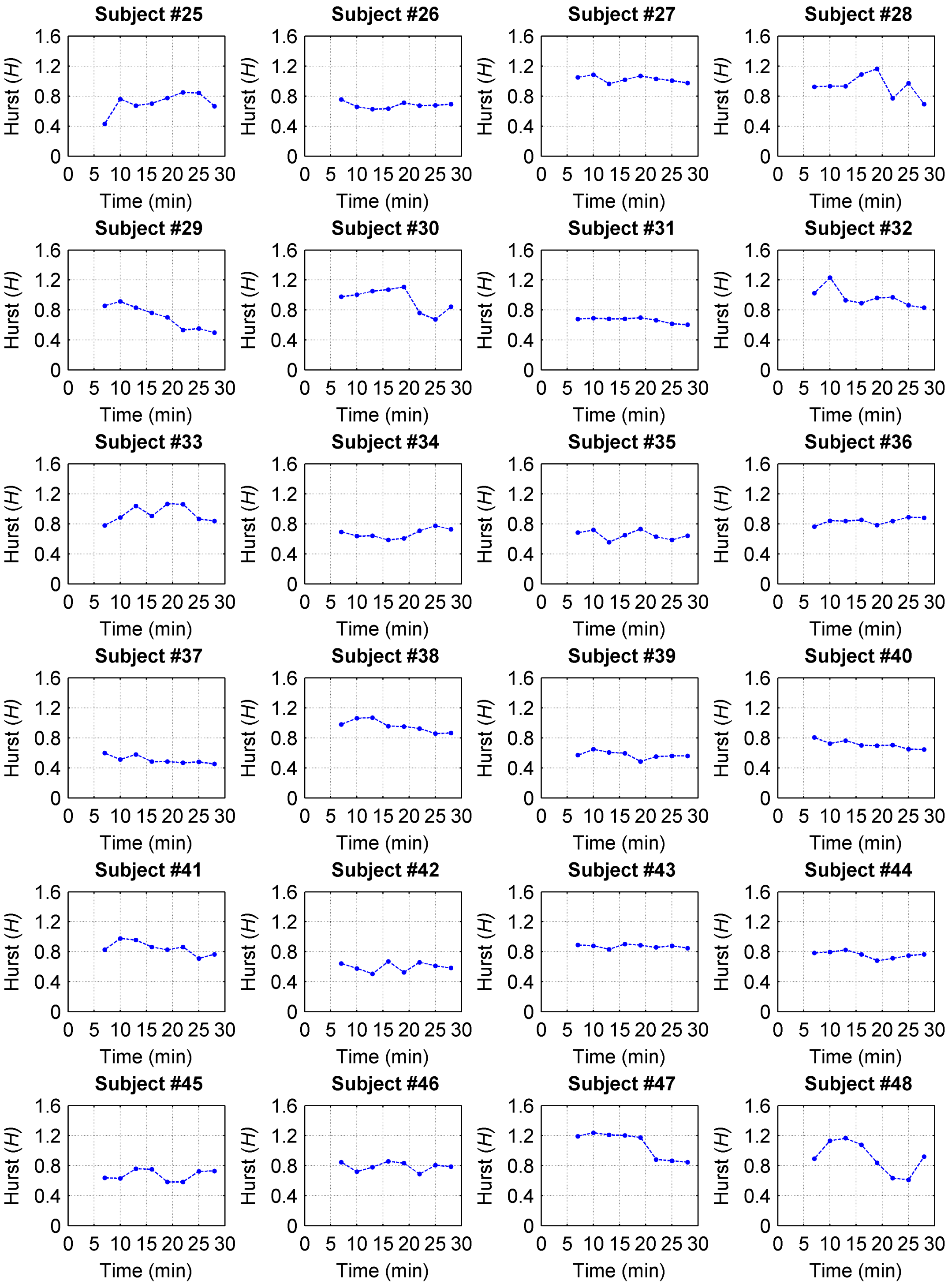

**Figure B.35:** Cardiac Index - SWE - Diffusion Entropy - Abnormal HRV II

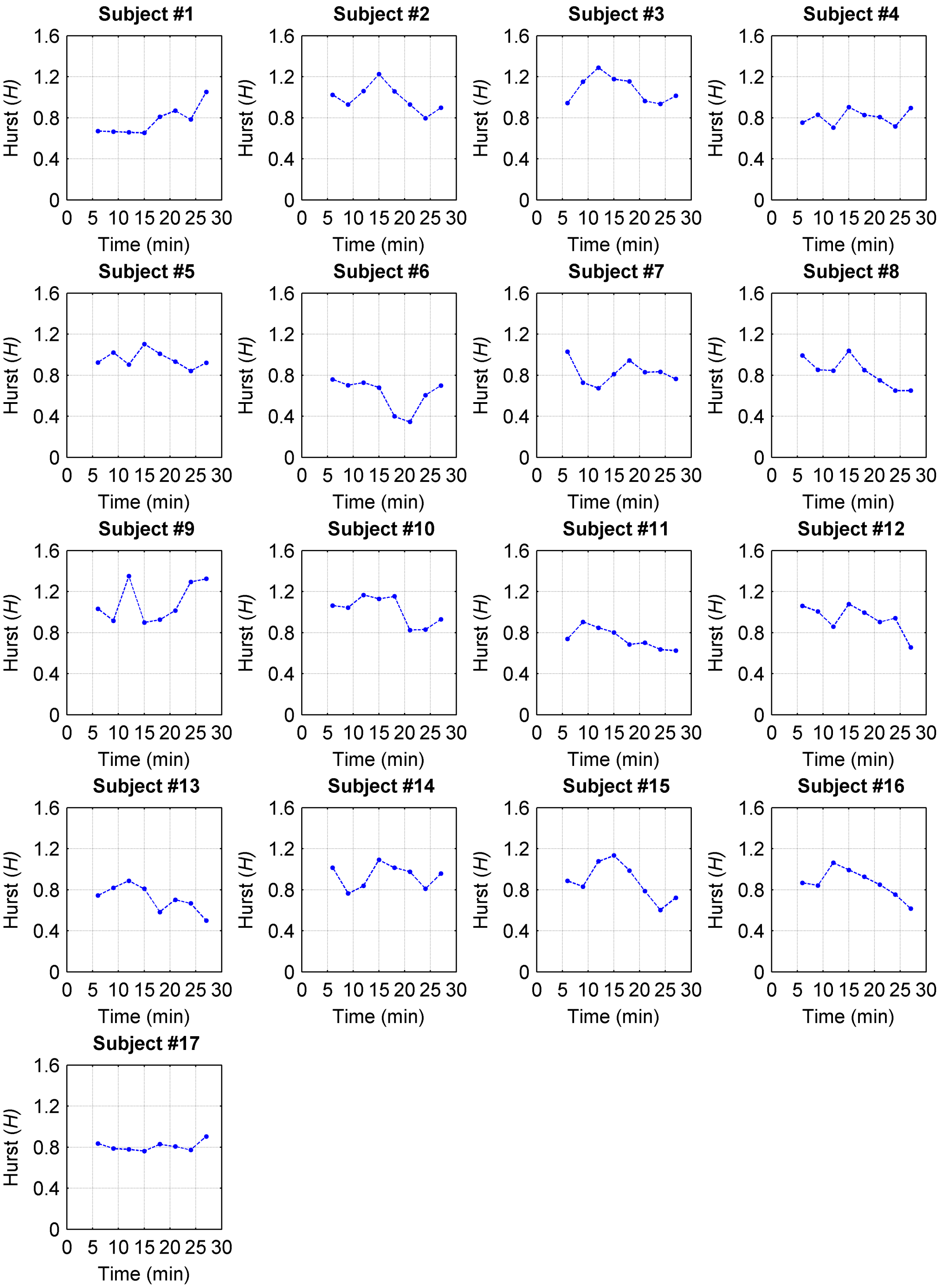

Subject #1 · Subject #2 · Subject #3 · Subject #4 · Subject #5 · Subject #6 · Subject #7 · Subject #8 · Subject #9 · Subject #10 · Subject #11 · Subject #12 · Subject #13 · Subject #14 · Subject #15 · Subject #16 · Subject #17

**Figure B.36:** Cardiac Index - SWE - Peng - Normal HRV

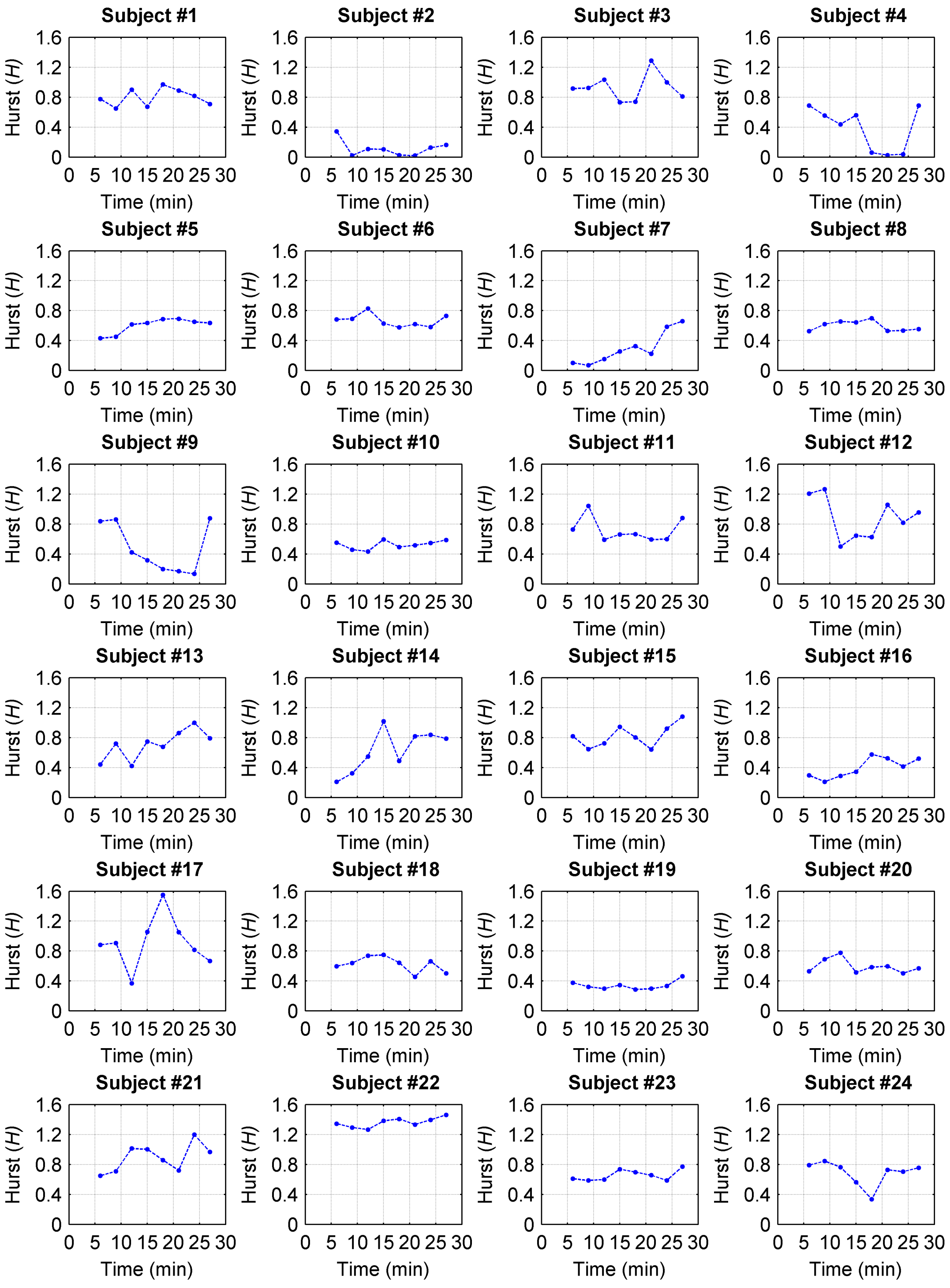

**Figure B.37:** Cardiac Index - SWE - Peng - Abnormal HRV I

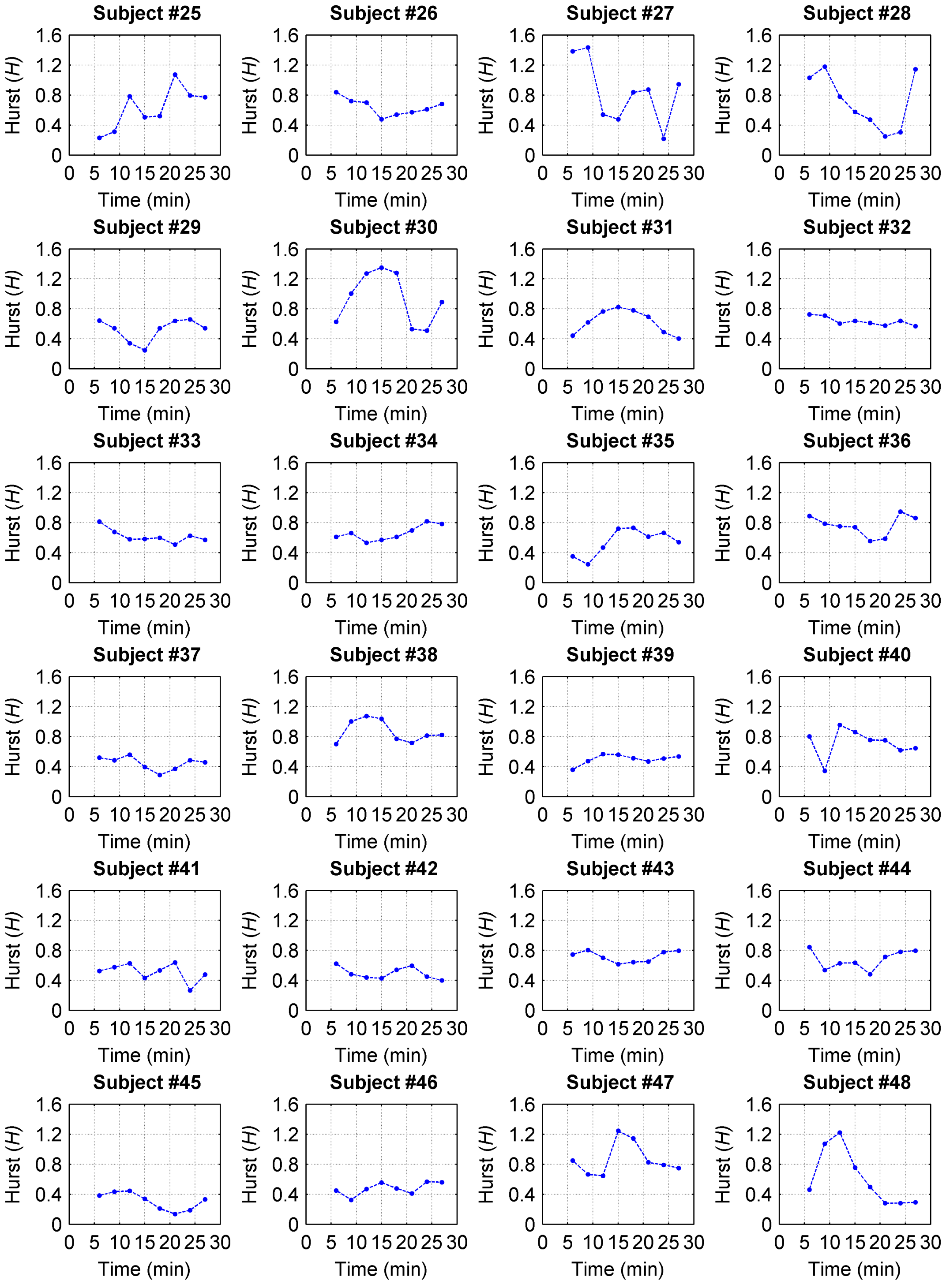

**Figure B.38:** Cardiac Index - SWE - Peng - Abnormal HRV II

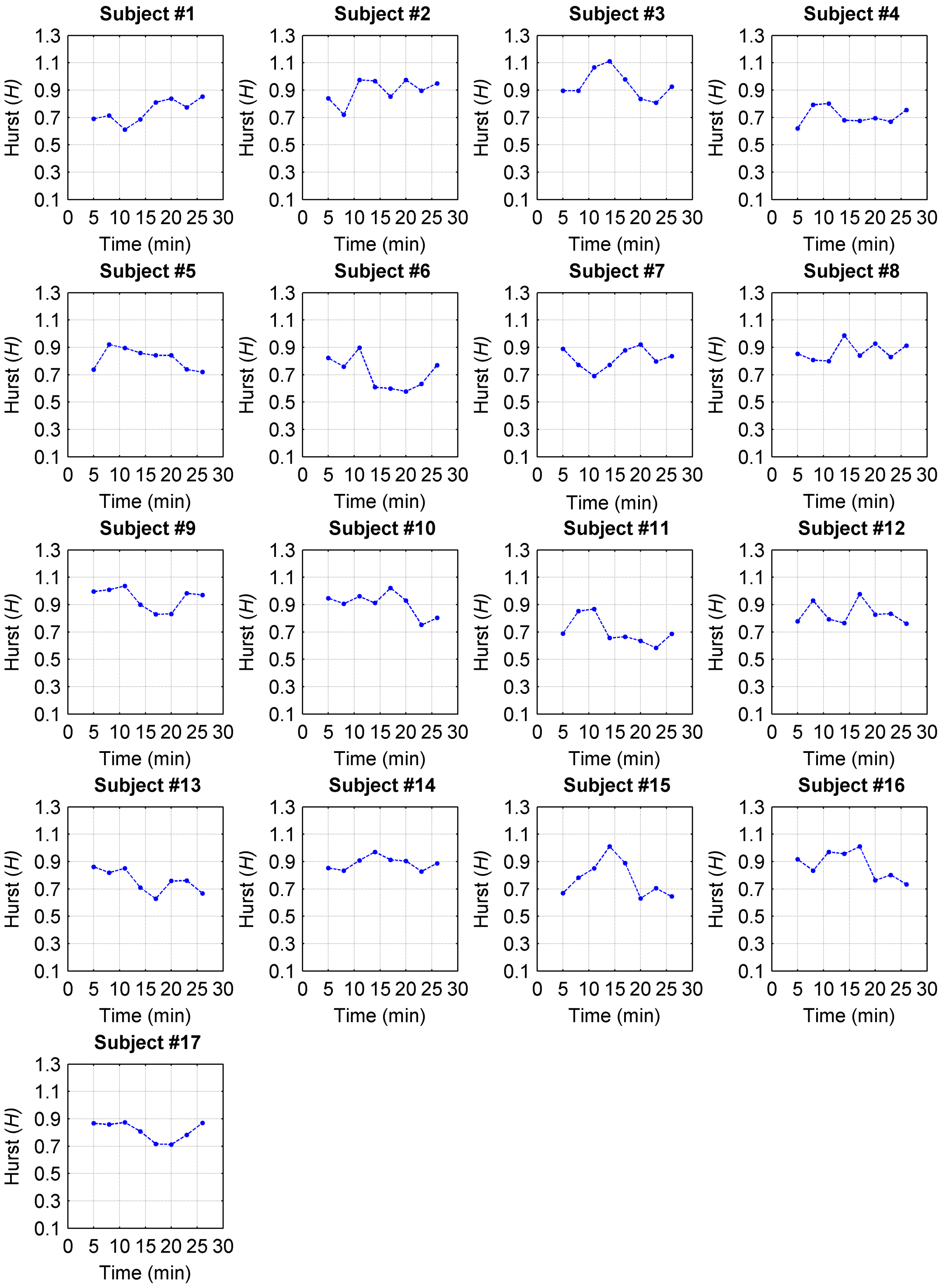

**Figure B.39:** Cardiac Index - SWE - Rescaled Range - Normal HRV

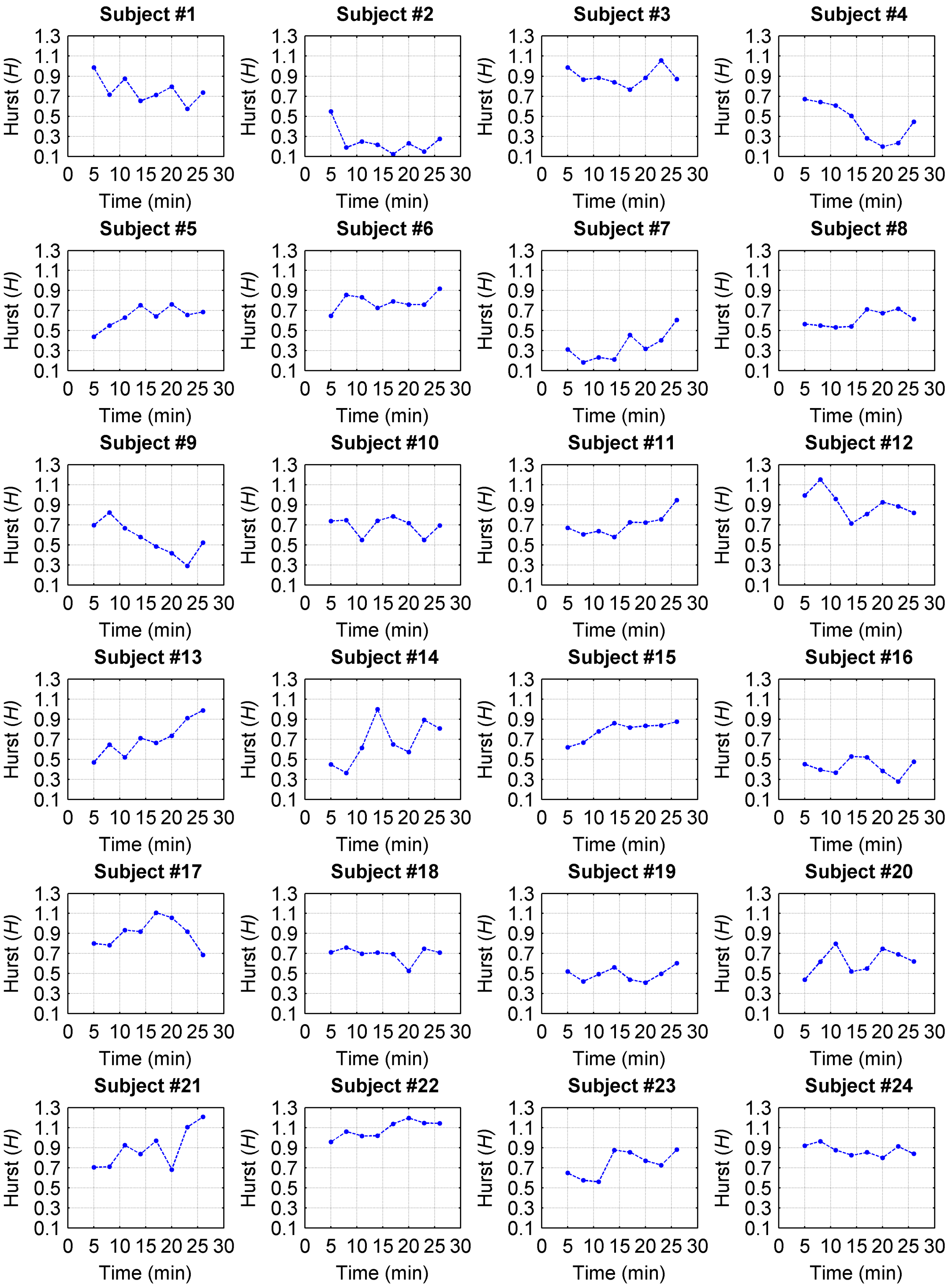

**Figure B.40:** Cardiac Index - SWE - Rescaled Range - Abnormal HRV I

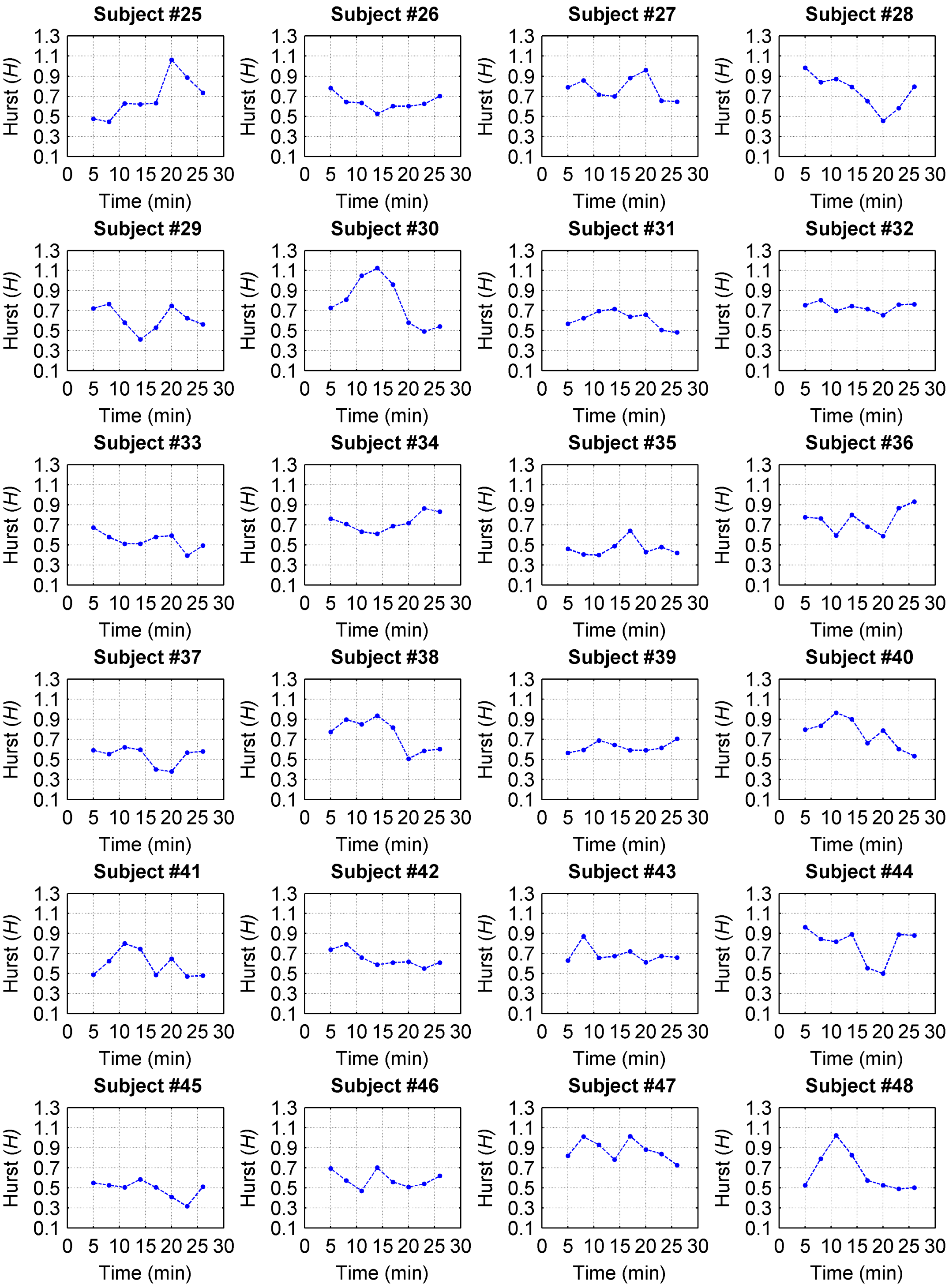

**Figure B.41:** Cardiac Index - SWE - Rescaled Range - Abnormal HRV II

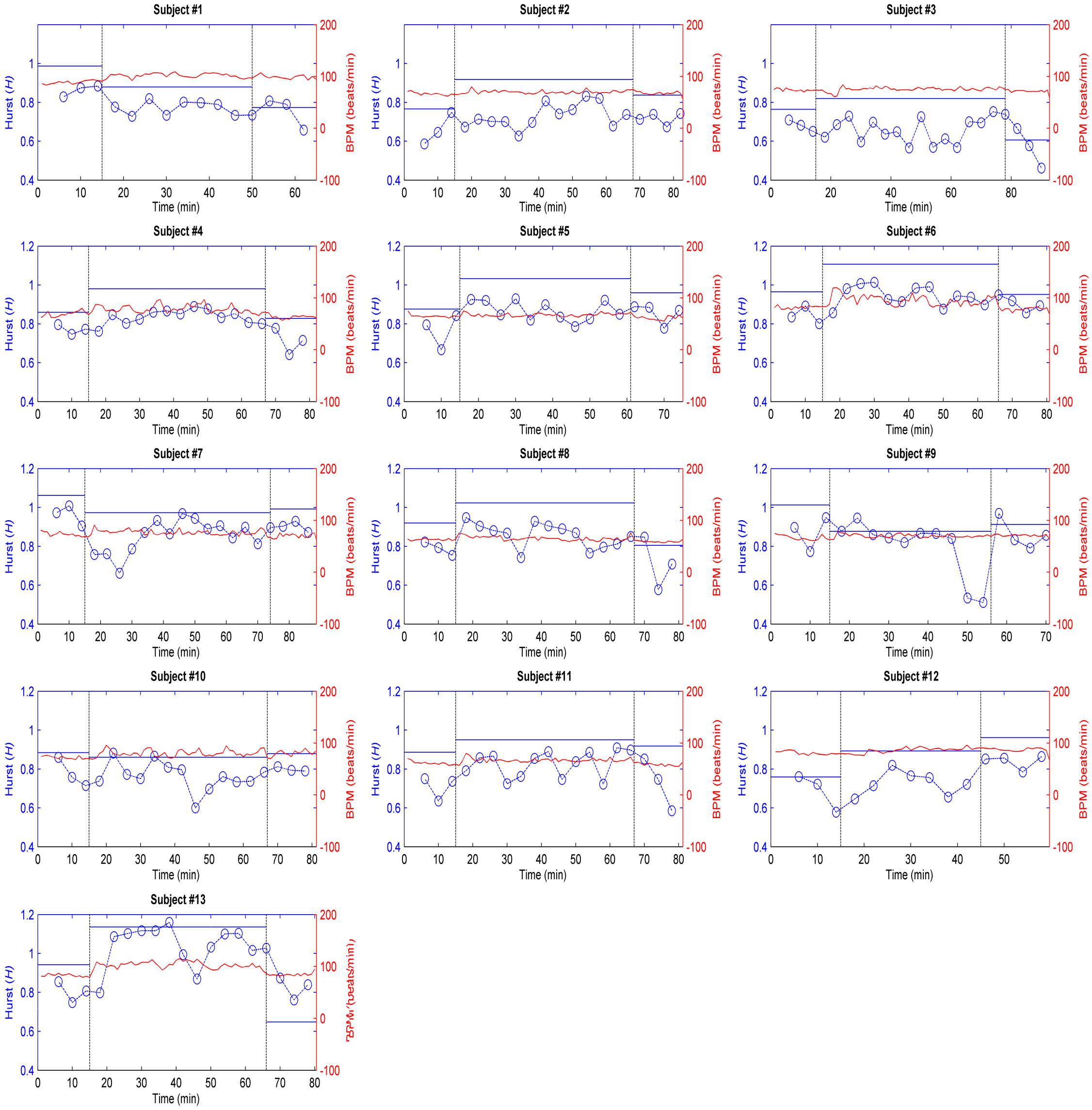

**Figure B.42:** Stress Detection - Diffusion Entropy - $(w_t = 6min, s_t = 4min)$

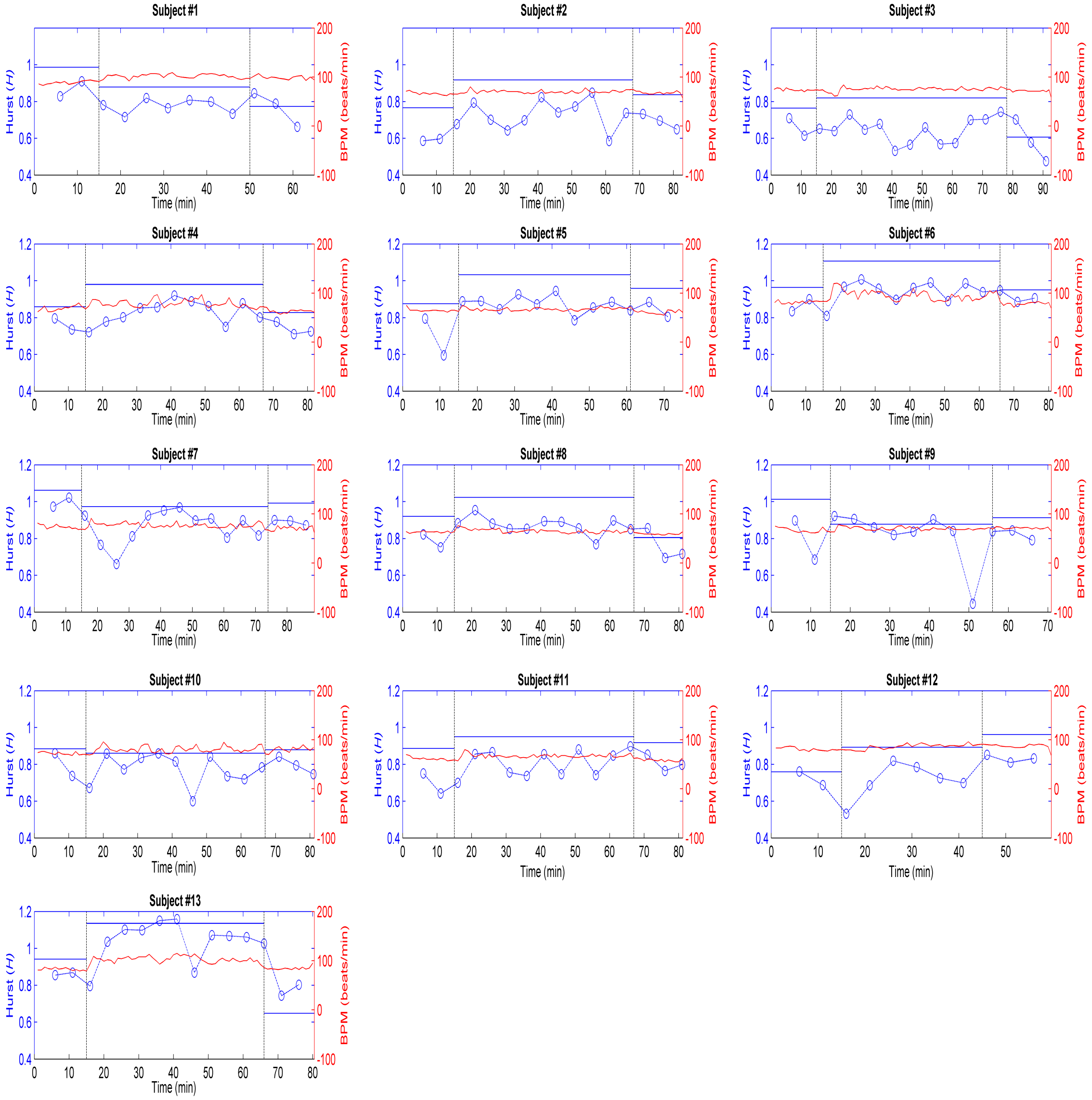

**Figure B.43:** Stress Detection - Diffusion Entropy - ($w_t = 6min, s_t = 5min$)

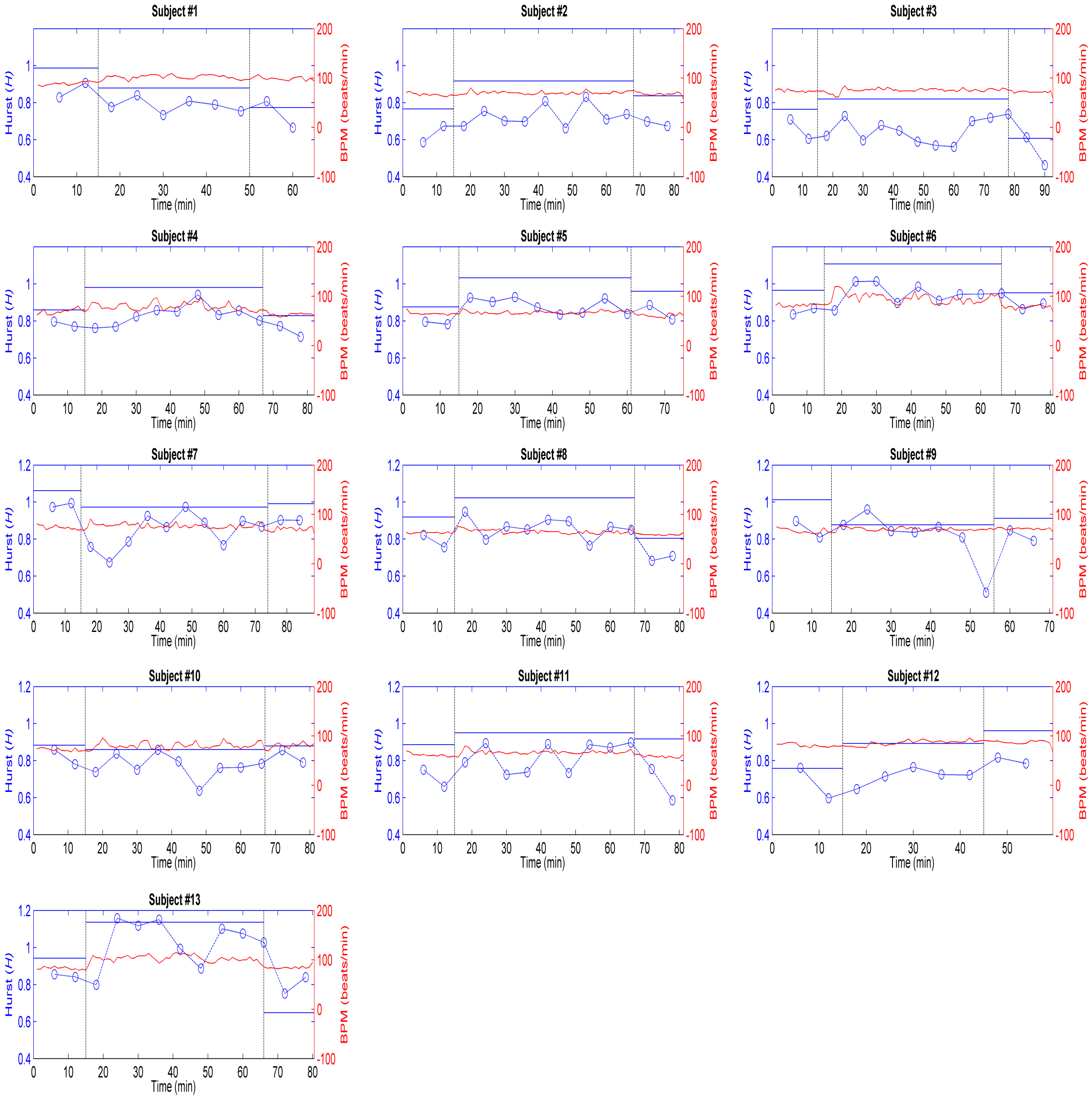

**Figure B.44:** Stress Detection - Diffusion Entropy - ($w_t = 6min, s_t = 6min$)

# Appendix C

# CODE

## C.1 Thermal Infrared - Pixel Data Acquistion

```
%% TIR PIXEL DATA ACQUISTION
%  Author: Marwin Ko & Monica Barbadillo
%  Version 1.0,  08/31/2015
%  mko3@ucmerced.edu
clc; clear;

%% SET UP VARIABLES
quote = '"';    sep = ',';  escape = '\n';
files = dir('*.csv'); TI = 1800;

%% LOAD SELECTED PIXEL MATRIX
load('pixels_20x20.mat')

%% OPEN TEXT FILE
for j = 1:825
    for k = 1:1:TI
        cName = files(k).name;
        [numbers, text] = swallow_csv(cName,quote,sep,escape);
        pixels(k,j) = numbers(pix_20x20(j,1), pix_20x20(j,2));
    end
end

%% SELECTED (20X20) PIXEL MATRIX
%{
clc; clear;
row = (0:20:480); %24+1
col = (0:20:640); %32+1
i = 1;
for r = 1:25
    for c = 1:33
        pix_20x20(i,1) = row(r);    pix_20x20(i,2) = col(c);
        i = i + 1;
    end
end
pix_20x20(pix_20x20==0)=1;  save('pixels_20x20','pix_20x20');
%}
```

## C.2 Thermal Infrared - Mapping

```matlab
%% CREATE TIR HURST/MEAN/VARIANCE/MAPS
%  Author: Marwin Ko & Monica Barbadillo
%  Version 1.0,  08/31/2015
%  mko3@ucmerced.edu
clc; clear; tic;

%% LOAD SELECTED PIXEL MATRIX
load('pixels_20x20.mat');   chosen_pix = pix_20x20;

%% TOTAL DATA HURST
for i = 1
    load(['PIXEL20X20_',num2str(i),'.mat']);    pix = pixels;
    h_map = zeros(825,1);   u_map = zeros(825,1);
    v_map = zeros(825,1);   temp_column = zeros(1800,1);

    for j = 1:825
        temp_column = pix(:,j);

        % create maps
        h = Dentropy(temp_column);  h_map(j,1) = h;
        u = mean(temp_column);      u_map(j,1) = u;
        v = var(temp_column);       v_map(j,1) = v;
    end

    % order: [ROW, COLUMN, HURST, MEAN, VARIANCE]
    pixels_map = [chosen_pix, h_map, u_map, v_map];

    % eliminate initial 200 data points
    pix_ss = pixels(201:1800,:);

    h_map_ss = zeros(825,1);    u_map_ss = zeros(825,1);
    v_map_ss = zeros(825,1);    temp_column_ss = zeros(1600,1);

    for k = 1:825
        temp_column_ss = pix_ss(:,k);

        % create maps
        h = Dentropy(temp_column_ss);   h_map_ss(k,1) = h;
        u = mean(temp_column_ss);       u_map_ss(k,1) = u;
        v = var(temp_column_ss);        v_map_ss(k,1) = v;
    end

    pixels_map_ss = [chosen_pix, h_map_ss, u_map_ss, v_map_ss];
    save(['PIXEL_MAPS_',num2str(i)],'pixels_map','pixels_map_ss');

end
```

## C.3 Cumulative Window Estimation

```
%% Cumulative Window Estimation (CWE) - function file
%  Author: Marwin Ko & Monica Barbadillo
%  Version 1.0,  08/31/2015
%  mko3@ucmerced.edu
function [H_normal, H_abnormal] = ...
    CWE(normalData,abnormalData,method)
opt = 1; isplot = 0;

%% MINUTE ARRAY
minute = 30;
for m = 1:minute
    mins(m,1) = m;
end

%% SELECTR START TIME
% Diffusion Entropy start @ 3min (aka skips first 2 mins)
% Peng & Rescaled Range start @ 2min (aka skips first 1 min)
de = strcmp('dentropy',method); rs = strcmp('RS',method);
pg = strcmp('peng',method);
if de == 1
    start = 3;
    else if rs == 1
        start = 2;
        else if pg == 1
            start = 2;
else
start = 1;
        end
    end
end

%% NORMAL
for m = start:1:minute
    for i = 1:1:17
    load([normalData,num2str(i)])
    [¬,RR_interval_seg] = ...
        RRtime_segment(RR_time,RR_interval,mins(m,1));
        if de == 1
            H_normal(m,i) = Dentropy(RR_interval_seg);
        else
            H_normal(m,i) = ...
                hurst_estimate(RR_interval_seg,method,isplot);
        end
    end
end

```

```
%% ABNORMAL
for m = start:1:minute
    for j = 1:1:48
    load([abnormalData, num2str(j)])
    [¬,RR_interval_seg] = RRtime_segment(RR_time,RR_interval, ...
        mins(m,1));
       if de == 1
            H_abnormal(m,j) = Dentropy(RR_interval_seg);
       else
            H_abnormal(m,j) = ...
               hurst_estimate(RR_interval_seg,method,isplot);
       end
    end
end
end
```

## C.4 Sliding window Optimization

```
%% Sliding Window Optimization
%  Author: Marwin Ko
%  Version 1.0,  08/31/2015
%  mko3@ucmerced.edu
clear; clc;
method = {'aggvar'; 'absval';'diffvar'; 'dentropy'; 'peng'; 'RS';};
tit = {'Aggregated Variance';'Absolute Value';...
'Difference Variance';'Diffusion Entropy';'Peng';'Rescaled Range'};

%% FIND OPTIMAL WINDOW & SLIDE LENGTH(S)
z = input('Enter Method#: ');   load(['A3_avgVar2_',method{z}]);
avg_var(avg_var==0) = NaN;      data = avg_var';    MIN = min(data);
for i = 2:1:10
    [s,w] = find(data==min(data(:,i))); slide(i)=s; window(i)=w;
end
MIN(isnan(MIN))= 0; optWindow = [window',slide',MIN'];

%% PLOT OPTIMAL TRAJECTORY
figure;
for z = 1:1:6
    load(['A3_optSlideTrace_',method{z}]);
    load(['A3_avgVar2_',method{z}]);    avg_var(isnan(avg_var))= 0;
    optWindow(optWindow==0)= NaN;       w = optWindow(:,1);
    s = optWindow(:,2);                 v = optWindow(:,3);
    subplot(3,2,z); plot = surf(avg_var);   hold on;     grid on;
    plot3(s,w,v,'-k'); plot3(s,w,v,'r.');   alpha(.4);   colorbar;
    zlabel('Average Variance');     ylabel('Window Length (min)');
    title(['\bf',tit{z}]); xlabel('Slide Length (min)'); hold off;
end
```

## C.5 Sliding Window Estimation

```
%% Sliding Window Estimation (SWE) - function file
%  Author: Marwin Ko & Monica Barbadillo
%  Version 1.0,  08/31/2015
%  mko3@ucmerced.edu
function hMatrix = SWE(data,window,slide,method)
opt = 1; isplot = 0; load(data);

%% PARTITION HRV DATA
[RR_t_seg,RR_int_seg] = RRtime_segment(RR_time,RR_interval, 30);
last = RR_t_seg(length(RR_t_seg));  mins = int64(last/60);
iterations = ceil((mins-window)/slide); start=0; endd=window;
points = zeros(mins,1); hMatrix = zeros(iterations,2);

% calculate all minutes (number of points per minute)
for m = 1:mins
    [¬,RR_interval_seg] = RRtime_segment(RR_time,RR_interval, m);
    [points(m,1),n] = size(RR_interval_seg);
end
[¬,RR_interval_seg] = RRtime_segment(RR_time,RR_interval, endd);
windowMatrix = RR_interval_seg(1:end, 1);

%% HURST ESTIMATION
de = strcmp('dentropy',method); i = 1;
    if de == 1
        hMatrix(i,2) = Dentropy(windowMatrix);
    else
        hMatrix(i,2) = hurst_estimate(windowMatrix,method,isplot);
    end
hMatrix(i,1) = endd; start = start+slide; endd = endd+slide;
for i = 2:iterations
    [¬,RR_interval_seg] = RRtime_segment(RR_time,RR_interval, endd);
    s = points(start,1); windowMatrix = RR_interval_seg(s:end, 1);
        if de == 1
            hMatrix(i,2) = Dentropy(windowMatrix);
        else
            hMatrix(i,2) = ...
                hurst_estimate(windowMatrix,method,isplot);
        end
    hMatrix(i,1) = endd;
        if (endd+slide)>mins
            break;
        else
            start = start+slide;    endd = endd+slide;
        end
    end
end
```